

NASA Contractor Report 3243

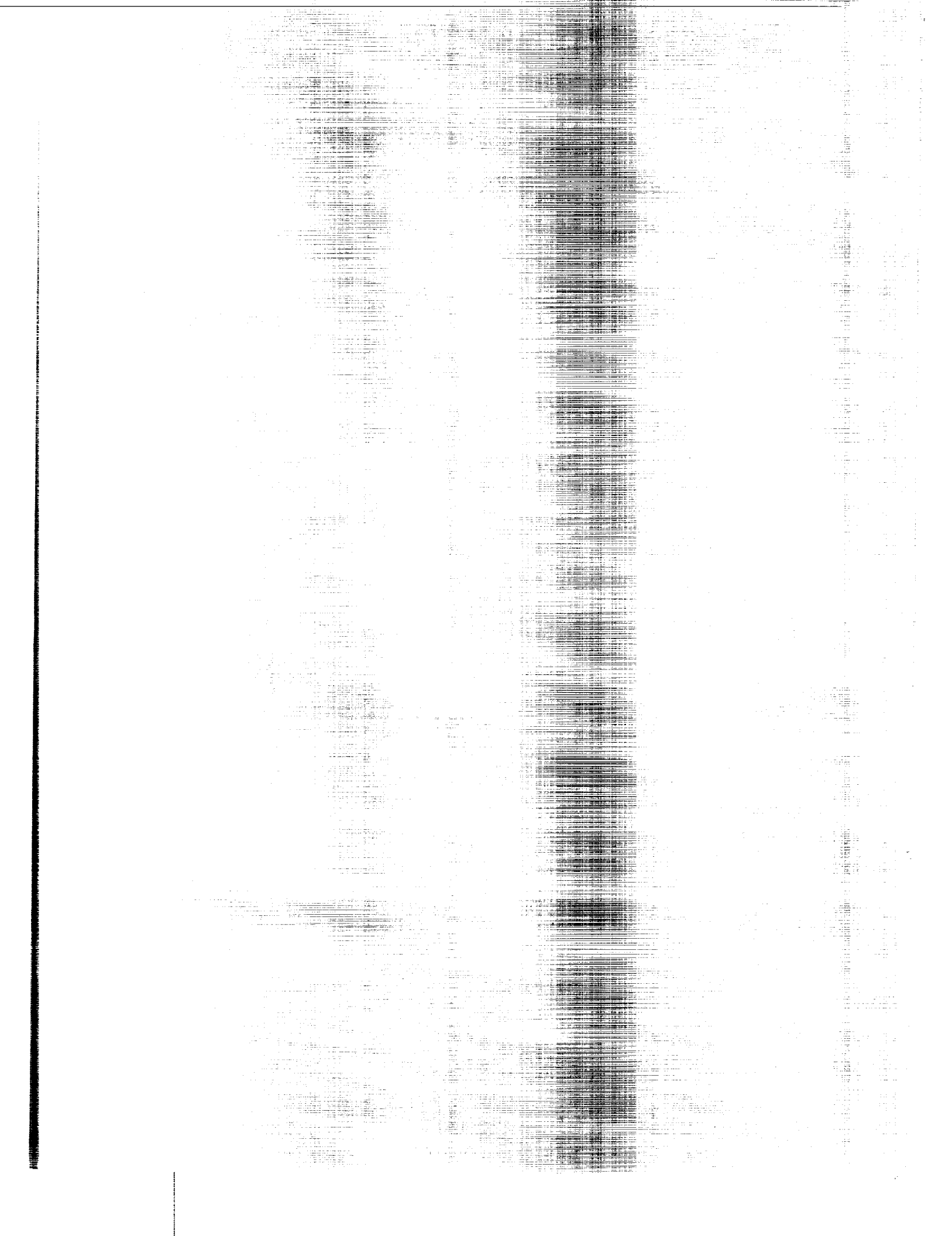
**Transonic Flow Field Analysis
for Wing-Fuselage Configurations**

Charles W. Boppe

**CONTRACT NAS1-14732
MAY 1980**

**CASE FILE
COPY**

NASA



NASA Contractor Report 3243

Transonic Flow Field Analysis for Wing-Fuselage Configurations

Charles W. Boppe
Grumman Aerospace Corporation
Bethpage, New York

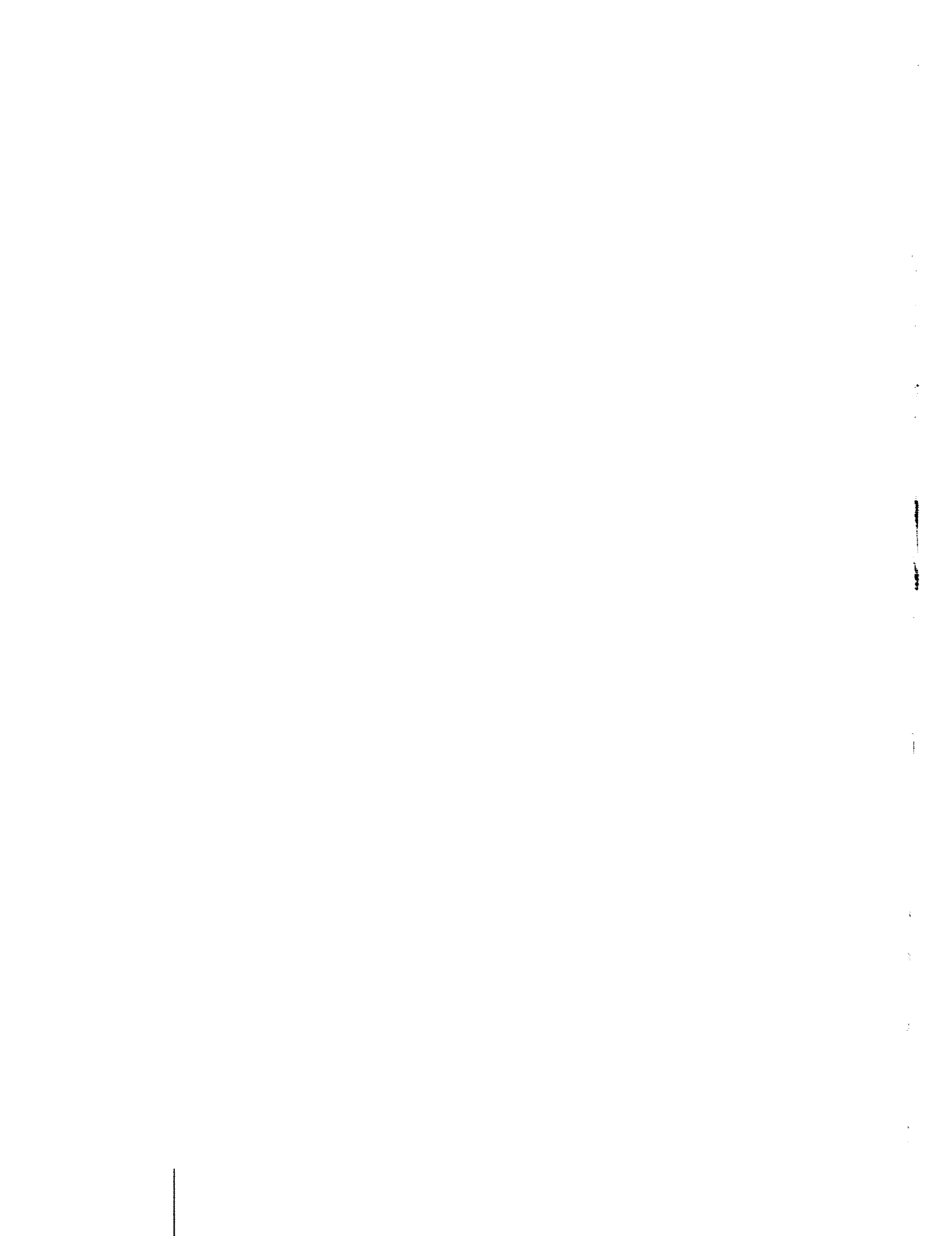
Prepared for
Langley Research Center
under Contract NAS1-14732

NASA

National Aeronautics
and Space Administration

**Scientific and Technical
Information Office**

1980



CONTENTS

	<u>Page</u>
SUMMARY	1
INTRODUCTION	3
NOMENCLATURE	5
COMPUTATIONAL METHOD	9
Flow Equation	9
Computational Space and Grid Systems	10
Finite Difference Approximations	19
Wing and Body Boundary Conditions	20
Solution Process	29
Body/Fuselage Geometry Model	34
Wing Viscous Effects	42
Pressure, Force and Moment Coefficients	49
COMPARISONS AND TYPICAL RESULTS	55
Isolated Bodies	55
Isolated Wings	60
Wing-Body Configurations	69
CONCLUDING REMARKS	91
APPENDIX: DESCRIPTION OF COMPUTER CODE WIBCO	97
REFERENCES	149

ILLUSTRATIONS

Figure		Page
1	Computational Space for Wing-Body Configuration	11
2	Grid Stretching ~ Physical X-Y Plane for Wing- Body Configuration	11
3	Wing Section/Crude Grid/Fine Grid Boundary Arrangement in Physical X-Z Plane	14
4	Details of Fine Embedded Wing Grid	15
5	Wing Fine Grid System Embedded in Crude Grid	17
6	Configuration with Crude Grid and Embedded Fine Grid Systems	17
7	Details of Fine Embedded Body Grid	18
8	Grid Approximation of Wing and Wake Surfaces	22
9	Wing Root Boundary Condition for Dummy Interior Points	24
10	Computational and True Body Surfaces	26
11	Details of Body Surface Approximation	27
12	Phase 2 Isolated Body Crude/Fine Grid Solution Process	30
13	Wing Section Crude/Fine Grid Interface	31
14	Three Different Grid Systems for Wing-Body Solution	33
15	Fixed Wing Surface Region for Embedded Body Grid Solution	33
16	Geometry Model Lines and Coordinate Systems	36
17	Components of Body and Cross-Section Line Models	38
18	Crude Grid Interrogation of Complete Geometry Model	39
19	Fine Grid Region Interrogation of Geometry Model	40
20	Geometry Model for Area-Ruled Fuselage	40
21	Wing Section Viscous Effects	43
22	Infinite Sheared Wing Coordinate System	44
23	Wing Viscous Effects Approximated by Infinite Sheared Wing Approach	45
24	Bavitz Empirical Relation Points	48
25	Wing Planform Parameters	50
26	Results Section Symbol Definition	56

ILLUSTRATIONS (contd)

<u>Figure</u>		<u>Page</u>
27	Sharp Nose Body Pressure Distribution Correlation	57
28	Sharp Nose Body Pressure Distribution Correlation	57
29	Blunt Nose Body Pressure Distribution Correlation	59
30	Grumman Gulfstream II Fuselage Pressure Distribution Correlation	59
31	Grumman Gulfstream II Fuselage - Decay of Canopy Shockwave, $M = 0.800$, $\alpha = 3.10^\circ$	61
32	Superimposed Computed Pressure Distributions for Isolated Onera M6 Wing.	62
33	Onera M6 Wing Pressure Distribution Correlation.	62
34	Onera M6 Wing Section Force and Moment Coefficient Correlation, $M=0.8407$, $\alpha = 3.01^\circ$	64
35	Onera M6 Wing Computed Spanload	65
36	NACA RM A9K01 Isolated Wing Superimposed Computed Pressure Distributions.	65
37	NACA RM A9K01 Wing Pressure Distribution Correlation	66
38	NACA RM A9K01 Isolated Wing Spanload Correlation	67
39	NACA RM A9K01 Isolated Wing Force and Moment Coefficient Correlation, $M = 0.85$, $\alpha = 4^\circ$	68
40	NACA RM L51F07 Simple Wing-Body Configuration	70
41	NACA RM L51F07 Wing-Body Superimposed Computed Wing Pressure Distributions	71
42	NACA RM L51F07 Wing Pressure Distribution Correlation	71
43	NACA RM L51F07 Stations for Computed and Experimental Body Pressures	73
44	NACA RM L51F07 Body Pressure Distribution Correlation	74
45	NACA RM L51F07 Wing-Body Spanload Correlation	75
46	Wing-Body Spanwise Pitching Moment Coefficient Correlation, NACA RM L51F07, $M = 0.93$, $\alpha = 4^\circ$	76
47	Wing-Body Force and Moment Coefficient Correlation NACA RM L51F07, $M = 0.93$, $\alpha = 4^\circ$	77

ILLUSTRATIONS (contd)

<u>Figure</u>		<u>Page</u>
48	NACA RM L51F07 Wing and Body Drag Coefficient Correlation	78
49	NACA RM L51F07 Body Longitudinal Load Correlation	79
50	Boeing KC-135 Transport Configuration (Pylons and Engines Off)	79
51	Boeing KC-135 Transport, Superimposed Computed Wing Pressure Distributions	80
52	Boeing KC-135 Transport Wing Pressure Distribution Correlation	81
53	Supercritical Wing/Area-Ruled Fuselage Transport Configuration	82
54	NASA TM X-3431 Transport Configuration Superimposed Computed Pressure Distributions for Basic Wing	83
55	NASA TM X-3431 Transport Configuration Wing Pressure Distribution Correlation for Basic Wing	84
56	NASA TM X-3431 Transport Configuration Superimposed Computed Wing Pressures for Wing with Control Surface Deflected	85
57	NASA TM X-3431 Transport Configuration Wing Pressure Distribution Correlation for Wing with Control Surface Deflection	86
58	Force and Moment Correlation for Supercritical Wing/Area-Ruled Fuselage Transport Configuration, $M = 0.90$, $\alpha = 3.91^\circ$	88
59	Force and Moment Correlation for Supercritical Wing/Area-Ruled Fuselage Transport Configuration with Wing Control Surface Deflection ($\delta F_2 = -15^\circ$) $M = 0.90$, $\alpha = 3.93^\circ$	89
60	NASA TM X-3431 Transport Configuration Effect of Wing Control Surface Deflection on Computed Wing Spanload	90
61	NASA-Douglas Supercritical Wing Transport Configuration.	92
62	Douglas Transport Configuration Superimposed Computed Pressure Distributions $M_\infty = 0.75$, $\alpha = 2.2^\circ$	93
63	Douglas Transport Configuration Wing Pressure Distribution Correlation, $M_\infty = 0.75$, $\alpha = 2.2^\circ$	94

ILLUSTRATIONS (contd)

<u>Figure</u>	<u>Page</u>
64	Douglas Transport Configuration Wing Pressure Distribution Correlation, $M_\infty = 0.84$, $\alpha = 1.85^\circ$ 95
65	Future Grid Component Build-Up Capability for Complex Aircraft Configurations 96
A-1	Sample Input Geometry Verification Plot with Error in Z- Coordinate of Canopy Definition 122
A-2	Sample Input Geometry Verification Plot with Error in Y- Coordinate of Canopy Definition 122
A-3	Sample Input Geometry Verification Plot for Fuselage 123
A-4	Sample Input Geometry Verification Plot for Wing Sections. 123
A-5	Sample Input Geometry Verification Plot, Plan View 124
A-6	Sample Input Geometry Verification Plot, Head-On View 124

TABLES

<u>Table</u>	<u>Page</u>
1	Cross-Section Arc Shapes 37
2	Body Line Segment Shapes 37
3	Gulfstream Fuselage Quick-Geometry Model 41

SUMMARY

A computational method for simulating the aerodynamics of wing-fuselage configurations at transonic speeds has been developed. The finite difference scheme is characterized by a multiple embedded mesh system coupled with a modified or extended small-disturbance flow equation. This approach permits a high degree of computational resolution in addition to coordinate system flexibility for treating complex realistic aircraft shapes. To augment the analysis method and permit applications to a wide range of practical engineering design problems, an arbitrary fuselage geometry modeling system has been incorporated as well as methodology for computing wing viscous effects. Configuration drag is broken down into its friction, wave, and lift-induced components. Typical computed results for isolated bodies, isolated wings, and wing-body combinations are presented. The results are correlated with experimental data. A computer code which employs this methodology is described in the Appendix of this report.



INTRODUCTION

The inherent complexity of transonic flows renders a purely experimental approach to solving aircraft design problems impractical in many cases. Mixed subsonic and supersonic regions, shock waves, and complicated viscous effects characterize this flow field. Numerical methods for simulating transonic flows are being developed to reduce the design cost and improve the performance of high speed aircraft.

Murman and Cole ⁽¹⁾ developed the first practical technique for computing two-dimensional inviscid transonic flows. This scheme utilized mixed (upwind and central) finite differences which were applied to the small perturbation equation in Cartesian coordinates. The equation was solved iteratively by numerical relaxation. The success of this technique made it possible for other investigators ⁽²⁻⁴⁾ to develop methodology incorporating the full potential equation and exact boundary conditions. Typically, coordinate system transformations now provide a grid system which is closely aligned with the airfoil surface. The mapped coordinates simplify application of the exact boundary conditions which are consistent with the full potential equation method. One advantage of this approach is that details of the high-gradient region near the airfoil leading edge are accurately predicted.

It is interesting to note that three-dimensional numerical methods for computing transonic flows about wings and wing-body combinations have evolved in the same manner that airfoil methods evolved. The early work of Bailey and Steger ⁽⁵⁾ with the transonic small disturbance equation provided the foundation for a number of three-dimensional schemes now in existence ⁽⁶⁻¹²⁾. Full potential equation codes have also been developed for treating wings and simple wing-body shapes ⁽¹³⁻¹⁵⁾. Unfortunately, the geometry-fitting coordinate system which is very advantageous when applied to simple airfoil shapes becomes increasingly difficult to implement as geometries become more complex. Constraints on computational resolution and geometry/coordinate system flexibility arise in three-dimensional applications.

A high degree of numerical resolution will be necessary if flow details about complex shapes are required. Providing this resolution for both a wing and fuselage

simultaneously presents a difficult problem. In addition, computational mesh flexibility is necessary to permit the treatment of truly arbitrary shapes. This must all be accomplished with sufficient computing efficiency to insure a cost-effective approach to solving engineering design problems. These requirements place a severe strain on the conventional single continuous grid/coordinate transformation approach which characterizes existing numerical methods.

This grid embedding approach ⁽¹⁶⁾ provides a means for modeling and analyzing configuration components (wings and bodies) within local detailed fine grid regions. Beyond these fine grid regions, a global crude mesh treats the flow field. Fine mesh computations are performed only in a region very close to the configuration where gradients are large and details are important. This permits a high degree of computational resolution and, at the same time, reduces computer resource requirements. Perhaps more important, mesh flexibility for treating complex shapes is available since global transformations are not required.

The present effort provides methodology for treating the more complex realistic aircraft shapes that occur in practical applications. The method uses a modified or extended small disturbance flow equation. With full potential equation solutions in hand, this would at first appear to be a step in the wrong direction. However, the simplicity of the planar boundary conditions which accompany the small disturbance equation, permits the extensive use of Cartesian coordinates; this, in turn, facilitates the implementation of a grid embedding scheme.

NOMENCLATURE

SYMBOLS

C	Infinite sheared wing chord
C_{AV}	Average wing chord
C_D	Total configuration drag coefficient
C_{DF}	Configuration friction drag coefficient
C_{DI}	Configuration lift-induced drag coefficient
C_{DBODY}	Body drag coefficient
$C_{DP} (b)$	Body pressure drag (lift-induced and wave drag)
$C_{DP} (w)$	Wing pressure drag (lift-induced and wave drag)
C_{DWING}	Wing drag coefficient
$C_{D WAVE}$	Configuration wave drag coefficient
$C_{F BODY}$	Body skin-friction drag coefficient
$C_{F WING}$	Wing friction drag coefficient
C_L	Total configuration lift coefficient
$C_{L BODY}$	Body lift coefficient
$C_{L WING}$	Wing lift coefficient
C_M	Total configuration moment coefficient
$C_{M BODY}$	Body moment coefficient
$C_{M WING}$	Wing moment coefficient
C_R	Wing root chord at configuration centerline (ϕ)
C_T	Wing tip chord
C_{d_b}	Body cross-section pressure drag coefficient (lift-induced + wave drag)

NOMENCLATURE (Continued)

SYMBOLS

C_{d_w}	Wing section pressure drag coefficient (lift-induced + wave drag)
C_{f_w}	Wing section skin-friction drag coefficient
C_{l_b}	Body cross-section lift coefficient
C_{l_w}	Wing section lift coefficient
C_{m_b}	Body cross-section moment coefficient
C_{m_w}	Wing section moment coefficient (taken about reference position)
$C_{m_{w(loc)}}$	Wing section moment coefficient (taken about local quarter-chord position)
C_p	Pressure coefficient
C_{p^*}	Critical (sonic) pressure coefficient
C_1, C_2, C_3, B_1, B_2	Crude grid scaling constants
F	Body geometry function
L	Body length
M.A.C.	Mean aerodynamic chord
M_∞	Freestream Mach number
N_x, N_y, N_z	Surface normal direction cosines
R	Body surface distance
Re	Reynolds number
S	Arc length
S_{BASE}	Body maximum cross-sectional area
S_{PB}	Body projected area (x-y plane)
S_{BWET}	Body wetted area
S_{cs}	Cross-sectional area

NOMENCLATURE (Continued)

SYMBOLS

S_{EXP}	Exposed wing area (for wing-body combinations)
S_W	Wing area
$X_{C/4}$	Wing section quarter-chord position
X_{REF}	Position about which moments are computed
b	Wing span
E	Oswald efficiency factor (lift induced drag)
f	Wing geometry function
u, v, w	Perturbation velocities
x, y, z	Physical coordinates
$\Delta x, \Delta y, \Delta z$	Mesh spacing
∞	Infinity
Γ	Circulation
$\Lambda_{c/2}$	Wing mid-chord sweep angle
α	Angle-of-attack
γ	Specific heat ratio
δ^*	Wing boundary layer displacement thickness
η	Wing span position ($\eta = 2y/b$)
θ	Momentum thickness
λ	Wing taper ratio C_T/C_R
ξ, η, ζ	Computational coordinates (symbolic for all grid systems)
ρ	Density
τ	Shear stress
φ	Perturbation velocity potential

NOMENCLATURE (Concluded)

SYMBOLS

ω Subsonic relaxation factor

f Body fineness ratio

SUBSCRIPTS

GLE	Grid leading edge	} Local wing section fine grid
GTE	Grid trailing edge	

TE Wing section trailing edge

W Wing

b Body surface

c Computational surface

e Edge condition

l Lower surface

loc Local

u Upper surface

$\begin{pmatrix} i, j, k \\ l, m, n \end{pmatrix}$ Mesh indices

$\begin{pmatrix} \xi, \eta, \zeta \\ x, y, z \end{pmatrix}$ Partial derivatives

SUPERSCRIPTS

D Dummy value

\sim Infinite sheared wing coordinate

+

Wing/Wake upper surface

-

Wing/Wake lower surface

COMPUTATIONAL METHOD

Flow Equation

Early three-dimensional computations using the classical transonic small-disturbance equation indicated that shock waves with appreciable sweep ($>15^\circ$) relative to the freestream direction could not be resolved. As a result, Lomax, Bailey and Ballhaus⁽¹⁷⁾ proposed the retention of additional terms in the flow governing equation. Their derivation was based on simple sweep theory concepts.

The present method employs a flow equation constructed by adding three additional terms to the classical transonic small-disturbance equation. The flow equation is:

$$\begin{aligned}
 & [1 - M_\infty^2 - (\gamma + 1) M_\infty^2 \varphi_x - \frac{\gamma + 1}{2} M_\infty^2 \varphi_x^2] \varphi_{xx} - 2M_\infty^2 \varphi_y \varphi_{xy} \\
 & + [1 - (\gamma - 1) M_\infty^2 \varphi_x] \varphi_{yy} + \varphi_{zz} = 0
 \end{aligned} \tag{1}$$

All of these terms can be found in the full potential equation (see ref 18, page 204). The $\varphi_y \varphi_{xy}$ and $\varphi_x \varphi_{yy}$ terms, typically referred to as crossflow terms, permit the resolution of shock waves with large sweep angles. A graphic example of the effects of these terms on computed pressure distributions and shock wave pattern can be seen in Figure 9 of ref 16. The $\varphi_x^2 \varphi_{xx}$ term has been retained to provide a better approximation of the critical velocity at which the full potential equation changes type (elliptic to hyperbolic). Difference approximations are applied to equation (1) as it is written. Empirical corrections⁽¹⁹⁾ and similarity variables are not employed. The method could be classified as modified or extended small disturbance in character.

Pressure coefficients on wing surfaces are computed using the following equation.

$$C_p = -[2\varphi_x + (1 - M_\infty^2) \varphi_x^2 + \varphi_y^2] \tag{2}$$

To simplify velocity computations on the non-planar body surface, a simplified equation is used. Note that the φ_y and φ_z components as listed in ref 18, page 206 are not included in the present version of the method.

$$C_p = -[2\varphi_x + (1 - M_\infty^2) \varphi_x^2] \tag{3}$$

Computational Space and Grid Systems

The computational space used in the present method is illustrated in Figure 1. This space is filled with a relatively crude Cartesian mesh. Instead of adopting a far-field solution for the grid outer boundaries, the original x, y, z region is stretched to a ξ, η, ζ region in which the boundaries correspond to infinity. The flow field potential is set to zero on all bounding planes except the downstream plane for which the following equation is solved.

$$\varphi_{yy} + \varphi_{zz} = 0 \quad (4)$$

The following conditions are enforced at the symmetry plane.

$$\varphi_y = 0 \quad (5a)$$

$$\varphi_{xy} = 0 \quad (5b)$$

Carlson (20) has noted that caution must be exercised in selecting a grid stretching function. For this reason, simple tangent functions are employed. Space in the x -direction is broken up into three regions (see Figure 2). The grid stretching takes the following form:

$$\text{Regions I and III} \quad X = X_1 + B_1 \text{TAN} \left(\frac{\pi}{2} (\xi - \xi_1) \right) + B_2 \text{TAN} \left(\frac{\pi}{2} (\xi - \xi_1)^3 \right) \quad (6a)$$

$$\text{Region II} \quad X = C_1 \xi \quad (6b)$$

Note that an evenly spaced grid spans the wing planform for wing and wing-body cases*. For isolated bodies, the entire body is covered by Region II. The computational space is divided into 50 cells or segments in the x -direction. Of these, 38 cells are constrained to fall within Region II. The constants C_1 and B_1 are computed by requiring that

$$X = X_1 \text{ at } \xi = \xi_1 \quad (6c)$$

* The author would like to thank Ed Waggoner (Vought Corporation) for demonstrating the improved performance of this x -grid system over that originally employed (see ref 16).

NOTE: ALL PLANES EXCEPT SYMMETRY
PLANE REPRESENT INFINITY.

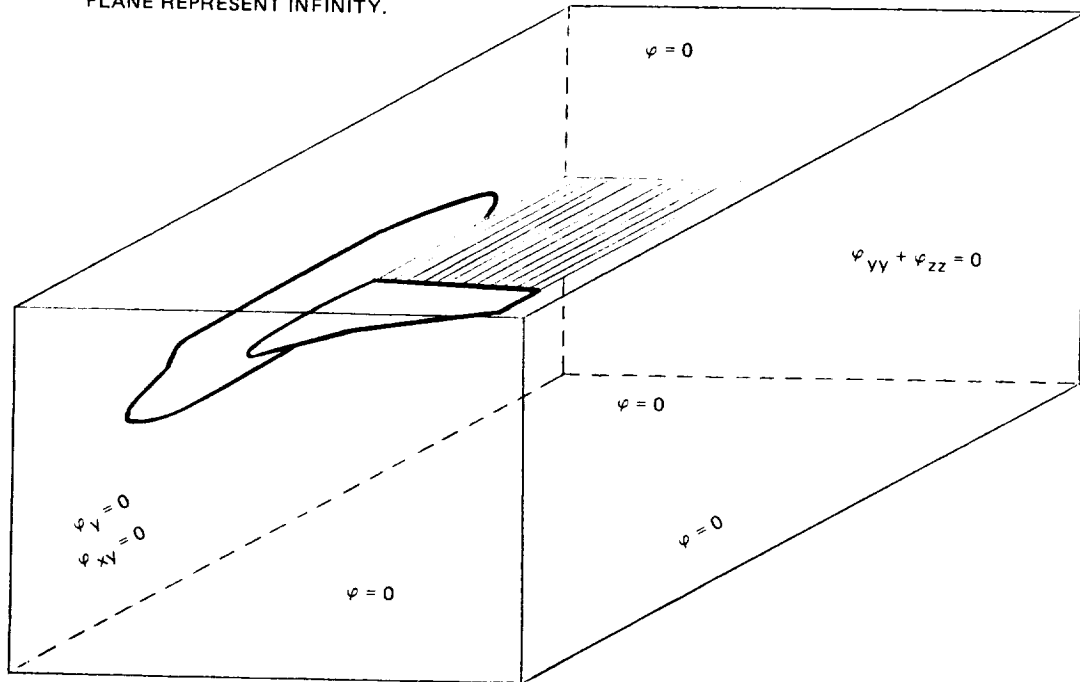


Figure 1 Computational Space for Wing-Body Configuration

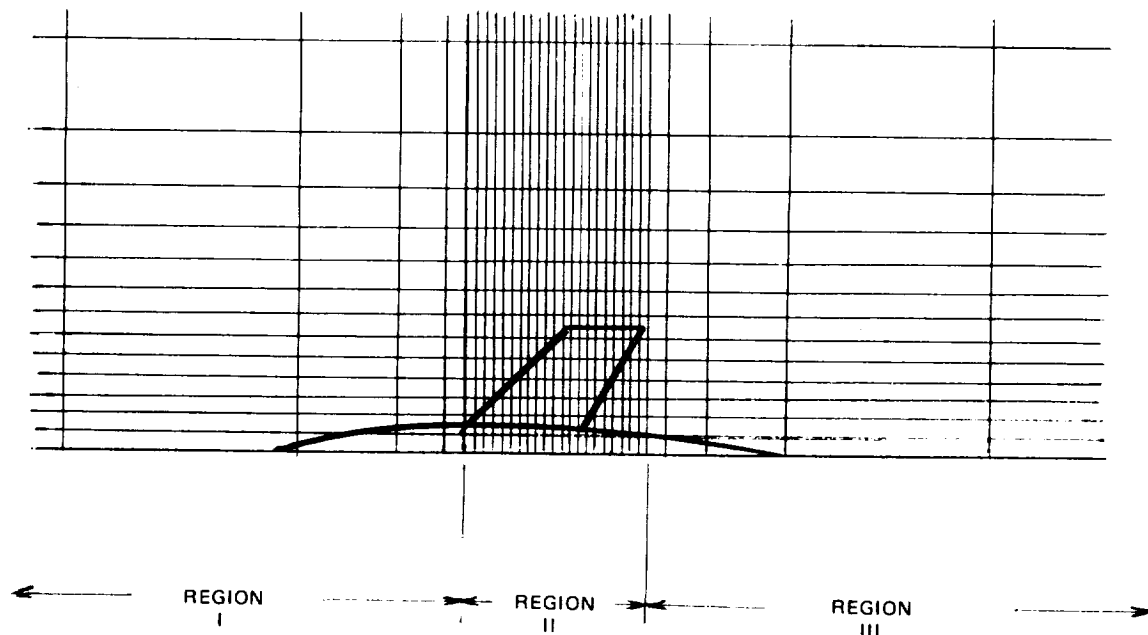


Figure 2 Grid Stretching ~ Physical X-Y Plane for Wing-Body Configuration

and

$$\left(\frac{dx}{d\xi}\right)_I = \left(\frac{dx}{d\xi}\right)_{II} \text{ at } X = X_1 \quad (6d)$$

The constant B_2 is determined by requiring that the next-to-last physical x-grid point be stretched several configuration lengths upstream and downstream. As a result, the finite computational region:

$$-4.167 \leq \xi \leq 4.167 \quad (6e)$$

corresponds to the infinite physical region:

$$-\infty \leq X \leq \infty \quad (6f)$$

Grid stretching in the y-direction takes the following form:

$$Y = \frac{\text{TANH}^{-1}(\eta)}{C_2} \quad (7a)$$

The hyperbolic tangent saves considerable computing resources when compared to the milder tangent function. The use of this exponential function in the spanwise direction has resulted in no apparent problems. The constant C_2 is adjusted to provide 18 crude grid span lines along the wing out of the total of 26. In addition, it is required that the wing tip lie exactly at the midpoint between two y-grid lines. This central tip location provides the best approximation of the wing tip aerodynamics. The finite computational region:

$$0 \leq \eta \leq 1 \quad (7b)$$

now corresponds to the infinite physical region:

$$0 \leq y \leq \infty \quad (7c)$$

The grid stretching function in the z-direction is:

$$Z = C_3 \text{TAN}\left(\frac{\pi}{2}\zeta\right) \quad (8a)$$

Thirty-one grid lines are employed with the constant C_3 chosen to provide sufficient mesh stretching so as not to inhibit or suppress supersonic flow development. As a result, the finite computational region:

$$-1 \leq \zeta \leq 1 \quad (8b)$$

now corresponds to the infinite physical region:

$$-\infty \leq Z \leq \infty \quad (8c)$$

The stretching adds transform derivatives to the crude grid governing equation. The following substitutions are made in equation (1).

$$\varphi_x = \varphi_\xi \xi_x \quad (9a)$$

$$\varphi_{xx} = \varphi_{\xi\xi} (\xi_x)^2 + \varphi_\xi \xi_{xx} \quad (9b)$$

$$\varphi_y = \varphi_\eta \eta_y \quad (9c)$$

$$\varphi_{yy} = \varphi_{\eta\eta} (\eta_y)^2 + \varphi_\eta \eta_{yy} \quad (9d)$$

$$\varphi_{xy} = \varphi_{\xi\eta} \xi_x \eta_y \quad (9e)$$

$$\varphi_{zz} = \varphi_{\zeta\zeta} (\zeta_z)^2 + \varphi_\zeta \zeta_{zz} \quad (9f)$$

This results in a total of 41,106 grid points representing the global crude grid. The primary purpose of this mesh system is the proper representation of both configuration effects in the far-field and far-field conditions on the configuration. However, the crude mesh also serves as a communication link for the embedded fine grid arrays to be described.

Individual fine grid arrays are constructed for the wing and body. These secondary mesh systems serve two purposes. First, detailed computations are performed only in a region very close to the wing or body where gradients are large and details are important. The resulting numerical efficiency permits a very dense computational mesh, a benefit in both the resolution of shock waves and the calculation of configuration forces and moments. Second, the embedded mesh systems are independent and optimized for a particular geometric component (wing or body shape). The system is not constrained by a single geometry-fitting transformation. This will facilitate future applications to configurations with multiple wing (wing, winglets, pylons, canards) surfaces and multiple body (fuselage, pods, engines) surfaces.

Wing fine grid arrays are set up at each position where a crude y-grid line cuts the wing surface. This results in 18 fine arrays for isolated wings and somewhat less (depending on fuselage span extent) for wing-body combinations. Figure 3 is a schematic which illustrates the wing section/grid system arrangement at a particular span station along the wing.

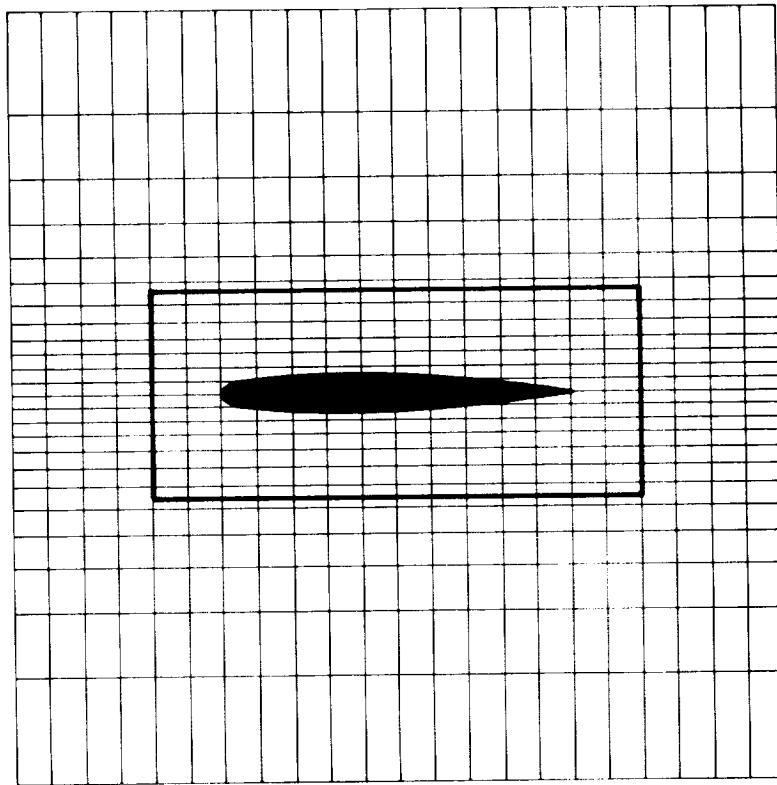


Figure 3. Wing Section/Crude Grid/Fine Grid Boundary Arrangement in Physical X-Z Plane

The wing fine grid is evenly spaced in both the x and z-directions (see Figure 4). As a result, a shock wave will be resolved to an equivalent degree independent of its position along the wing chord. The wing section leading and trailing edge are positioned at the mid-point between two streamwise mesh points. The present formulation utilizes 100 mesh points along the wing chord. Fine grid boundaries are positioned at 20% local chord distance in front of each wing section leading edge and 10% behind each trailing edge. Similarly, boundaries are set at 30% of the wing average chord distance above each section and 10% below. These limits have been pre-set in the solution coding and were used for all computed results presented herein. They may, of course, be modified for special applications. The total number of field points in the wing grid system is approximately 60,750.

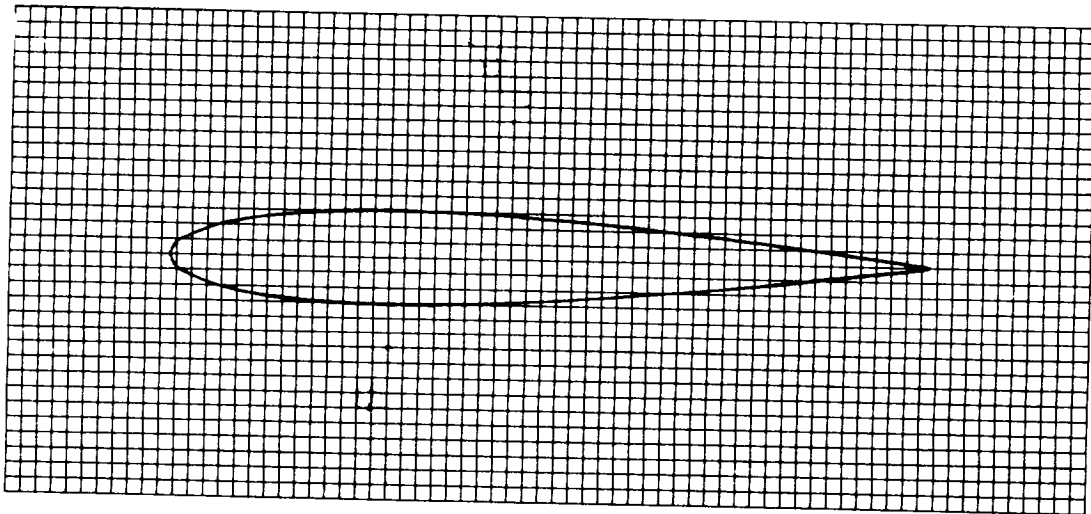


Figure 4 Details of Fine Embedded Wing Grid

The wing fine grid system has been sketched in Figure 5. Note that the embedded grid system is tapered as is the wing planform. A shearing transformation is introduced so that neighboring fine grid arrays can be used directly for cross-flow differencing.

$$x = \xi (X_{GTE} - X_{GLE}) + X_{GLE} \quad (10a)$$

$$y = \frac{\text{TANH}^{-1}(\eta)}{C_2} \quad (10b)$$

$$z = \zeta \quad (10c)$$

As was the case for the crude grid stretching transformation, this shearing transformation introduces additional terms into the flow equation. The following substitutions are made in equation (1).

$$\varphi_x = \varphi_\xi \xi_x \quad (11a)$$

$$\varphi_{xx} = \varphi_{\xi\xi} (\xi_x)^2 \quad (11b)$$

$$\varphi_y = \varphi_\xi \xi_y + \varphi_\eta \eta_y \quad (11c)$$

$$\varphi_{yy} = \varphi_\xi \xi_{yy} + \varphi_\eta \eta_{yy} + \varphi_{\xi\xi} (\xi_y)^2 + 2 \varphi_{\xi\eta} \xi_y \eta_y + \varphi_{\eta\eta} (\eta_y)^2 \quad (11d)$$

$$\varphi_{xy} = \varphi_\xi \xi_{xy} + \varphi_{\xi\xi} \xi_x \xi_y + \varphi_{\xi\eta} \eta_y \xi_x \quad (11e)$$

$$\varphi_{zz} = \varphi_{\zeta\zeta} \quad (11f)$$

Only the term $\varphi_{\xi\xi}$ which results from the φ_{xx} term (Equation 11b) is upwind differenced at supersonic points (see finite difference approximations). All other terms are centrally differenced (11, 21).

The body fine grid system is constructed to completely encapsulate the body or fuselage shape. Figure 6 illustrates the body fine grid arrangement. Fine mesh boundaries are positioned at 10% body length in front of the nose and behind the tail. For special applications, the fine mesh may be concentrated on one particular region for a detailed analysis. Boundaries above, below and on the side are positioned at approximately one average body radius away from the body surface.

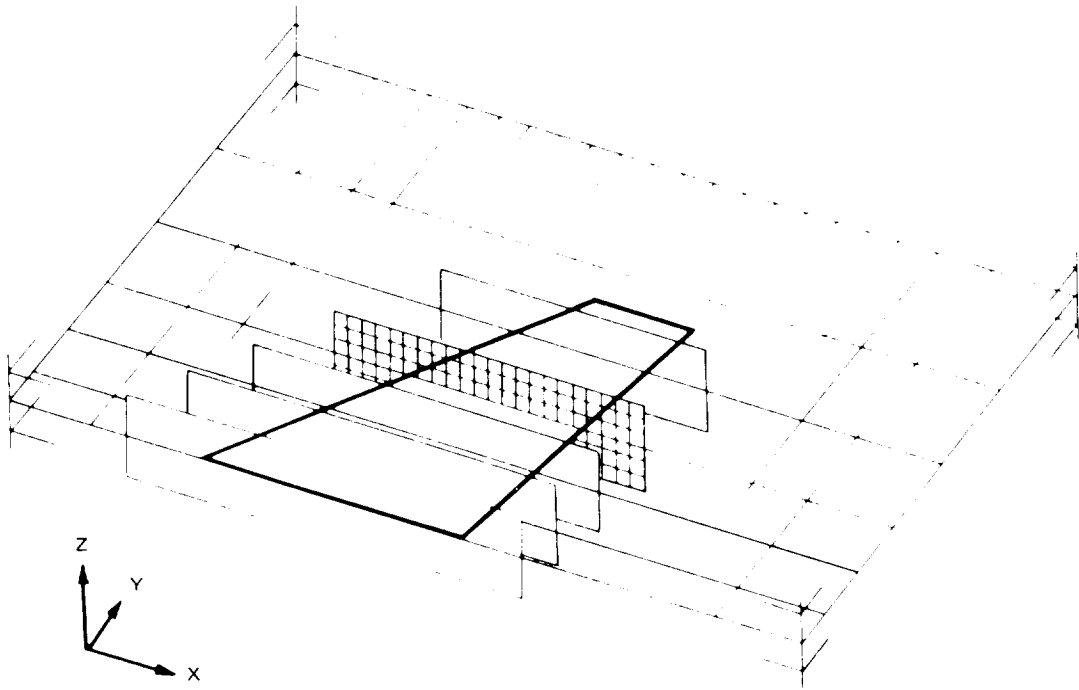


Figure 5 Wing Fine Grid System Embedded in Crude Grid

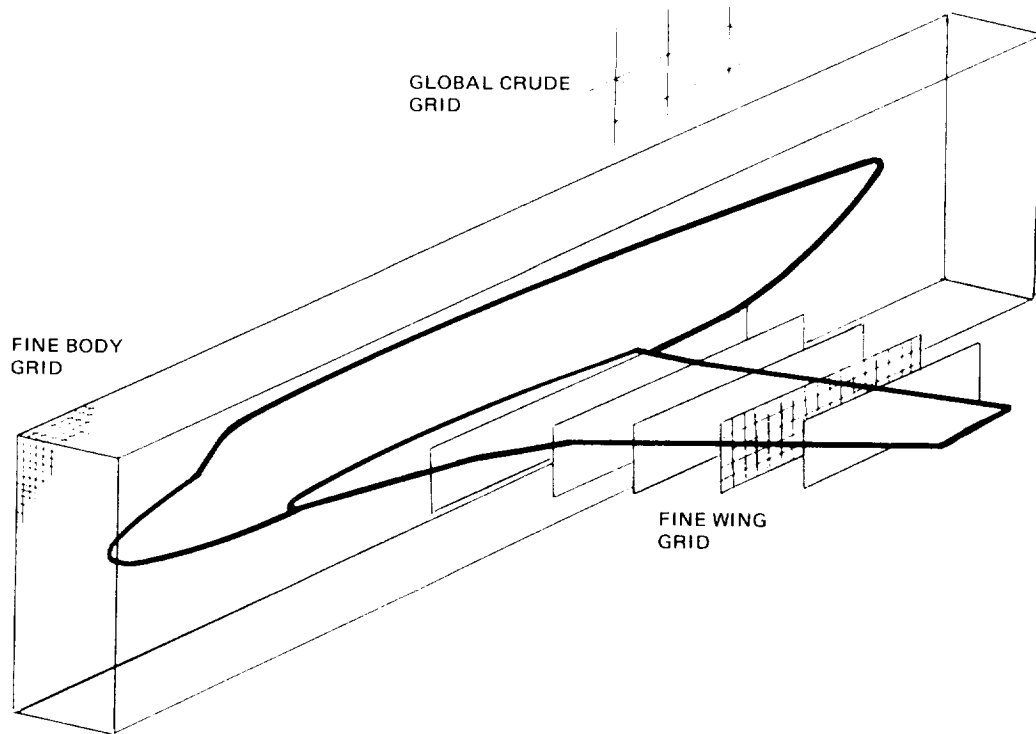


Figure 6 Configuration with Crude Grid and Embedded Fine Grid Systems

As was the case for the individual embedded wing grid systems, the body mesh is evenly spaced in all directions. Transformations are not used. As a result, the flow governing equation (1) is differenced directly. Details of this grid system can be seen in Figure 7. A total of 54,000 points are available in this grid system, which brings the total points in all grid systems combined to approximately 156,000.

Overlap regions in which the flow is computed twice provide a means for interacting the different grid systems. This approach, which also employs combined Dirichlet and Neumann boundary conditions and dummy boundary surfaces, is described in the solution process section.

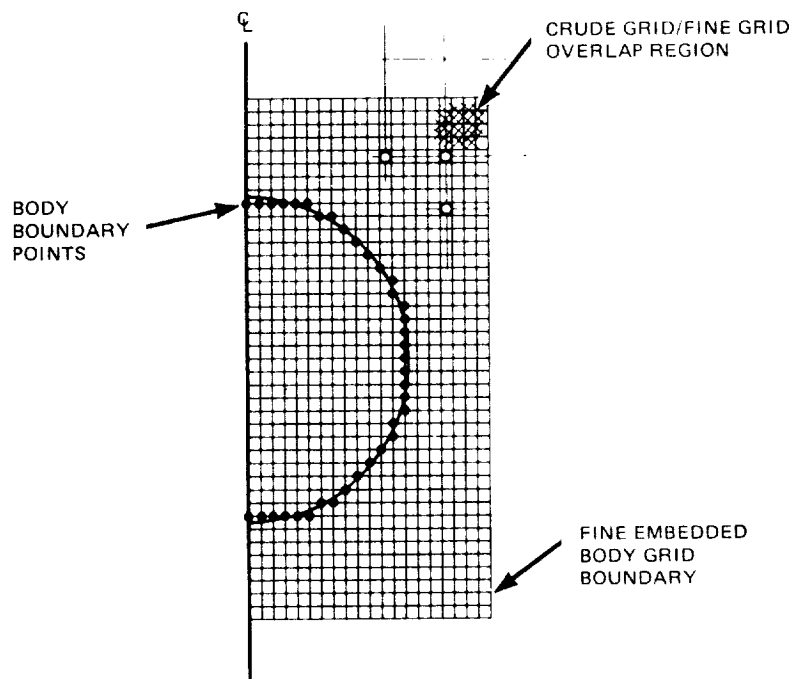


Figure 7 Details of Fine Embedded Body Grid

Finite Difference Approximations

Finite difference approximations* are substituted for the derivatives in equation (1). At each mesh point, the local velocity is computed to determine whether the flow is subsonic (elliptic equation) or supersonic (hyperbolic equation). Equation (1) can be written

$$T \varphi_{xx} + U \varphi_{xy} + V \varphi_{yy} + \varphi_{zz} = 0 \quad (12)$$

where

$$T = 1 - M_\infty^2 - (\gamma + 1) M_\infty^2 \varphi_x - \frac{\gamma + 1}{2} M_\infty^2 \varphi_x^2 \quad (13a)$$

$$U = -2M_\infty^2 \varphi_y \quad (13b)$$

$$V = 1 - (\gamma - 1) M_\infty^2 \varphi_x \quad (13c)$$

The elliptic equation results when

$$DES = U^2 - 4 \cdot T \cdot V < 0 \quad (14)$$

and the hyperbolic equation results for $DES > 0$. With the flow type determined, the appropriate central or upwind difference operator is selected. For subsonic points

$$\varphi_{xx} = \frac{\varphi_{i-1, j, k}^+ - \frac{2}{\omega} \varphi_{i, j, k}^+ - 2 \left(1 - \frac{1}{\omega}\right) \varphi_{i, j, k} + \varphi_{i+1, j, k}}{\Delta X^2} \quad (15)$$

and for supersonic points

$$\varphi_{xx} = \frac{2\varphi_{i, j, k}^+ - \varphi_{i, j, k} - 2\varphi_{i-1, j, k}^+ + \varphi_{i-2, j, k}}{\Delta X^2} \quad (16)$$

Central difference operators are used for all other derivatives regardless of the local flow velocity.

$$\varphi_x = \frac{\varphi_{i+1, j, k} - \varphi_{i-1, j, k}}{2\Delta X} \quad (17a)$$

$$\varphi_y = \frac{\varphi_{i, j+1, k} - \varphi_{i, j-1, k}}{2\Delta Y} \quad (17b)$$

* Finite difference operators are listed for equally spaced grid system only.

$$\varphi_z = \frac{\varphi_{i,j,k+1} - \varphi_{i,j,k-1}}{2\Delta Z} \quad (17c)$$

$$\varphi_{xy} = \frac{\varphi_{i-1,j-1,k}^+ - \varphi_{i-1,j+1,k}^+ - \varphi_{i+1,j-1,k}^+ + \varphi_{i+1,j+1,k}^+}{4\Delta X\Delta Y} \quad (17d)$$

$$\varphi_{yy} = \frac{\varphi_{i,j-1,k} - \varphi_{i,j,k}^+ - \varphi_{i,j,k}^- + \varphi_{i,j+1,k}^+}{\Delta Y^2} \quad (17e)$$

$$\varphi_{zz} = \frac{\varphi_{i,j,k-1}^+ - 2\varphi_{i,j,k}^+ + \varphi_{i,j,k+1}^+}{\Delta Z^2} \quad (17f)$$

The (+) superscript indicates that a new or updated value of the flow field potential is used while no superscript indicates that the value is from a previous sweep or cycle. This procedure enhances the diagonal dominance of the numerical scheme improving the stability of the solution (21, 22).

It should be noted that non-conservative difference operators have been selected. As a result, mass is not conserved across shock waves and the discrepancy or loss increases with increasing shock strength. However, shock waves are weakened in the physical flow field by interaction with the viscous boundary layer. It has been known for some time that nonconservative differencing fortuitously approximates the real flow shock wave strength. Since the present viscous correction method does not have sufficient detail (approximately 41 chordwise boundary layer points) to resolve the details of the true shock-boundary layer interaction, non-conservative difference operators are employed. This should result in a better simulation of the physical flow field.

Wing and Body Boundary Conditions

Surface boundary conditions are enforced on all outer surfaces of the computational space, wing and body surfaces and grid interface regions. Computational space outer boundary requirements were illustrated in Figure 1. Boundary conditions at grid interface regions will be discussed in the solution process section. This section will primarily concentrate on the boundary conditions applied to the wing and body surfaces and the wake potential jump condition.

Boundary conditions are imposed by setting the value of a potential or its first derivative at a field point which represents the configuration surface. The wing and wake are approximated by a planar surface which extends from the wing leading edge to downstream infinity, while the body or fuselage is represented by a fixed cross-sectional surface extending from upstream to downstream infinity. Corrections are applied to the body boundary conditions for the simulation of finite length bodies. Modeling is sufficiently flexible to permit the treatment of wings at varying height relative to the body (high-low-mid-wing).

Special difference approximations are required at boundary points. The planar wing and wake are represented numerically by a grid surface of double valued mesh points (see Figure 8). For a wing surface defined by

$$Z = f(x, y) \quad (18)$$

the wing flow tangency condition is approximated by

$$\varphi_z(x, y, 0) = f_x - \alpha + \delta_x^* \quad (19)$$

where the slope of the boundary layer displacement thickness is added only for the inviscid/viscous interaction mode of operation.

The wing upper and lower surface boundary conditions enter the solution formulation by way of the φ_{zz} term in equation (1). At the wing surface, this term can be written

$$\varphi_{zz} = \frac{1}{\Delta Z} \left[\left(\frac{\varphi_{K+1} - \varphi_K}{\Delta Z} \right) - \left(\frac{\varphi_K - \varphi_{K-1}}{\Delta Z} \right) \right] \quad (20)$$

Note that the I and J subscripts have been dropped for convenience. By incorporating the following relation into equation (20)

$$f_x - \alpha + \delta_x^* = \frac{\varphi_{K+1} - \varphi_{K-1}}{2 \Delta Z} \quad (21)$$

The wing boundary condition on the upper surface becomes

$$\varphi_{zz}(x, y, 0^+) = \frac{2}{\Delta Z} \left[\left(\frac{\varphi_{K+1} - \varphi_K}{\Delta Z} \right) - \left(f_{x_u} - \alpha + \delta_x^* \right) \right] \quad (22)$$

Similarly, the wing lower surface boundary condition becomes

$$\varphi_{zz}(x, y, 0^-) = -\frac{2}{\Delta Z} \left[\left(\frac{\varphi_K - \varphi_{K-1}}{\Delta Z} \right) - \left(f_{x\varphi} - \alpha - \delta_x^* \right) \right] \quad (23)$$

At the end of each sweep of the flow field, the Kutta condition is enforced by calculating the circulation at the trailing edge of the wing section

$$\Gamma = \varphi(X_{TE}, y, 0^+) - \varphi(X_{TE}, y, 0^-) \quad (24)$$

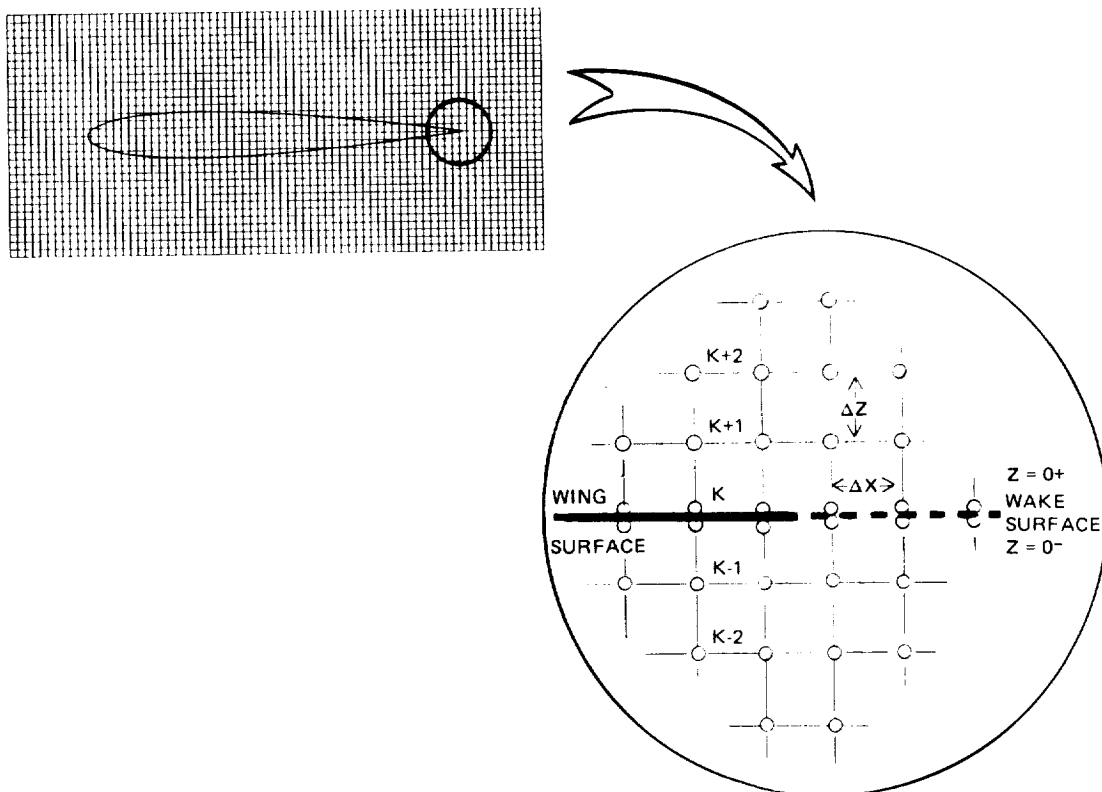


Figure 8 Grid Approximation of Wing and Wake Surfaces

The magnitude of the circulation is determined as part of the solution. The circulation jump condition is enforced along the wake between the wing section trailing edge and downstream infinity. The finite difference approximation for the wake upper surface is

$$\varphi_{zz}(x, y, 0^+) = \frac{\varphi_{K+1} - 2\varphi_K + (\varphi_{K-1} + \Gamma)}{\Delta Z^2} \quad (25)$$

and for the wake lower surface

$$\varphi_{zz}(x, y, 0^-) = \frac{(\varphi_{K+1} - \Gamma) - 2\varphi_K + \varphi_{K-1}}{\Delta Z^2} \quad (26)$$

The use of the shearing transformation (Equation 10-a) for the wing embedded fine grid system complicates the imposition of symmetry conditions for isolated wings and wing root juncture conditions for wing-body combinations. The simple Cartesian (crude) grid symmetry condition (Equation 5a) becomes

$$\varphi_y = \varphi_\xi \xi_y + \varphi_\eta \eta_y = 0 \quad (27)$$

for isolated wings at the symmetry plane and

$$\varphi_y = \varphi_\xi \xi_y + \varphi_\eta \eta_y = F_x \quad (28)$$

for wing-body combinations in the wing root juncture region. Here, F_x represents the slope of the fuselage or body at the wing root.

Computations indicate that numerical instabilities will result if special attention is not given to the selection of difference approximations in this region. These difficulties result from the nature of the shearing transformation. To solve this problem, a plane of dummy mesh points is positioned across the symmetry plane (within the body surface for wing-body configurations) opposite the wing. These flow-field potentials are artificial in the sense that there is no physical flow field associated with them. They simply provide a side boundary of potentials which when used for differencing, produce the proper side condition given by Equation (27) or (28).

A special first order accurate one-sided difference operator is used to generate the dummy interior point potential values. Figure 9 is a schematic which illustrates the mesh point arrangement. For η grid lines which are swept back in the physical plane ($\xi_y < 0$), the following equation is used

$$\varphi_{I, J-1}^D = \frac{\frac{\eta_y}{\Delta\eta} \varphi_{I, J} - \frac{\xi_y}{\Delta\xi} \varphi_{I-1, J-1}^D}{\frac{\eta_y}{\Delta\eta} - \frac{\xi_y}{\Delta\xi}} \quad (29)$$

and for η grid lines which are swept forward ($\xi_y > 0$)

$$\varphi_{I, J-1}^D = \frac{\frac{\eta_y}{\Delta\eta} \varphi_{I, J} + \frac{\xi_y}{\Delta\xi} \varphi_{I+1, J-1}^D}{\frac{\eta_y}{\Delta\eta} + \frac{\xi_y}{\Delta\xi}} \quad (30)$$

Note that the operator changes depending on whether the grid lines are swept forward or backward. In each case, the coefficient of the dummy potential at the point (I, J-1) is larger than the coefficients of other potentials in the difference equation (see ref 23). This enhances the effective diagonal dominance of the system even though the dummy points are not directly relaxed in the conventional sense*.

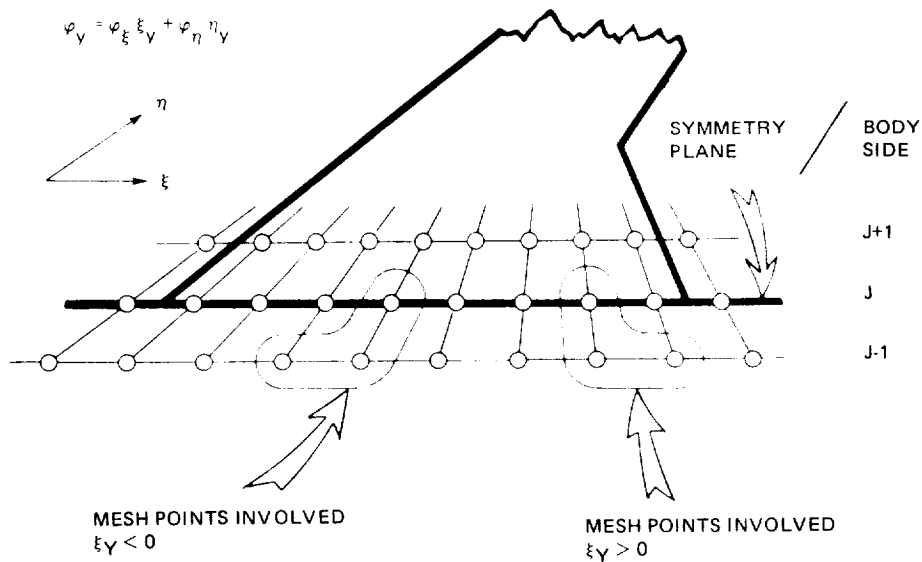


Figure 9 Wing Root Boundary Condition for Dummy Interior Points

*Problem solution provided by J. South, NASA LRC.

Differencing at the wing tip is complicated by the fact that the fine mesh system does not extend beyond the wing tip. Unlike the conventional global transformation approach, the coordinate lines do not have to be unswept or unsheared far from the wing. Provisions must be made, however, for properly ending the fine grid computation at the wing tip. For this reason, another temporary fine mesh is positioned just beyond the wing tip. Like its neighboring fine grid on the wing, this grid array is located at a crude mesh Y-line. Its extent in the streamwise and vertical directions is consistent with the fine grid system on the wing. Both the dummy plane beyond the wing root and the temporary fine grid beyond the wing tip are computed for each sweep of the array of fine grid structures. While the root dummy plane is computed using difference formulas, equations (29) and (30), the tip plane is simply filled using linear interpolation and potentials from the crude Cartesian grid.

A computational surface represents the true body surface in the Cartesian grid systems. For axisymmetric bodies, the computational shape is an infinite cylinder with a radius equal to the true body maximum radius. For wing-body configurations the shape takes the form of the body cross-section in the wing-body juncture region. Figure 10 is a schematic illustrating the true and computational body surfaces. This approach proves to be more economical and stable than "fitting" the body boundary points to the true body shape in the axial direction. This approximation is probably consistent with the planar wing/wake surface and the small disturbance approach in general.

Body boundary conditions are imposed by computing appropriate flow field potentials at points near the body surface (body computational surface). The flow field is relaxed, holding these values fixed during each iteration cycle. No attempt is made to position mesh lines so points fall near the body surface. The mesh density is sufficiently detailed to provide a good hands-off representation of the cross-sectional shape (see Figure 7). For a body shape defined by

$$F(x, y, z) = 0 \quad (31)$$

The small-disturbance boundary condition is

$$F_x + F_y \varphi_y + F_z \varphi_z = 0 \quad (32)$$

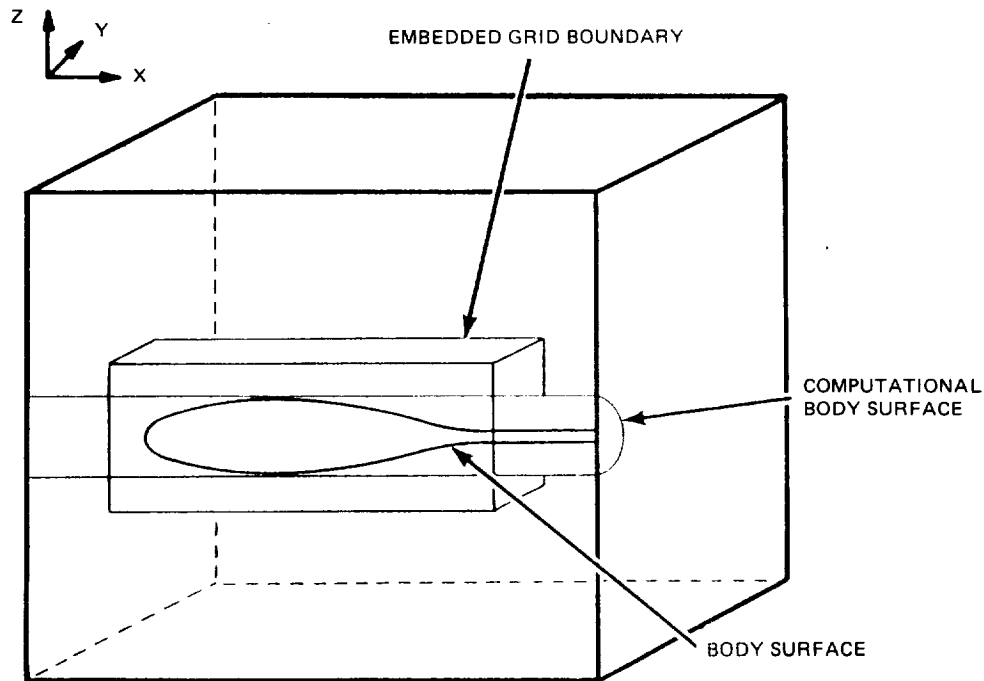


Figure 10 Computational and True Body Surfaces

Following Bailey and Ballhaus ⁽¹⁰⁾, three-point extrapolated differences are substituted for the flow velocities in Equation (32). The body/mesh arrangement for a typical body point is illustrated in Figure 11.

Between the nose and tail of the body, there are sections where the true body surface and the computational body surface are not aligned. This is illustrated in Figure 10 and can be seen on a sectional basis in Figure 11. To ensure a proper representation of the true body shape, a correction must be applied to the boundary condition on the computational surface. The boundary condition correction will account for the displacement effect. Similarly, flow velocities computed on the computational surface must be corrected to yield velocities and pressures on the true body surface. Slender body theory provides the required modifications*.

* Boundary condition displacement corrections provided by Professor Jack Werner, Polytechnic Institute of New York ⁽²⁴⁾.

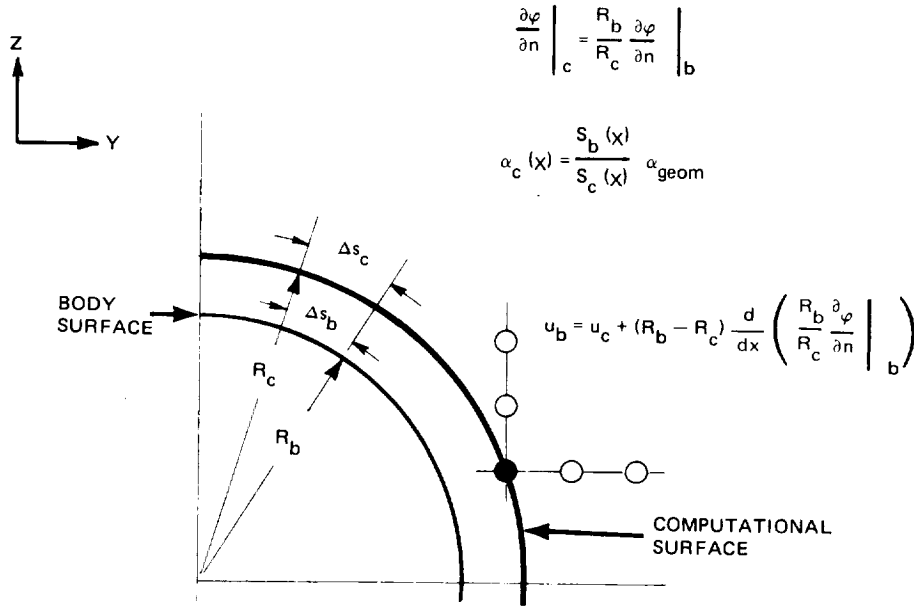


Figure 11. Details of Body Surface Approximation

The effects of body thickness and incidence lead to separate corrections. Body thickness effects can be approximately represented by a source distribution, the strength of which is proportional to the rate of change of body area. The boundary condition on the computational surface can be obtained by requiring that the net source strength across both surfaces be identical at each cross-sectional cut.

$$\int_c \varphi_n ds_c = \int_b \varphi_n ds_b \quad (33)$$

As a result, the correct global effect of the true body shape on the remainder of the flow field will be obtained. This leads to

$$\varphi_n \Big|_c = \frac{\Delta s_b}{\Delta s_c} \varphi_n \Big|_b \quad (34)$$

In the present method, cross-sectional shapes are taken to be circular or near-circular in character. Equation (34) is approximated by

$$\varphi_n \Big|_c = \frac{R_b}{R_c} \varphi_n \Big|_b \quad (35)$$

A similar correction can be obtained for effects caused by flow incidence or angle-of-attack. In this case equivalent doublet strengths are enforced where doublet strength is proportional to the cross-sectional area S .

$$\alpha_{\text{eff}} S_c (X) = \alpha_{\text{geom}} S_b (X) \quad (36)$$

An effective angle-of-attack is obtained for each sectional cut. The angle-of-attack imposed on the computational surface becomes

$$\alpha_c (X) = \frac{S_b (X)}{S_c (X)} \alpha_{\text{geom}} \quad (37)$$

By substituting three-point extrapolated differences for the velocities in the body boundary condition (Equation 32) and adding the thickness correction (35) and the angle-of-attack correction (37), the following expression for body boundary points is obtained

$$\varphi_{c_j, k} = \frac{A}{B} \quad (38)$$

where

$$A = N_x \frac{R_b}{R_c} + \frac{N_y}{2\Delta y} (4 \varphi_{j+1, k} - \varphi_{j+2, k}) \quad (38.1)$$

$$+ N_z \left(\frac{4 \varphi_{j, k+1} - \varphi_{j, k+2}}{2\Delta z} + \alpha_{\text{geom}} \frac{S_b}{S_c} \right)$$

and

$$B = \frac{3}{2} \left(\frac{N_y}{\Delta y} + \frac{N_z}{\Delta z} \right) \quad (38.2)$$

Note that the I subscripts have been eliminated for clarity.

Solution Process

Conventional finite difference relaxation schemes employ a procedure which is known as "Grid Halving". A solution is obtained using a very crude mesh. The grid is halved (mesh points are twice as dense) and the crude mesh potentials provide an initial flow field for what is now a medium mesh. The medium mesh solution is used for a mesh system which is halved once again for the final fine grid solution. Convergence is accelerated because flow disturbances naturally propagate faster in a crude grid than in a fine grid.

The present method does not employ grid halving, however, an initial solution is obtained using only the global crude grid system. This quickly establishes the general character of the flow field and provides a starting flow for the detailed embedded grid systems. Final results are obtained by a simultaneous solution in all grid systems, both crude and fine. It is required then, that the different grid systems interact. This interaction is made possible by mesh overlap regions in which the flow is computed twice during each cycle.

Successive Line Over-Relaxation (SLOR) is used, vertical columns of mesh points are relaxed starting at the first point upstream and ending at the last point downstream in each grid system. The solution process for isolated bodies and wings will be described first followed by the solution process for wing-body combinations.

Isolated Body Solution Process.

Phase 1: The body is represented by crude mesh points and an initial solution is obtained in the global crude grid. Typically, 50 iterations are sufficient. Crude grid potentials (ϕ) in the crude/fine grid overlap region (see Figure 7) provide a starting flow for the embedded fine grid. Linear interpolation is employed.

Phase 2 (Step No. 1): The embedded body grid is swept holding fine grid perimeter points fixed forming an outer boundary. Body boundary points are computed and they form an inner boundary (see Figure 12). Body boundary potential values are computed using Equation (38).

(Step No. 2): The crude grid points which make up the inner boundary of the overlap region are updated based on fine grid potentials obtained in step No. 1. The global crude grid is swept holding these potential values fixed as an inner boundary. Infinity boundary conditions (Figure 1) at the limits of the computational space form an outer boundary. Crude grid potentials are now used to update fine grid perimeter points. Step No. 1 is repeated

Phase 2 proceeds by repeating Steps 1 and 2 until both grid systems are converged. Typically, 50 cycles are sufficient. Body pressure coefficients are computed using body boundary potentials in the fine grid system.

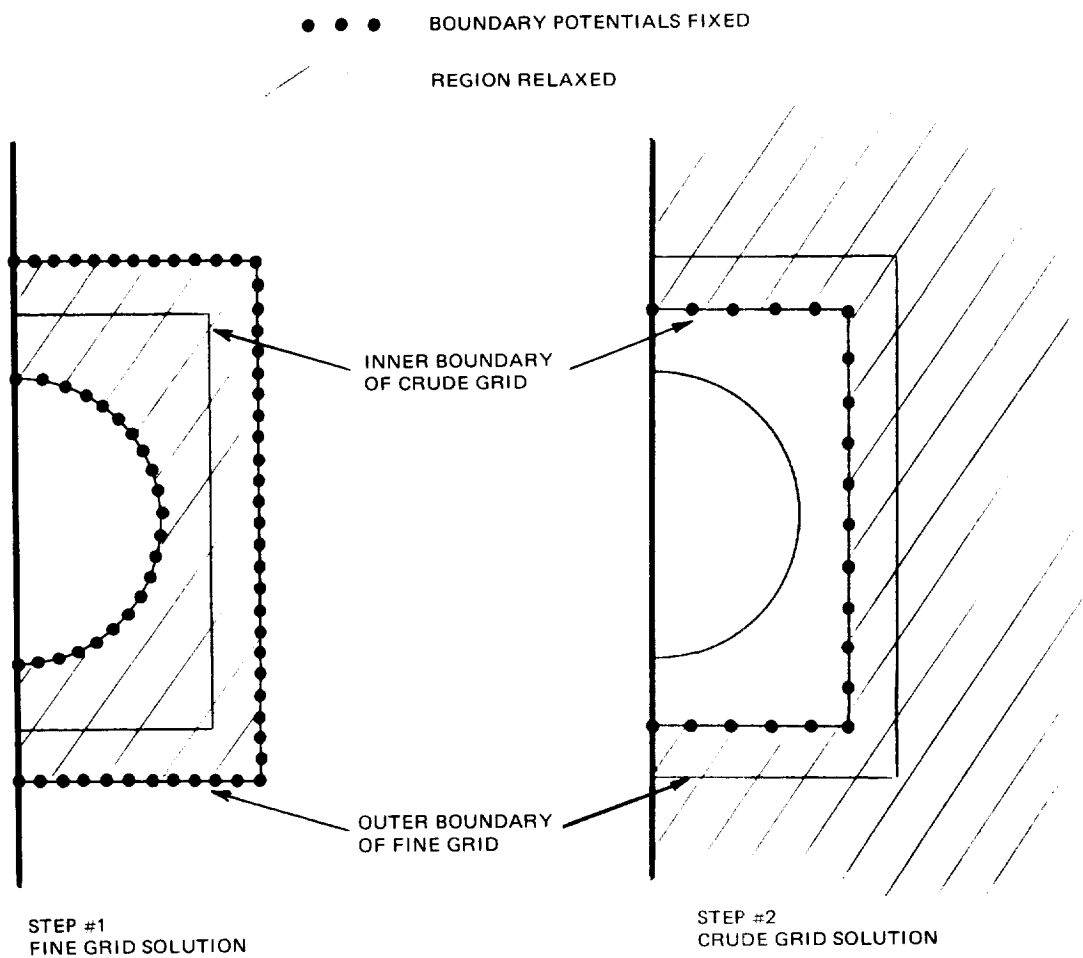


Figure 12. Phase 2 Isolated Body Crude/Fine Grid Solution Process

Isolated Wing Solution Process. The isolated wing solution process is similar to that of the body. However, the entire fine embedded grid region is now the overlap region. In addition, side boundaries at the wing root and tip must be computed.

Phase 1: The wing is represented by crude mesh points which fall randomly on the planform (see Figure 2). An initial solution is obtained using the crude mesh, typically 100 iterations are sufficient*. Using linear interpolation, crude grid potentials in the crude/fine overlap region (see Figures 3 and 4) provide a starting flow field for the fine embedded grid.

Phase 2 (Step No. 1): The embedded wing grid is swept holding fine grid perimeter points fixed as an outer boundary (see Figure 13). Conventional Neumann boundary conditions (φ_n) are imposed at fine grid section boundary points forming an inner boundary.

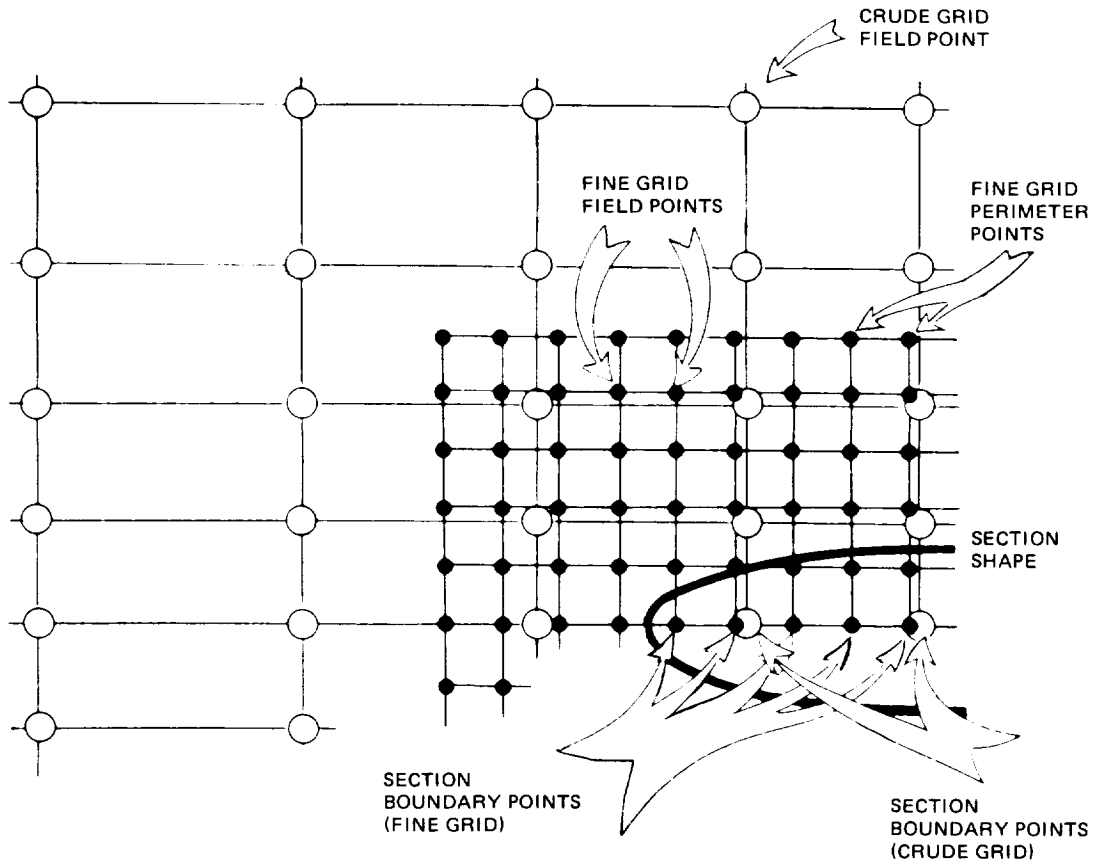


Figure 13. Wing Section Crude/Fine Grid Interface

*See recommendations for usage section (pg. 148) for additional comments on iteration count and convergence.

(Step No. 2): The crude grid section boundary points are computed using the potentials at the fine grid section boundary points (linear interpolation). These crude potentials (φ) are held fixed for the global crude grid sweep forming an array of dirichlet (φ) inner boundary conditions. Once again, infinity boundary conditions at the limits of the computational space form the outer boundary. At the end of the crude grid sweep, crude grid potentials are used to update the fine grid perimeter points. Step No. 1 is repeated.

Phase 2 proceeds by repeating Steps 1 and 2 until both grid systems are converged. Typically, 80 cycles are sufficient. Wing pressure coefficients are computed using wing boundary potentials in the fine grid system.

Wing-Body Solution Process. The wing-body solution process combines the procedures which are described for isolated bodies and isolated wings. In addition, however, a scheme for interacting two fine grid systems (embedded wing fine and body fine) is necessary. Figure 14 is a schematic illustrating the overlap of the three different grid systems involved.

Phase 1: An initial solution is obtained with the wing-body configuration represented in the crude mesh. Typically, 100 iterations are sufficient. Crude grid potentials are used to fill both wing and body embedded grid systems.

Phase 2: (Step No. 1) As was the case for isolated wings, the wing fine grid is swept using conventional Neumann boundary conditions at fine grid section boundary points.

(Step No. 2) As was the case for isolated bodies, the body fine grid is swept with perimeter points and body boundary points fixed. An additional surface representing the wing and wake is also held fixed (see Figure 15). Flow field potentials representing the wing/wake surface are obtained from the fine embedded wing grid.

(Step No. 3) The global crude grid is swept with interior boundary points provided by the fine wing and body grid solutions. At the end of the crude grid sweep, crude grid potentials are used to update fine body grid perimeter points and fine wing grid perimeter points outside the fine body grid region (recall Figure 14). Within this region, fine body grid potentials are used to update fine wing grid perimeter points. Step No. 1 is repeated.

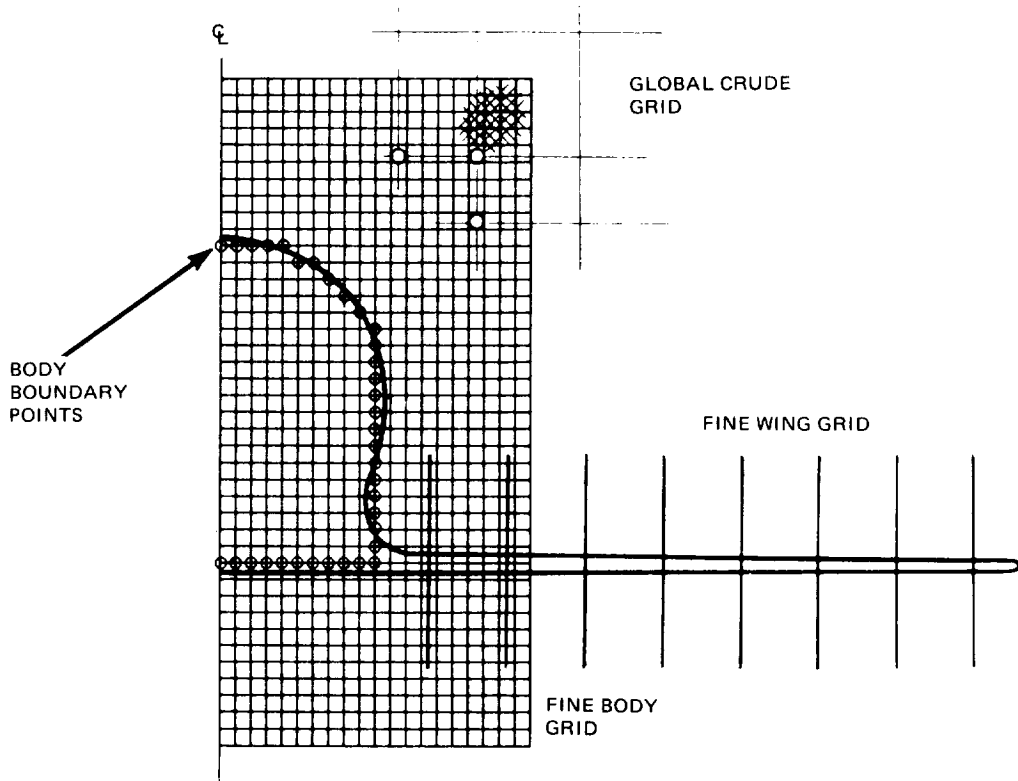


Figure 14. Three Different Grid Systems for Wing-Body Solution

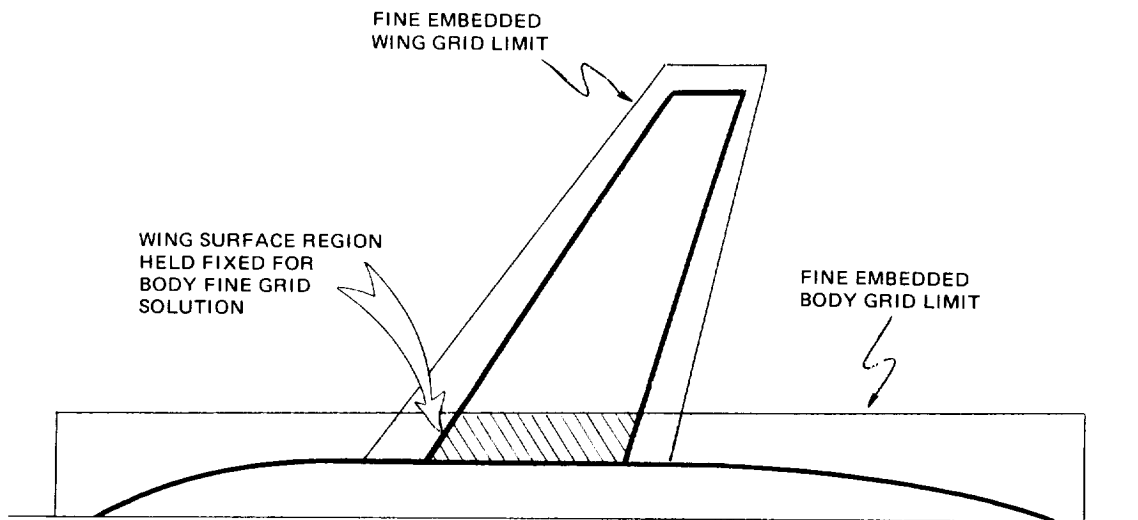


Figure 15. Fixed Wing Surface Region for Embedded Body Grid Solution

Phase 2 proceeds by repeating Steps No. 1, 2 and 3 until all grid systems are satisfactorily converged. Typically, 80 cycles are sufficient.

The development of the solution in all cases is monitored by calculating the maximum update to the flow field potential ($\varphi^+ - \varphi$) and its position in the three-dimensional flow field. Typically, for most configurations at flow conditions which are of interest, this maximum $\Delta\varphi$ value will start near 0.5×10^{-1} and end near 0.5×10^{-4} for the final solution. Large regions of supersonic flow will slow this converging process since difference approximations at supersonic points are only first order accurate while those at subsonic points are second order accurate. Most important, however, the position of this maximum flow field correction will be useful in pinpointing the problem area when convergence is hindered. Problem areas may develop when the flow conditions are extreme or when the geometric representation is in error.

Body/Fuselage Geometry Model

The present method provides a means for analyzing truly arbitrary body shapes at transonic speeds. Thus, it is occasionally required that complex three-dimensional geometries be input, processed and converted into a suitable array of boundary conditions for the analysis scheme. Since the input or modeling of complex body shapes is extremely error prone and certain applications might not warrant this level of effort, several options have been provided for describing body or fuselage shapes.

- Option No. 1 Cylinder - A cylinder extending from upstream infinity to downstream infinity approximates the body shape. Only a radius need be input. This simple approach may be suitable for certain wing-fuselage applications (no body force or moment computed).
- Option No. 2 Axisymmetric Body - Only an array of X and R coordinates need be input. This option is particularly advantageous when analyzing simple research test configurations.
- Option No. 3 Arbitrary Fuselage - This option is necessary in most realistic aircraft applications, particularly when flow details about fuselage contours (canopies, blisters and fairings) are required.

This section describes the mathematical modeling system which is employed for processing arbitrary fuselage shapes (Option No. 3). The system has been named "Quick-Geometry" by its developers, Vachris and Yaeger⁽²⁵⁾. A detailed User's Guide for the Quick-Geometry System can be found in the Appendix of ref 26. This system was originally developed for the geometric modeling of wing-body shapes. Since only fuselage shapes are of concern here, many of the more sophisticated options including fillets and patches will not be described in the paragraphs which follow. In addition, if ref 25 and 26 are being used to augment the modeling description provided herein, it should be noted that the input format has been modified to be more consistent with that of the basic transonic wing-body code.

The geometry package requires that certain body lines and cross-section lines be defined. The body lines and cross-section lines may be likened to the stringers and bulkheads, respectively, used in fuselage construction. These line models are defined by a combination of simple curves (i.e., lines, ellipses, cubics). They are taken together to provide a continuous analytical model of the surface geometry. Slopes and normals are developed analytically. Either discontinuous intersections or smooth fairings can be modeled and enforced.

Two different coordinate systems are employed. Geometry definition is performed in a Cartesian coordinate system (x, y, z), while interrogation of the model for body boundary conditions is performed in cylindrical coordinates (X, R, θ). This results in the use of a plane of symmetry map axis, the height of which usually corresponds to the position of the max-half-breadth line. It is required that the configuration radius at any cross-sectional cut be a single valued function of the angle θ . These definition lines and coordinate systems are illustrated in Figure 16.

From this description, it should be apparent that a minimum of four body lines are required for the simplest fuselage. These are 1) top centerline, 2) bottom centerline, 3) max-half-breadth line, and 4) the map axis. Each body line must be defined by both its Y and Z values over the full range of X (between fuselage nose and tail). Similarly, a minimum of two cross-section line segments are required for each different cross-section line model. These are 1) body upper, and 2) body lower.

Both body lines and cross-section lines are specified by defining key arc or segment shapes and their accompanying limiters. The segment shape boundary conditions that are used to determine the coefficients of the shape equation are the

(1) origin point, (2) termination point, and (3) slope control point. The slope control point lies at the intersection of the line which is tangent to the segment shape at the origin point and the line which is tangent to the segment shape at the termination point (see Figure 17). The slope control point is a very convenient way of specifying slope conditions. In particular, it allows for the simultaneous specification of slope conditions at both ends of the segment.

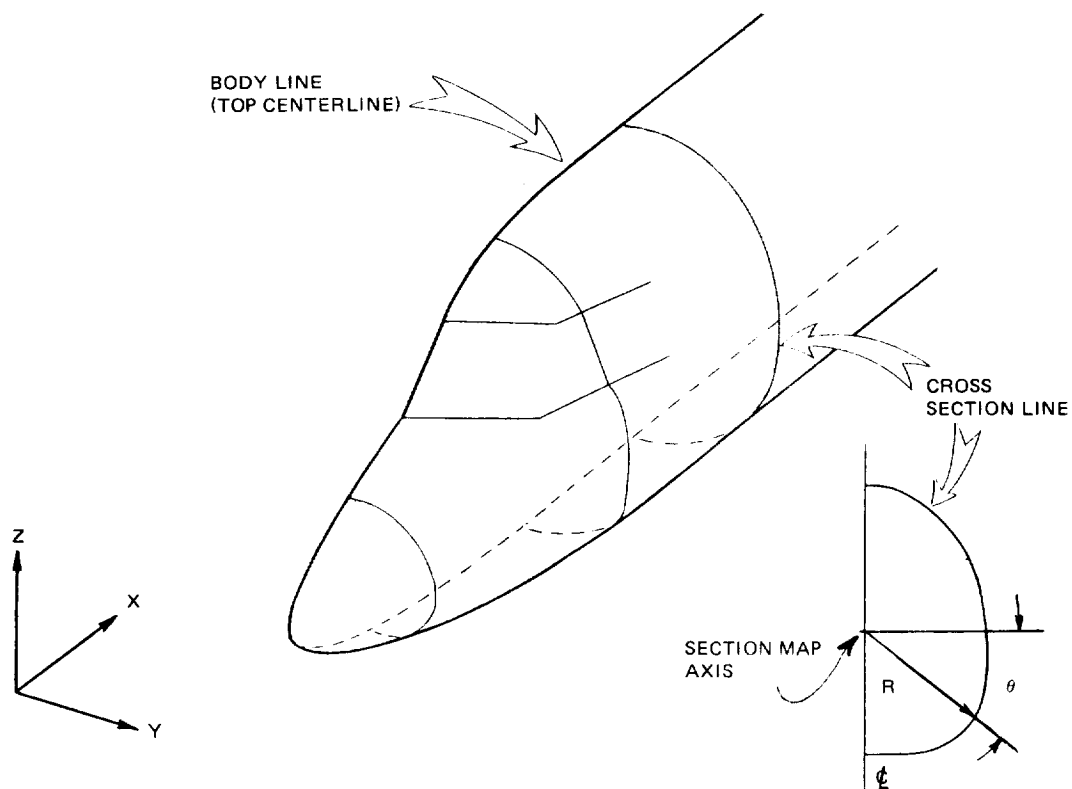


Figure 16. Geometry Model Lines and Coordinate Systems

The arc shapes used for defining a cross-section line model are listed in Table 1.

TABLE 1. Cross-Section Arc Shapes

Shape	Keyword	Equation
Line	LINE	$Ay + Bz + C = 0$
Ellipse (Concave to origin)	ELLI	$\frac{(y - y_0)^2}{A^2} + \frac{(z - z_0)^2}{B^2} = 0$
Ellipse (Convex to origin)	ELLO	Same as ELLI

They are input in an order which starts at the body bottom centerline and proceeds to the body top center line. The segment shapes used for defining a body line model are listed in Table 2.

TABLE 2. Body Line Segment Shapes

Shape	Keyword	Equation
Line	LINE	$Ax + By = 0$
X-PARABOLA	XPAR	$Ax + By + y^2 = 0$
Y-PARABOLA	YPAR	$Ax + By + x^2 = 0$
X-ELLIPSE	ELLX	$Ax + By + Cx^2 + y^2 = 0$
Y-ELLIPSE	ELLY	$Ax + By + Cy^2 + x^2 = 0$
CUBIC	CUBI	$Ax + By + Cx^2 + x^3 = 0$

Cross-section arcs are input in their order of appearance. However, body line segments are defined along with an index which establishes their order in the x-direction. In addition, body lines may be aliased to other body lines to avoid duplicate definitions.

It should be noted that cross-sections are defined only in terms of named component arcs (arc shape table) and named control points. On the other hand, body lines are defined mathematically by coordinates over the length of the configuration for which they are required. At a given x-station, the body lines are interrogated to give the key control points required to construct the cross-sectional arcs.

Figure 17 is a schematic illustrating the component build-up of a particular body line and cross-section line model. Naturally, LINE segments do not require a slope control point. In this case, the portion of the body top center line illustrated requires four body line segments and the cross-section is constructed with two arcs (two is the minimum number allowed).

Figure 18 illustrates an array of cross-section lines and the body lines for a typical transport fuselage shape. Five different body lines can be identified. These body lines form the limiters for the three distinct cross-section models. This geometry package has proven to be particularly useful when coupled with the mesh embedding scheme since the fine grid structure may be placed for analysis purposes about any region of interest in addition to totally encapsulating the body shape. Figure 19 illustrates the surface geometry produced when the mathematical model is interrogated

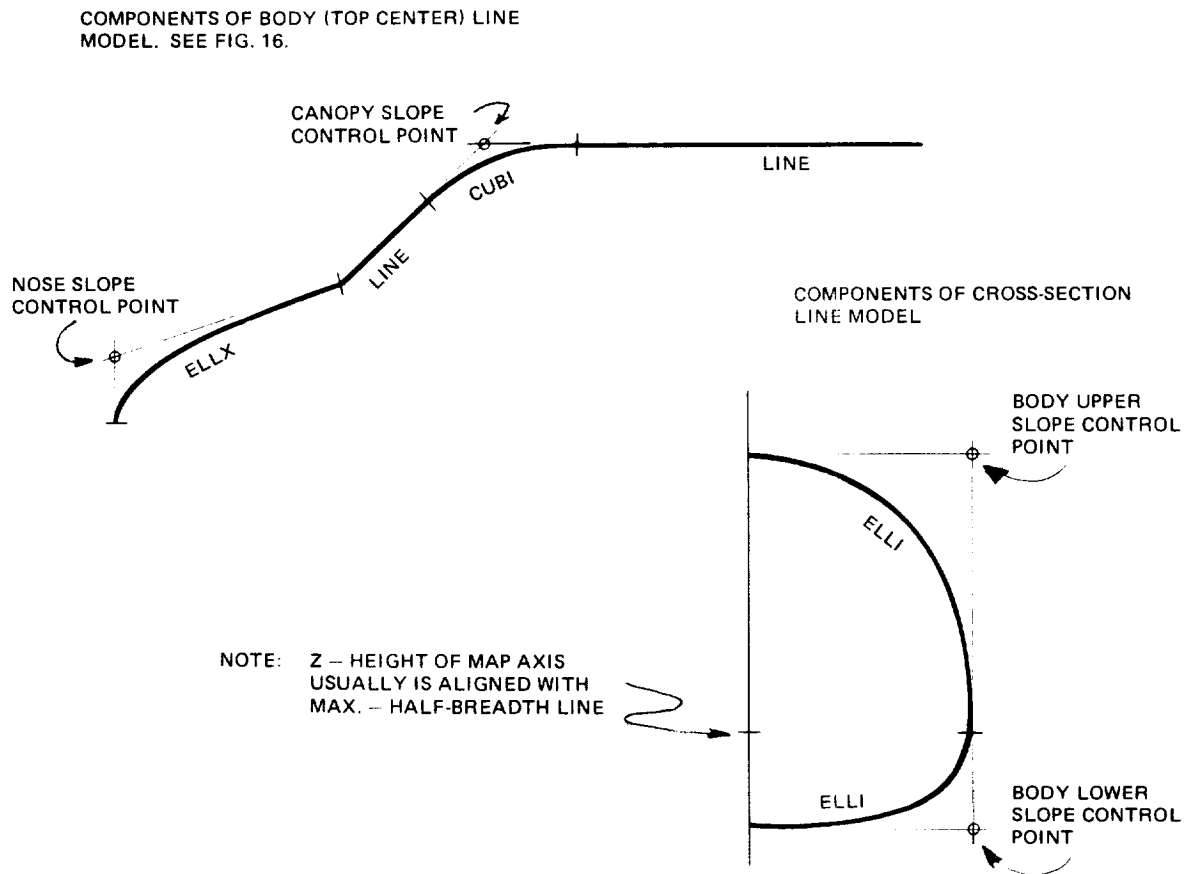


Figure 17. Components of Body and Cross-Section Line Models

for a fine embedded mesh system. Boundaries of this region were outlined in Figure 18. Note that the mathematical model does not change in this case, only the region over which the model is interrogated for boundary conditions and the surface shape. The input data set for this geometry can be found in the Appendix (page 109 and computed results can be seen in the Results Section (page 59).

Figure 20 illustrates an array of cross-section lines and the body lines for an area-ruled transport fuselage shape. Here, only four body line models and one cross-section model were required. The cross-sectional shape has been varied from circular to flat bottomed simply by changing the position of the max-half-breadth line.

The geometry modeling procedures described in the preceding paragraphs can best be interpreted by studying a sample fuselage shape. Table 3 lists the geometric model for the transport nose-windshield-canopy shape illustrated in Figure 19. Lines C through S make up the cross-section line model input while lines T through FFF describe the body line models. Note that there are three distinct cross-section line

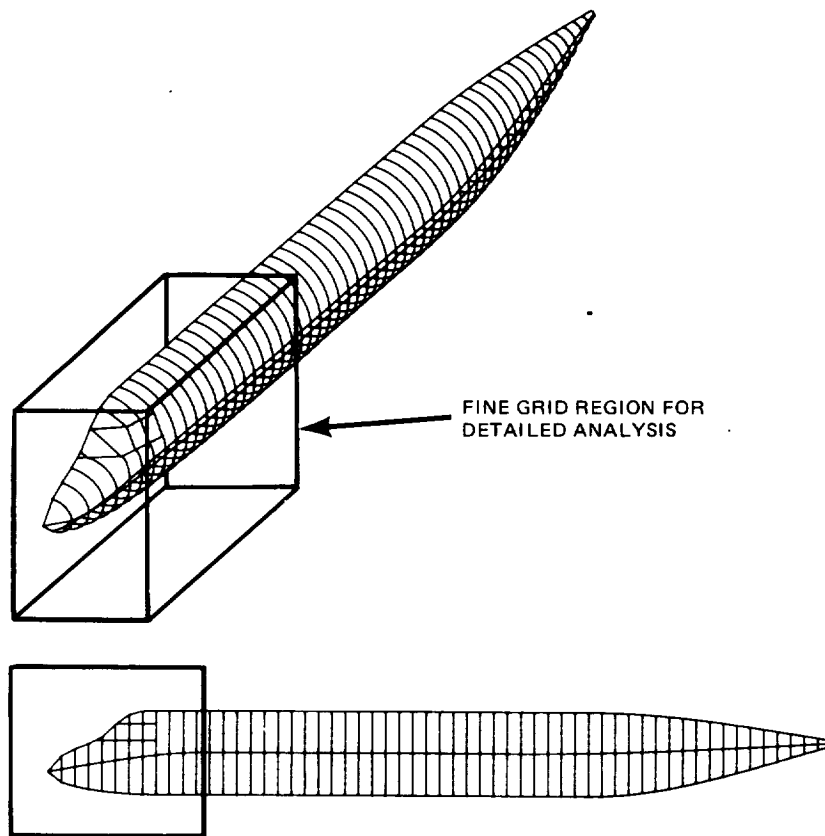


Figure 18. Crude Grid Interrogation of Complete Geometry Model

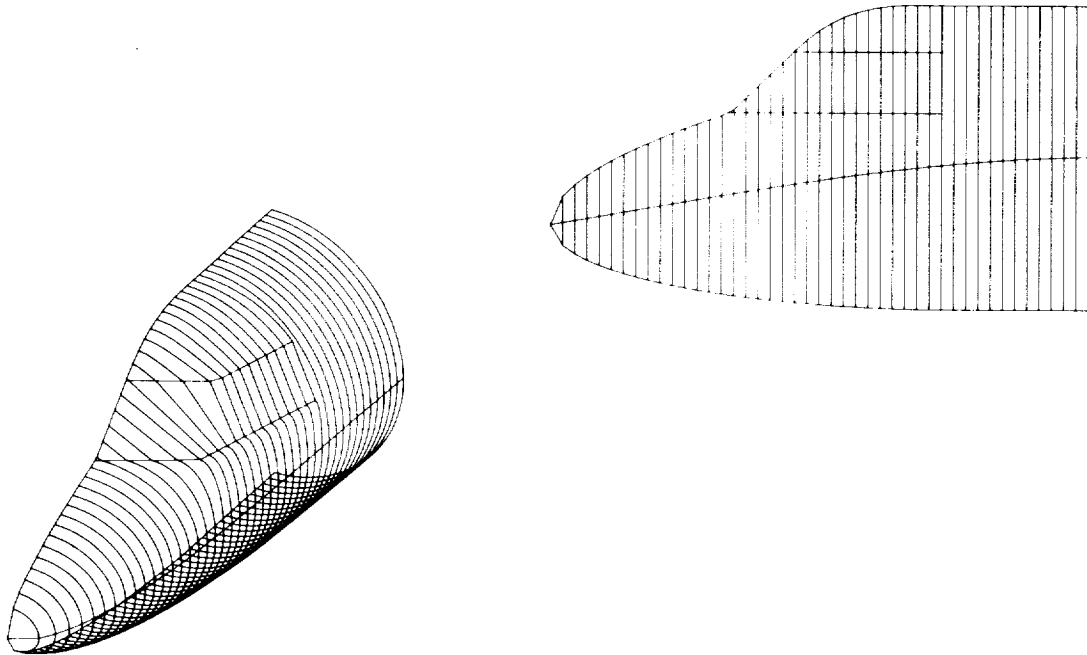


Figure 19. Fine Grid Region Interrogation of Geometry Model

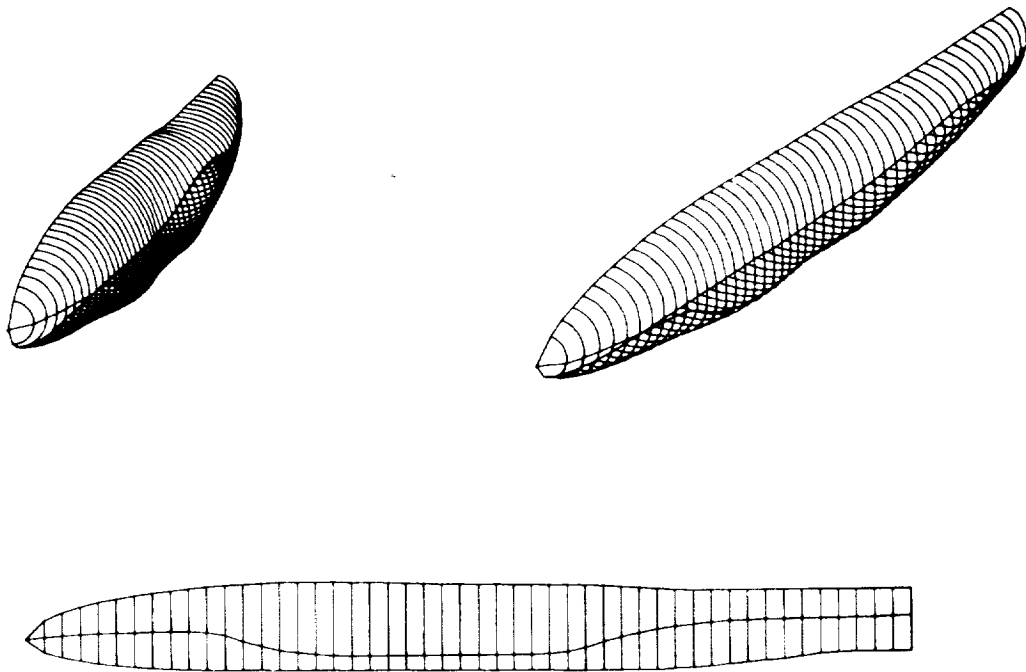


Figure 20. Geometry Model for Area-Ruled Fuselage

TABLE 3. Gulfstream Fuselage Quick-Geometry Model

					LINE		
3.							A
1.							B
BODYLO	2.	NOSE TO WINDSHIELD BASE					C
	ELLI	BDYBCL	BDYMH	BDYLSCP			D
BODYHI	ELLI	BDYMHB	BDYTCL	BDYUSCP			E
2.							F
CANLC	3.	WINDSHIELD					G
	ELLI	BDYBCL	BDYMHB	BDYLSCP			H
CANSI	ELLI	BDYMHB	CANLCW	CANLSCP			I
WINDF	LINE	CANLOW	BDYTCL				J
3.							K
CANOPLO	4.						L
	ELLI	BDYBCL	BDYMHB	BDYLSCP			M
CANOPSI	ELLI	BDYMHB	CANLOW	CANLSCP			N
WINDSI	LINE	CANLOW	CANHIE				O
CANOPUP	ELLI	CANHIE	BDYTCL	CANTSCP			P
4.							Q
1.	1.	8.0	64.0				R
2.	2.	64.0	83.5				S
3.	3.	83.5	133.0				T
4.	1.	133.0	200.0				U
10.	11.						V
2.	ZBDYBCL						W
FLLX	8.0	78.5	133.0	53.0	8.0	53.0	X
LINE	133.0	53.0	200.0	53.0			Y
4.	ZBDYTCL						Z
FLLX	8.0	78.5	64.0	113.5	8.0	94.5	AA
LINE	64.0	113.5	83.5	132.5			BB
CUBI	83.5	132.5	133.0	147.0	98.0	147.0	CC
LINE	133.0	147.0	200.0	147.0			DD
1.	YCENTER						EE
LINE	8.0	0.0	200.0	0.0			FF
2.	ZBDYMHB						GG
CUBI	8.0	79.5	181.0	100.0	135.5	100.0	HH
LINE	181.0	100.0	200.0	100.0			II
1.	YBDYMHB						JJ
FLLX	8.0	0.	200.0	47.0	8.0	47.0	KK
1.	ZCANLOW						LL
LINE	64.0	113.5	133.0	113.5			MM
1.	ZCANHIE						NN
LINE	83.5	132.5	133.0	132.5			OO
2.	YCANLOW						PP
LINE	64.0	0.	79.5	28.0			QQ
LINE	79.5	28.0	133.0	42.0			RR
2.	YCANHIE						SS
LINE	83.5	0.	96.0	24.5			TT
LINE	96.0	24.5	133.0	34.0			UU
1.	YCANTSCP						VV
LINE	83.5	0.	133.0	22.0			WW
	ZMAPAXIS	ZBDYMHB					XX
	YMAPAXIS	YCENTER					YY
	ZCANTSCP	ZBDYTCL					ZZ
	ZCANLSCP	ZCANLOW					AAA
	YCANLSCP	YBDYMHB					BBB
	YBDYTCL	YCENTER					CCC
	YROYBCL	YCENTER					DDD
	YBDYLSCP	YBDYMHB					EEE
	ZBDYLSCP	ZBDYBCL					FFF
	YBDYUSCP	YBDYMHB					
	ZBDYUSCP	ZBDYTCL					

models (lines C-E, F-I, and J-N). Line group P-S provides the region over which each cross-section line model is to be applied. Most important however, note that line S indicates that the same cross-section model is to be used for both the nose and fuselage body.

Lines T through FFF indicate that ten body lines are required for this fuselage shape. Each is described in both y and z values over the range of x for which they are required. This leads to twenty different models along with the y center line used for aliasing. Ten are defined by inputting section shape and limiters (lines U-UU) and eleven are aliased to them (lines VV-FFF).

As one might expect, it is very easy to make errors when defining complex three-dimensional shapes. Various diagnostic checks have been incorporated into the method to simplify this process. First, geometry verification plots are available to illustrate the defined surfaces using cross-section lines. Second, a diagnostic print-out is available for checking both the coefficients of the shape equations and the proper range of definition for body segments. Finally, the sample cases provided in the Appendix should provide a foundation of experience upon which a user can build.

Wing Viscous Effects

Wing viscous effects (C_{Df} , δ^*) are computed in the present method by coupling a modified Bradshaw boundary layer computation with the aforementioned finite difference potential flow scheme. The boundary layer method provides details of the thin viscous layer close to the surface given the wing pressure distributions from the global inviscid calculation. Several modes of operation are provided for tailoring the computation for various applications and minimization of computing requirements.

- Mode No. 1 Wing viscous effects including skin friction drag component (C_{Df}) and boundary layer displacement thickness (δ^*) are not computed. Inviscid solution only. Minimum computer resources required.
- Mode No. 2 Wing viscous effects are computed at the end of the inviscid solution providing an approximation to C_{Df} and δ^* . Permits subtraction of B. L. δ^* for design work done inviscidly to get physical or constructed wing shape (approximately 7% computing time increase over Mode No. 1).

Mode No. 3 Coupled inviscid/viscous interaction solution. Iterative scheme for simultaneous solution of boundary layer and potential flow (approximately 30% computing time increase over Mode No. 1).

Examples of viscous flow phenomena occurring on wings have been sketched in Figure 21. In particular, an aft-loaded or supercritical wing section shape has been illustrated. Details of the shock wave/boundary layer interaction are not computed by the present method. This effect includes both a local thickening of the boundary layer and a weakening of the shock wave strength. Instead, non-conservative finite differences of the flow equation have been selected which somewhat fortuitously approximate the shock weakening phenomena. The global boundary layer displacement thickness effects are predicted by the present method. For aft-loaded wing sections or wings with control surface deflections, this effect can have a dramatic effect on wing loading and shock wave positions. As illustrated in Figure 21, an asymmetric boundary layer build-up results in a net decambering effect. For Mode 3 operation, this effect is incorporated into the solution automatically.

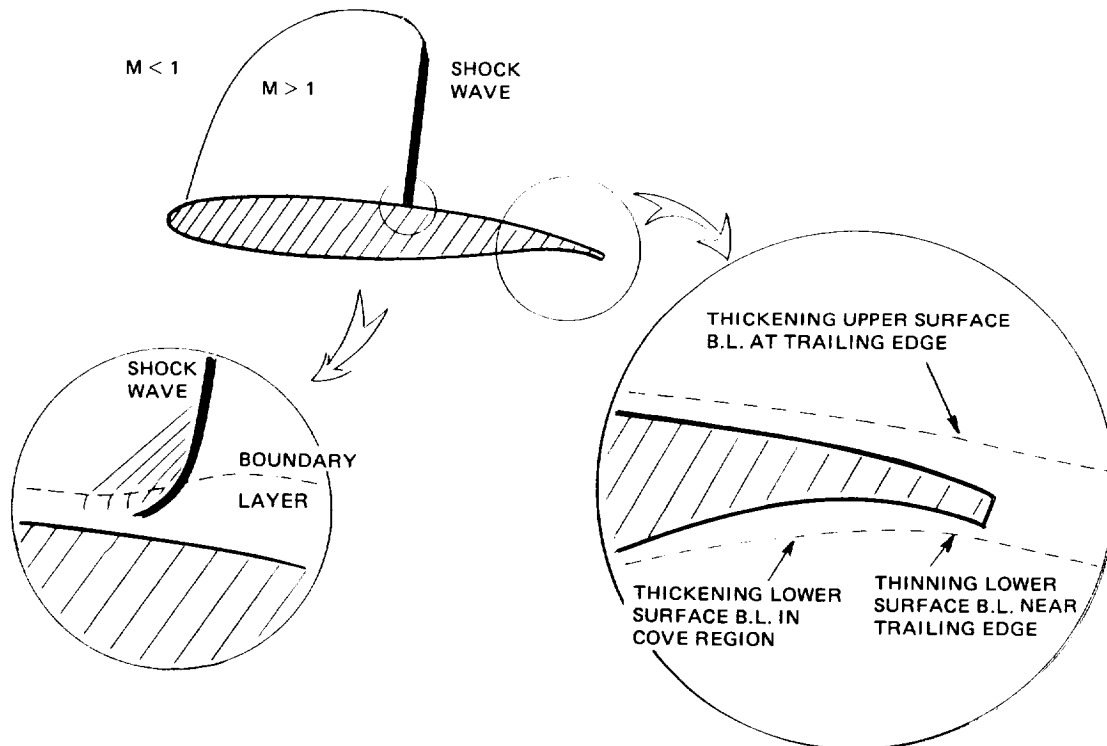


Figure 21. Wing Section Viscous Effects

The modified chord technique of Nash & Tseng⁽²⁷⁾ is used in the present method. Developed by Mason⁽²⁸⁾, this particular technique permits a two-dimensional boundary layer method to be extended to the three-dimensional case provided that the flow does not deviate far from the infinite sheared wing type. The coordinate system for this sheared wing approximation can be seen in Figure 22. The wing sweep angle is taken to be that of the mid-chord span line. As a result, the local boundary layer computations vary with the wing planform shape, see Figure 23. This quasi-three-dimensional approach has been selected because it requires about an order of magnitude less computing time as compared to a full three-dimensional boundary layer calculation. This is an important consideration when coupling with three-dimensional transonic flow methods is being investigated.

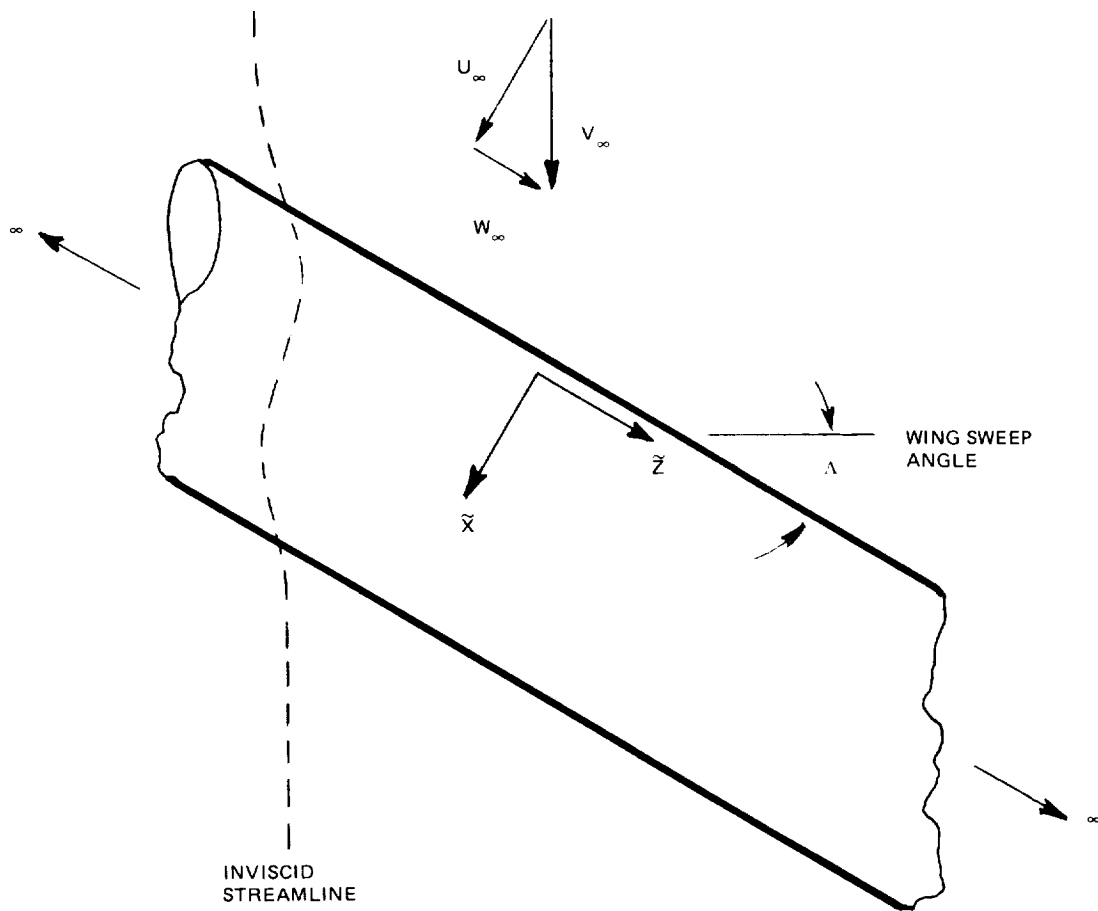


Figure 22. Infinite Sheared Wing Coordinate System

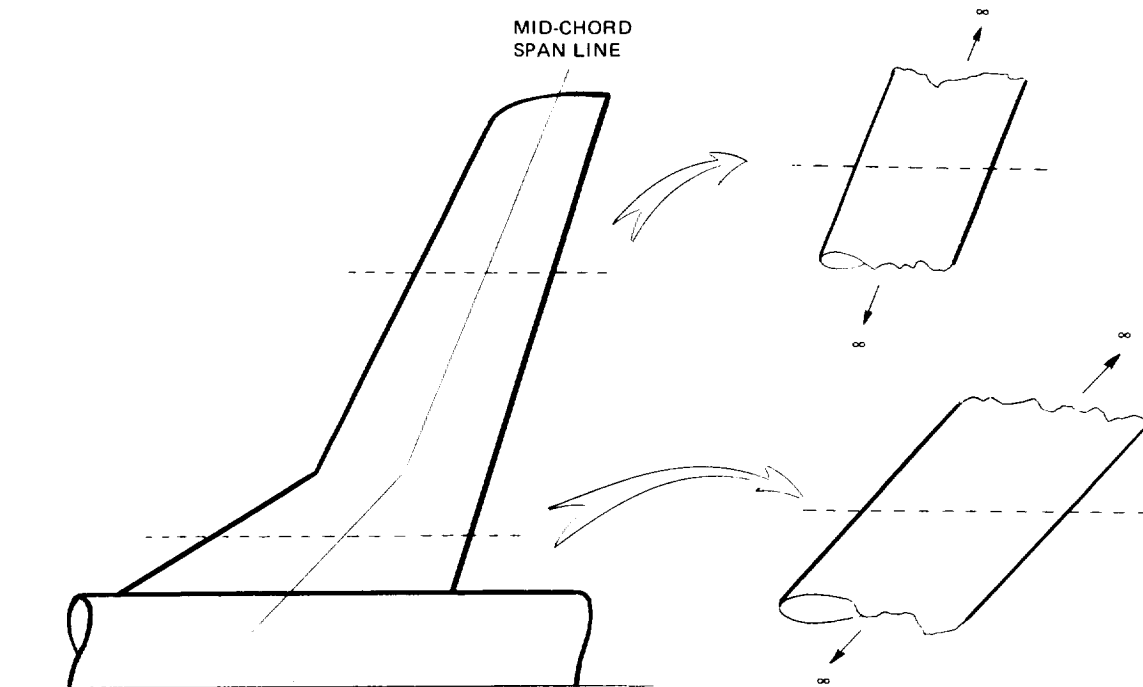


Figure 23. Wing Viscous Effects Approximated by Infinite Sheared Wing Approach

The Bradshaw turbulent boundary layer method ⁽²⁹⁾ provides the foundation for this scheme with the laminar boundary layer predicted by Thwaites method modified for compressible flow. Several corrections are required for simulation of three-dimensional effects. The modifications of Nash and Tseng ⁽²⁷⁾ for incompressible flow about an infinite yawed wing are employed. In particular, it was noted that, A) pressure gradient effects on boundary layer development were properly accounted for by a 2-D calculation performed in the chordwise \tilde{x} direction and similarly, B) shear stress direction and magnitude could be represented by a 2-D calculation in the streamline direction (see Figure 22). Nash has shown that the equation for the chordwise shear stress component is similar to the conventional 2-D equation.

$$\frac{\tau_{\tilde{x}}}{\rho U_e} = \cos[\tan^{-1} \frac{We}{U_e}] \tau = \lambda \tau \quad (39)$$

Here it is assumed that λ varies slowly in the \tilde{x} -direction compared to the shear stress change.

The computation requires an effective Reynolds number which is obtained by requiring that the shear component in the \tilde{x} -direction bear the same relationship to an effective Reynolds number that the actual shear stress has to the specified Reynolds number. This is accomplished by using the Reynolds number based on the momentum thickness at transition in the Karman-Schoenherr formula. The transition point has been fixed at the 5% chord position in the coding of the method. Of course, this may be modified or varied by changing the coding. However, this variation is not provided as an input option.

Finally, a method is required to compute the solution in the spanwise direction. It is assumed that $\tau_{\tilde{z}}$ can be related to $\theta_{\tilde{z}}$ by a flat plate skin-friction formula. In this case, the Squire-Young formula is used.

$$\frac{\tau_{w\tilde{z}}}{\rho_{\infty} W_{\infty}^2} = \frac{1}{[5.89 \log_{10} (4.075 \overline{\text{Re}} \frac{\theta_{\tilde{z}}}{c})]^2} \quad (40)$$

NOTE: $\overline{\text{Re}}$ based on W_{∞} and effective chordwise viscosity of Nash.

The boundary layer computation will stop when flow separation is predicted ($\tau_{\tilde{x}} = 0$). At this point, the slope of the displacement thickness boundary is extrapolated to the trailing edge. This will permit the calculation to proceed, however, it should be noted that deviations between computed results and the real flow will result if separation points before the 96 to 97% chord position are encountered.

The interaction solution (coupled viscous/inviscid) requires that the boundary layer computation be performed during the solution development. The computed boundary layer displacement thickness slopes are added to the wing geometric surface slopes to provide an equivalent inviscid wing shape for analysis by the inviscid scheme. Note that in the present small-disturbance method, only the boundary condition slopes are modified. The planar wing boundary surface does not change.

Many wing shapes which are of practical interest have section shapes with cove regions. This includes the supercritical type wing section shapes and occasionally conventional sections when control surfaces are deflected. Of course, it is possible for cove type shapes to exist on the wing upper or lower surface. The existence of this type of geometry coupled with extreme flow conditions can become a problem during the solution process if cove type flow separations are encountered. Typically,

the boundary layer becomes thicker in the cove region and thins out toward the trailing edge (see Figure 21). If separation is encountered, the boundary layer computation will stop and the character of the displacement thickness effect will be lost. In this case, the section lift may be significantly in error which will lead to a poor numerical simulation. To relieve this problem, an empirical relation developed by Bavitz⁽³⁰⁾ is employed to provide an approximation to the cove displacement thickness. This will make it possible for the computation to continue.

Bavitz's empirical relation is based on an extensive correlation study of supercritical type airfoils. It involves the pressure coefficients and displacement thickness at four points along the section surface. These points have been illustrated in Figure 24. The first point is positioned 10% chord upstream of the separation point. The second point is 8% chord before separation, the third point is midway between the separation point and the trailing edge, and the final point lies at the trailing edge.

The boundary layer displacement thickness at stations 3 and 4 are computed using using the following equations:

$$\frac{\delta^*}{c} \Big|_3 = \frac{\delta^*}{c} \Big|_1 + 0.019 (C_{P_3} - C_{P_1}) - 0.022 \left(\frac{x}{c} \Big|_3 - \frac{x}{c} \Big|_1 \right) \quad (41)$$

$$\frac{\delta^*}{c} \Big|_4 = \left(\frac{\delta^*}{c} \Big|_1 + \frac{\delta^*}{c} \Big|_3 \right) / 2 \quad (42)$$

A third degree polynomial is fit to the four δ^* values to provide the boundary layer shape between the separation point and the trailing edge. The pressure difference coefficient in Equation (41) was set at 0.033 for computations involving two-dimensional airfoils. Calculations performed on several supercritical wings, however, indicated that a lower value would be better for the three-dimensional case. As a result, the 0.019 coefficient is used in the present method.

It should be noted that this empirical relation only provides an approximation to the cove region boundary layer when shallow separations are encountered. In many cases, this approximation may be sufficient to establish the proper wing lift level and the final solution in the cove region may be fully attached (empirical correction not used). If this is the case, a valid solution has probably been obtained. If on the other

hand, the final solution still indicates cove separation is present, it is likely that the physical flow is separated and agreement between theory and experiment may be poor.

In the present method, the empirical correction is employed if separation is encountered and the trailing edge angle is less than -4° or greater than $+4^\circ$. For trailing edge angles within these boundaries, the conventional procedure is used beyond the separation point. In other words, the sum of the δ^* and local wing slopes at the separation point is enforced as the wing boundary condition between the separation point and the wing trailing edge. Viscous effects are incorporated by using an under-relaxation factor of 0.6. This factor should be reduced if boundary layer instabilities are encountered.

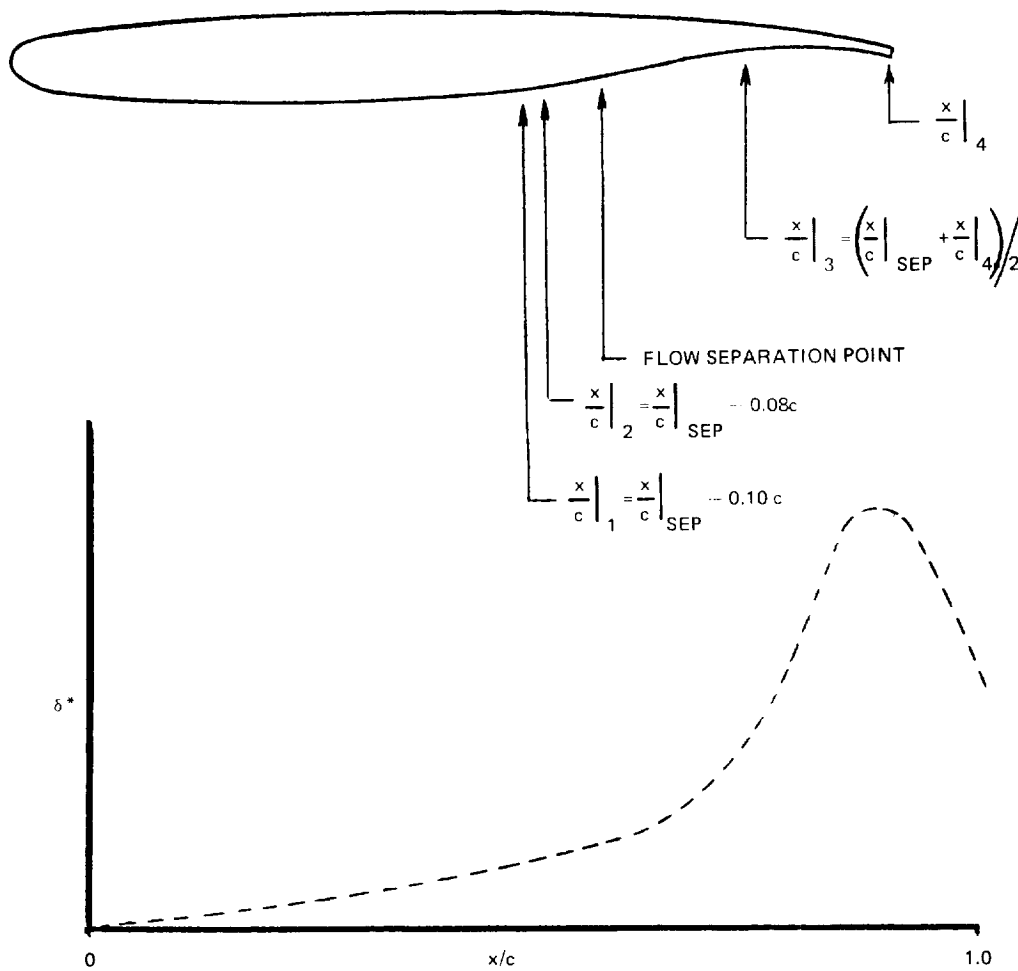


Figure 24. Bavitz Empirical Relation Points

Pressure, Force, and Moment Coefficients

Force (except wing friction) and moment coefficients are obtained by integrating computed pressure coefficients. Wing pressure coefficients are computed by using central difference operators for velocity components (Equations 17a, b) and then pressure coefficients from Equation 2. With 100 grid points between each section leading and trailing edge, this provides pressure output every 1% chord beginning at 0.005c.

Body pressure coefficients are computed in a similar manner except that a correction must be applied in regions where the computational body surface and the true body surface are not aligned. The velocity or pressure distribution corrections are similar to those developed for the body boundary conditions (Equation 38). Both apply only in regions where there is a displacement between the computational body surface and the actual body surface. Velocity components on the computational surface are obtained with central difference operators at body boundary points. The velocity on the true body shape is then approximated by

$$u_b = \varphi_x \Big|_b = \varphi_x \Big|_c + \frac{\partial}{\partial r} (\varphi_x)_c \delta r \quad (43-A)$$

where

$$\delta r = R_b - R_c \quad (43-B)$$

Since the flow is continuous in this region, (Equation 43-A) may take the form

$$\varphi_x \Big|_b = \varphi_x \Big|_c + \frac{\partial}{\partial X} \left(\frac{\partial \varphi}{\partial r} \right)_c \delta r \quad (44-A)$$

$$\varphi_x \Big|_b = \varphi_x \Big|_c + \frac{\partial}{\partial X} \varphi_n \Big|_c \delta r \quad (44-B)$$

Using (Equation 35) the body surface velocity becomes

$$u_b = u_c + (R_b - R_c) \frac{d}{dX} \left(\frac{R_b}{R_c} \varphi_n \Big|_b \right) \quad (45)$$

Body surface pressures are now computed using a central difference operator (Equation 17a) for the surface velocity (Equation 45) which is substituted into the pressure equation (Equation 3).

Configuration force, moment, and loading coefficients require reference areas and lengths as a basis. These reference values are taken from the input geometric wing planform shape. A typical wing planform has been sketched in Figure 25. Note that the wing is specified to the plane of symmetry even for the wing-body case. The following parameters are computed using the defined wing planform.

$$AR = \frac{b^2}{S_w} \quad (46)$$

$$C_{av} = \frac{S_w}{b} \quad (47)$$

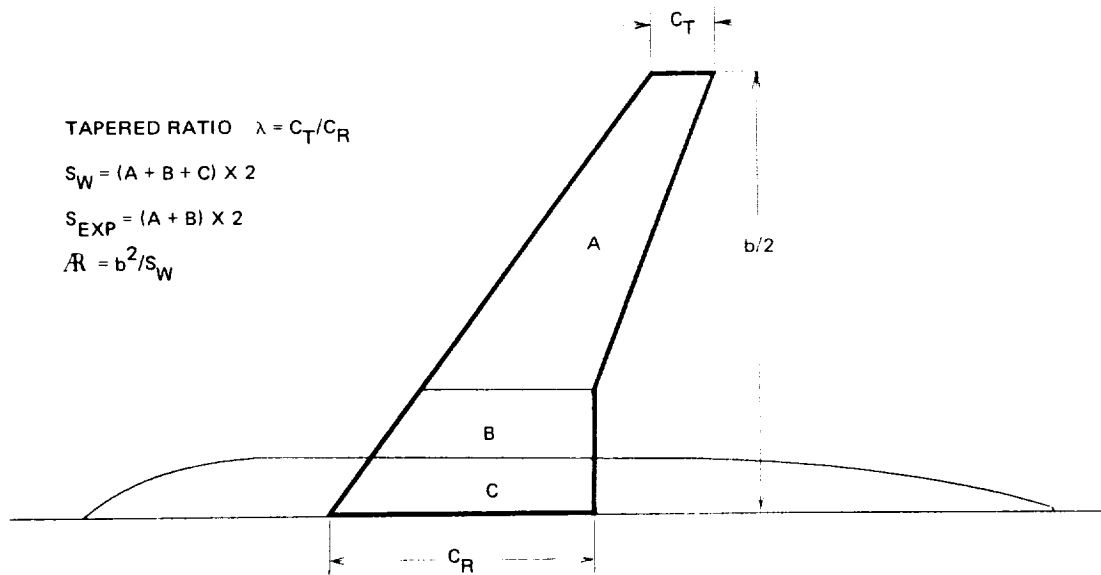


Figure 25. Wing Planform Parameters

$$\text{M.A.C.} = \frac{2}{3} C_R \left(\frac{1 + \lambda + \lambda^2}{1 + \lambda} \right) \quad (48)$$

Wing section coefficients are obtained by integrating the upper and lower surface pressure coefficients along the chord.

$$C_{\ell\omega} = -\frac{1}{C_{loc}} \int_0^c (C_{P_u} - C_{P_\ell}) dx \quad (49)$$

$$C_{m\omega} (loc) = \frac{1}{C_{loc}^2} \int_0^c (C_{P_u} - C_{P_\ell}) (X_{loc} - X_{c/4}) dx \quad (50)$$

$$C_{d\omega} = \frac{1}{C_{loc}} \int_0^c \left[C_{P_u} \left(\frac{dz_u}{dx} - \alpha \right) - C_{P_\ell} \left(\frac{dz_\ell}{dx} - \alpha \right) \right] dx \quad (51)$$

In addition, a sectional moment about the axial reference position is computed.

$$C_{m\omega} = \frac{1}{\text{M.A.C.} \cdot C_{loc}} \int_0^c (C_{P_u} - C_{P_\ell}) (X_{loc} - X_{REF}) dx \quad (52)$$

The wing lift coefficient is obtained by integrating the spanwise load coefficients.

$$C_{LWING} = \frac{2}{b} \int_0^{b/2} \left(\frac{C_{loc} C_{\ell\omega}}{C_{av}} \right) dy \quad (53)$$

Note that for wing-body combinations, all integrals in the spanwise direction start at the wing-body juncture instead of the symmetry plane which is the case for an isolated wing. In addition, the computed spanwise integrals are scaled by S_{EXP}/S_W for the wing-body case.

The wing moment coefficient is computed in a similar manner.

$$C_{MWING} = \frac{2}{b} \int_0^{b/2} \left(\frac{C_{loc} C_{m\omega}}{C_{av}} \right) dy \quad (54)$$

Wing skin friction drag is computed by integrating the shear stress coefficients computed by the boundary layer analysis. At each wing station, a local section skin friction coefficient is computed.

$$C_{f_{\omega}} = \int_0^c [\tau_{\tilde{x}} \cos \Lambda_{loc} + \tau_{\tilde{z}} \sin \Lambda_{loc}] dx \quad (55)$$

The \tilde{x} and \tilde{z} sheared wing coordinate system was illustrated in Figure 22. Total wing skin friction drag is then obtained by integrating the local friction coefficients along the span.

$$C_{F_{WING}} = \frac{2}{b} \int_0^{b/2} \left(\frac{C_{loc} C_{f_{\omega}}}{C_{av}} \right) dy \quad (56)$$

The wing pressure drag coefficient:

$$C_{D_{P(w)}} = \frac{2}{b} \int_0^{b/2} \left(\frac{C_{loc} C_{d_{\omega}}}{C_{av}} \right) dy \quad (57)$$

is added to the skin-friction drag coefficient to obtain the total wing drag coefficient.

$$C_{D_{WING}} = C_{F_{WING}} + C_{D_{P(w)}} \quad (58)$$

Body coefficients are obtained by integrating surface pressure distributions and adding a skin friction component based on total body wetted area. A body cross-sectional force coefficient distribution is computed first.

$$C_{\ell_b} = -\frac{1}{R_{loc}} \int_0^{R_{loc}} [C_{P_{UPPER}} \cdot N_z] dy - \frac{1}{R_{loc}} \int_0^{R_{loc}} [C_{P_{LOWER}} \cdot N_z] dy \quad (59)$$

and

$$C_{d_b} = \frac{1}{R_{loc}} \int_0^{R_{loc}} [C_{P_{UPPER}} \cdot N_x] dy + \frac{1}{R_{loc}} \int_0^{R_{loc}} [C_{P_{LOWER}} \cdot N_x] dy \quad (60)$$

The longitudinal coefficients are then integrated along the length of the body.

$$C_{L\text{BODY}} = \frac{1}{L} \int_0^L \left[\frac{C_{\ell_b} \cdot R_{loc}}{R_{max}} \right] d\ell \quad (61)$$

Similarly

$$C_{M\text{BODY}} = \frac{1}{L^2} \int_0^L \left[\frac{C_{\ell_b} \cdot R_{loc}}{R_{max}} \right] (x_{loc} - x_{REF}) d\ell \quad (62)$$

and

$$C_{D\text{P}(b)} = \frac{1}{L} \int_0^L \left[\frac{C_{d_b} \cdot R_{loc}}{R_{max}} \right] d\ell \quad (63)$$

The body moment coefficient (62) is scaled by L/M.A.C. for the wing-body case.

The reference position about which moments are computed is taken to be the center of the body for isolated bodies and the input moment center for the wing-body case. In addition, the integrated coefficients are based on reference areas which are a function of the case. For isolated bodies, the maximum cross-sectional area becomes the reference area while for wing-body configurations, the wing plan form reference area is used. For isolated bodies, equations (61-63) are scaled by S_{BP}/S_{BASE} and for wing-body combinations, the equations are scaled by S_{BP}/S_W

The body skin friction coefficient is computed using the Prandtl-Schlichting formula

$$C_{F\text{BODY}} = \frac{0.455}{[\log(Re_\ell)]^{2.58}} \quad (64)$$

corrected for compressibility effects. Here, Re_ℓ is the Reynolds number based on body length. Total body drag is then computed.

$$C_{D\text{BODY}} = C_{F\text{BODY}} + C_{D\text{P}(b)} \quad (65)$$

Total configuration force and moment coefficients are obtained by adding the wing and body components.

$$C_L = C_{L\text{WING}} + C_{L\text{BODY}} \quad (66a)$$

$$C_M = C_{M\text{WING}} + C_{M\text{BODY}} \quad (66b)$$

$$C_D = C_{D\text{WING}} + C_{D\text{BODY}} \quad (66c)$$

Configuration lift induced drag (C_{D_I}) is computed by first determining the span-wise loading efficiency factor (E). This is accomplished by means of fast Fourier analysis applied to the configuration span load distribution. The lift induced drag component is then computed using the following equation.

$$C_{D_I} = \frac{C_L^2}{\pi A E} \quad (67)$$

The wave drag is then computed by subtracting the lift induced drag from the total integrated pressure drag given by (Equations 57 and 63).

$$C_{D\text{WAVE}} = C_{D_P(\omega)} + C_{D_P(b)} - C_{D_I} \quad (68)$$

It is important to note that the body, wing, and wing-body force and moment coefficients are based on reference areas and lengths taken from the input geometry. These values are listed as part of the program output. Sometimes it is required that configuration force and moment coefficients be based on reference values other than those provided by the physical wing and body shape. If this is the case, and case 8 is a good example, it will be necessary to scale the computed coefficients by the ratio of the two reference values. If A is the reference length or area, the actual coefficients are computed.

$$C_{L\text{ACTUAL}} = \frac{A_{\text{COMP}}}{A_{\text{REF}}} \cdot C_{L\text{COMP}} \quad (67a)$$

$$C_{M\text{ACTUAL}} = \frac{A_{\text{COMP}}}{A_{\text{REF}}} \cdot C_{M\text{COMP}}$$

$$C_{D\text{ACTUAL}} = \frac{A_{\text{COMP}}}{A_{\text{REF}}} \cdot C_{D\text{COMP}}$$

COMPARISONS AND TYPICAL RESULTS

The computational method is capable of treating a variety of geometric shapes. Several options are available for modeling and analyzing a particular configuration. If a single sample case were chosen as a demonstrator, many features of the method would not be illustrated. Since transonic experimentation is often impaired by wind tunnel wall interference effects, it would also be bad practice to rely on a single case to evaluate a numerical method. For this reason, eight different sample cases have been selected. These include three isolated body or fuselage shapes, two isolated wings, and three wing-body combinations. These cases cover both sharp and blunt nose bodies as well as conventional and supercritical type wing sections over a range of flow conditions.

The comparisons are of particular interest because the present method is based on certain small-disturbance assumptions. It is important then to study these applications if the method is to be effectively applied to realistic aircraft configurations. The input data set for each of these cases has been included in the appendix of this report. Figure 26 defines the various symbols used for the correlations throughout this section.

Isolated Bodies

A sharp-nose body of revolution was investigated by Swihart and Whitcomb (31). The body had a fineness ratio of 12 and was sting-mounted. This data was selected because it provided isolated body experimental results for non-zero angles-of-attack. Correlations for the zero angle-of-attack case at $M = 0.99$ can be seen in Figure 27. A computation was also made for the 8.4° angle-of-attack case at $M = 0.99$. Correlation with experimental data for the top and the bottom centerlines can be seen in Figure 28. Discrepancies on the upper surface near the body-sting juncture can probably be attributed to boundary layer thickening.

Experimental data for a blunt-nose body of revolution was recently obtained by Couch and Brooks (32). This body had a fineness ratio of approximately 9. The cross-sectional area distribution is typical of supercritical type bodies. The pressure

BODY PRESSURE DISTRIBUTION CORRELATION

+	+	+	+	THEORY	}	ALL ANGULAR STATIONS
○	○	○	○	EXPERIMENT		

SUPERIMPOSED COMPUTED WING PRESSURE DISTRIBUTIONS

————— THEORY (UPPER AND LOWER SURFACE)

WING PRESSURE DISTRIBUTION CORRELATION

×	×	×	×	THEORY – UPPER SURFACE
+	+	+	+	THEORY – LOWER SURFACE
○	○	○	○	EXPERIMENT – UPPER SURFACE
□	□	□	□	EXPERIMENT – LOWER SURFACE

WING SPANWISE LIFT/MOMENT/DRAG DISTRIBUTION CORRELATION

—————	THEORY
□ □ □ □	EXPERIMENT

WING SPANLOAD DISTRIBUTION CORRELATION

×	×	×	×	THEORY
□	□	□	□	EXPERIMENT

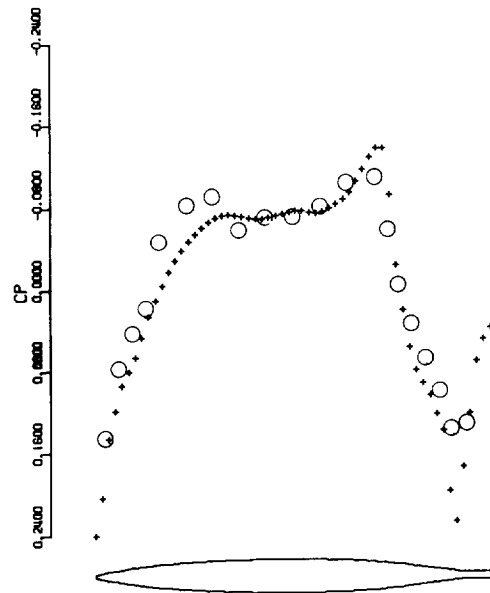
BODY LONGITUDINAL LOAD DISTRIBUTION CORRELATION

×	×	×	×	THEORY
○	○	○	○	EXPERIMENT

WING-BODY AND WING TOTAL FORCE AND MOMENT CORRELATION

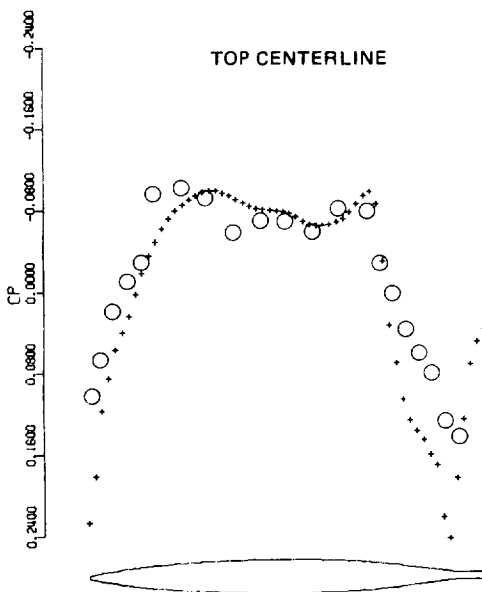
●	THEORY
□ □ □ □	EXPERIMENT

Figure 26. Results Section Symbol Definition

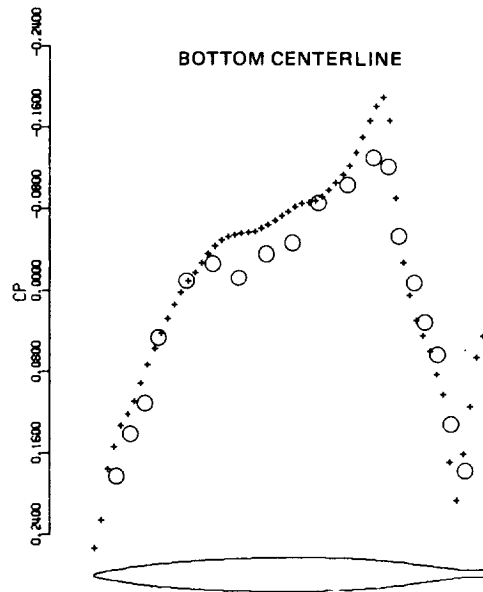


NACA RM L53F07 ISOLATED BODY
 BODY PRESSURE DISTRIBUTION
 BODY STATION 1 BODY ANGLE = 90.00 DEGREES
 MACH = 0.990 ALPHA = 0.00

Figure 27. Sharp Nose Body Pressure Distribution Correlation



NACA RM L53F07 ISOLATED BODY
 BODY PRESSURE DISTRIBUTION
 BODY STATION 1 BODY ANGLE = 90.00 DEGREES
 MACH = 0.990 ALPHA = 8.40



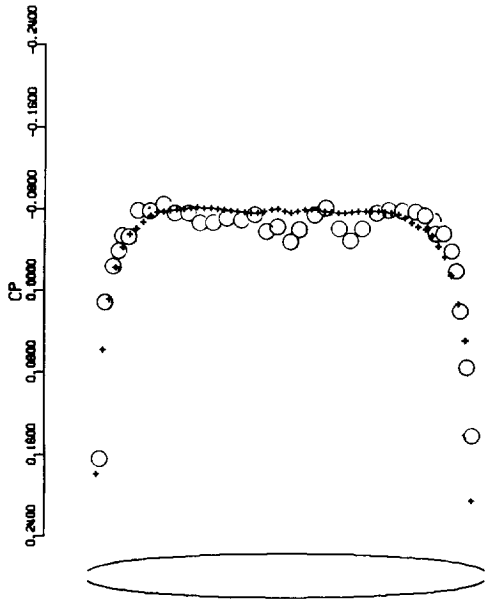
NACA RM L53F07 ISOLATED BODY
 BODY PRESSURE DISTRIBUTION
 BODY STATION 7 BODY ANGLE = -90.00 DEGREES
 MACH = 0.990 ALPHA = 8.40

Figure 28. Sharp Nose Body Pressure Distribution Correlation

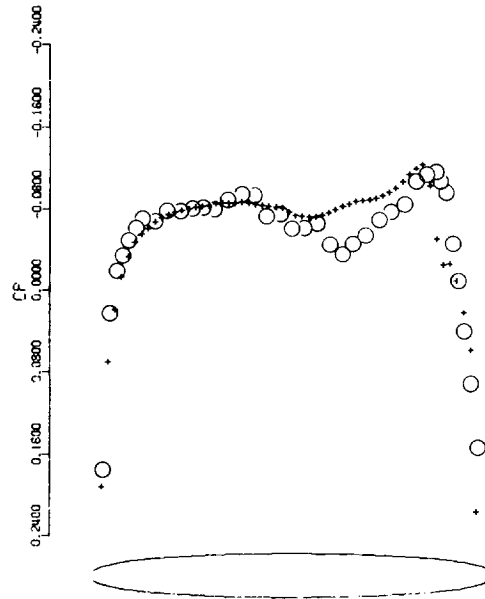
distributions are characterized by a rapid expansion around the nose followed by a flat distribution along the length of the body. Correlations for the case $M = 0.980$ and $M = 0.991$ can be seen in Figure 29.

These simple research models for which comparisons were just presented provide a means of checking the behavior of the present modified small disturbance method when analyzing both blunt and sharp-nose bodies. However, these shapes are rarely of interest to the aircraft designer. To demonstrate the full computational capability of the present method, calculations have been made for a realistic transport fuselage. The geometry for this case can be seen in Figures 18 and 19. In this particular application, the fine mesh is positioned for detailed analysis of the nose-windshield-canopy region of the fuselage.

Wind tunnel pressure distributions were measured to provide an understanding of shock-wave/boundary layer interactions over the canopy which caused unacceptable levels of noise in the cockpit. The sting-mounted isolated fuselage model was instrumented to obtain detailed pressure data in the windshield-canopy region (33). The objective of follow-up experiments or the use of the analysis method would be to re-contour the fuselage shape to reduce the strength of the canopy shock wave. Correlations with experimental data for the fuselage top centerline at the transonic cruise condition can be seen in Figure 30. The computed decay of the canopy shock wave can be seen in Figure 31.

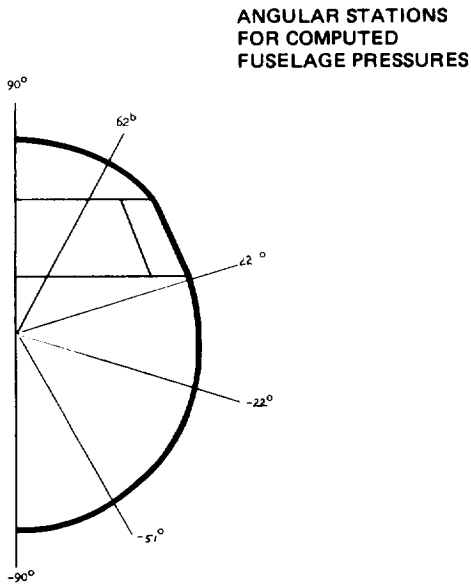


NACA TND 7331 ISOLATED BODY
 BODY PRESSURE DISTRIBUTION
 BODY STATION 1 BODY ANGLE = 90.00 DEGREES
 MACH = 0.980 ALPHA = 0.00

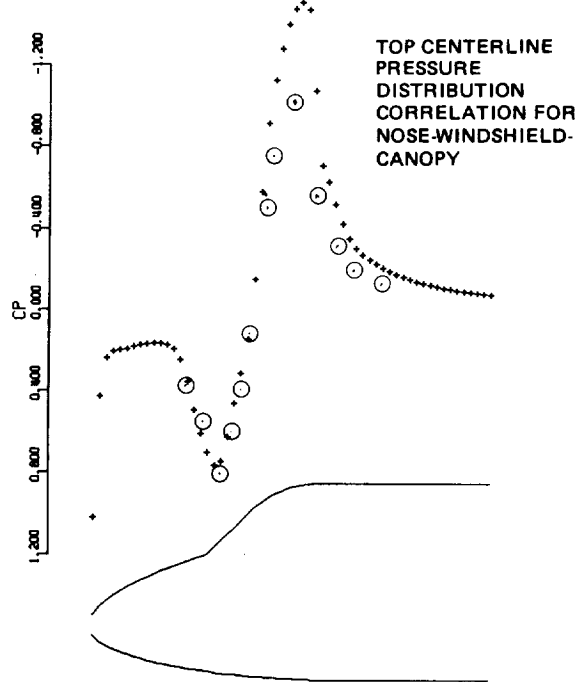


NACA TND 7331 ISOLATED BODY
 BODY PRESSURE DISTRIBUTION
 BODY STATION 1 BODY ANGLE = 90.00 DEGREES
 MACH = 0.991 ALPHA = 0.00

Figure 29. Blunt Nose Body Pressure Distribution Correlation



ANGULAR STATIONS
 FOR COMPUTED
 FUSELAGE PRESSURES



TOP CENTERLINE
 PRESSURE
 DISTRIBUTION
 CORRELATION FOR
 NOSE-WINDSHIELD-
 CANOPY

GULFSTREAM II ISOLATED FUSELAGE NOSE
 BODY PRESSURE DISTRIBUTION
 BODY STATION 1 BODY ANGLE = 90.00 DEGREES
 MACH = 0.800 ALPHA = 3.10

Figure 30. Grumman Gulfstream II Fuselage Pressure Distribution Correlation

Isolated Wings

Two different wings have been selected for comparisons. The first is a low aspect ratio wing with a symmetric wing section and the second is a high aspect ratio wing with a conventionally cambered NACA 64₁-212 wing section. Viscous effects on the symmetric wing are negligible and no viscous effects were computed (VISM0D = 1). Viscous effects did not have a large impact on computed pressures for the cambered wing but they did significantly change the computed forces and moments. The cambered wing was analyzed using the viscous/inviscid solution process (VISM0D = 3).

The ONERA M6 wing ⁽³⁴⁾ provides a very simple case for the computational method because wing planform sweep and taper are mild. In addition, viscous effects are negligible making this a very popular case for published correlation studies. The ONERA wing is interesting, however, because the data exhibits a double shock wave pattern. Superimposed computed pressure distributions for the wing upper and lower surface can be seen in Figure 32. A weak highly swept supersonic to supersonic shock wave forms at the wing leading edge. As the wing tip is approached, this weak shock wave coalesces with the primary supersonic to subsonic shock wave behind it. Published reports indicate that methods with poor resolution or flow governing equations without additional cross-flow terms cannot resolve the weak highly swept type of shock wave. Correlations with experimental data at five span stations can be seen in Figure 33. Spanwise distributions of lift, drag and pitching moment can be seen in Figure 34. Figure 35 shows the computed spanload and drag component breakdown.

A cambered high aspect ratio wing ⁽³⁵⁾ was analyzed using the present method. This case is thought to be of particular interest because the geometry and lift condition are typical of conventional transport wings now in existence (super-critical type wings are also included - case number 8). Figure 36 illustrates the wing shock wave pattern. Correlations at five spanwise wing stations can be seen in Figure 37. The computed spanload along with span efficiency factor and drag component breakdown can be seen in Figure 38. Force and moment comparisons can be seen in Figure 39.

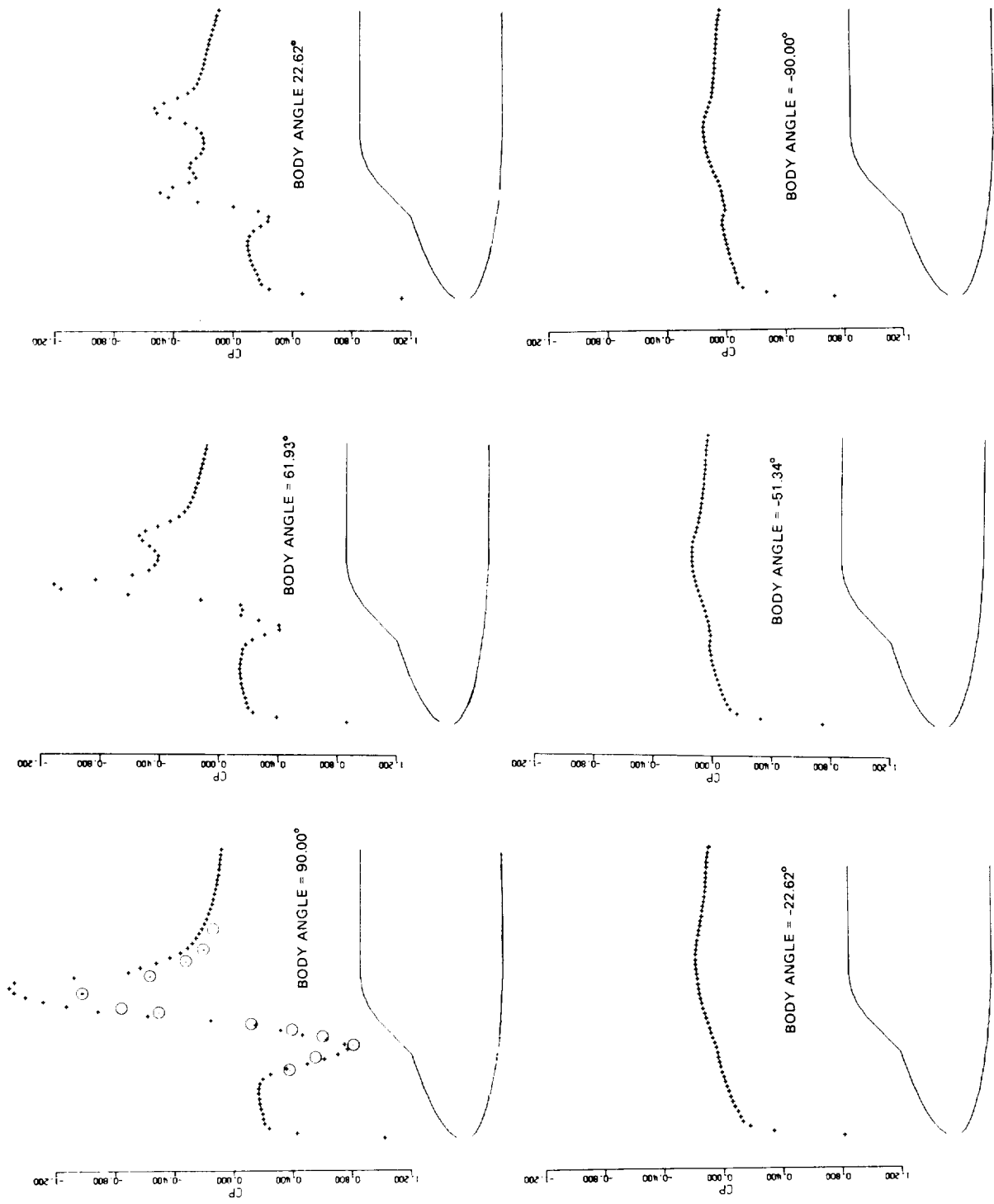


Figure 31. Grumman Gulfstream II Fuselage-Decay of Canopy Shockwave, $M = 0.800$, $\alpha = 3.10^\circ$

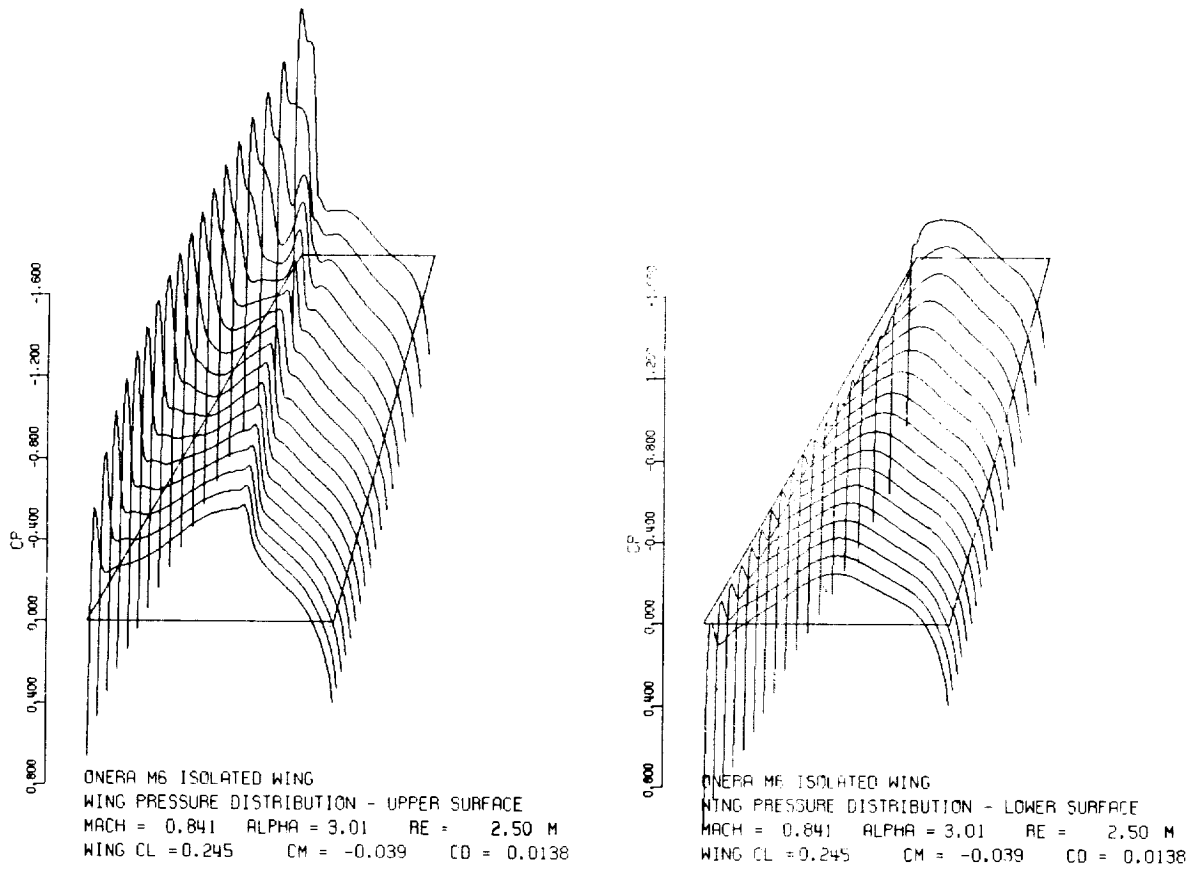


Figure 32. Superimposed Computed Pressure Distributions for Isolated Onera M6 Wing

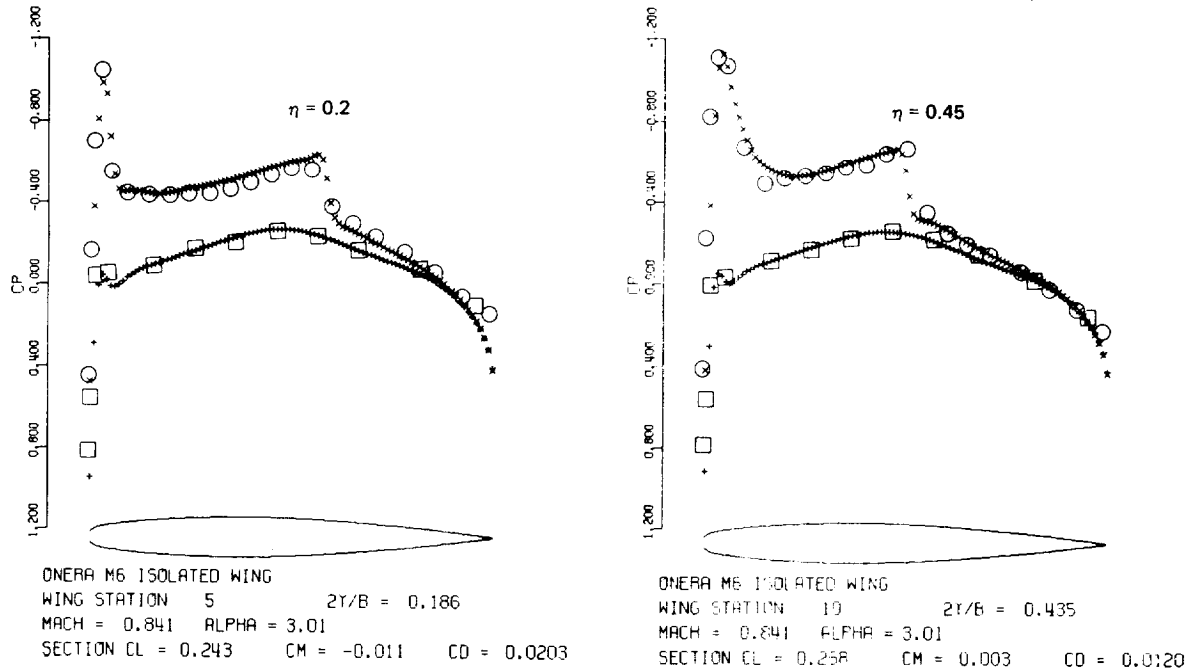
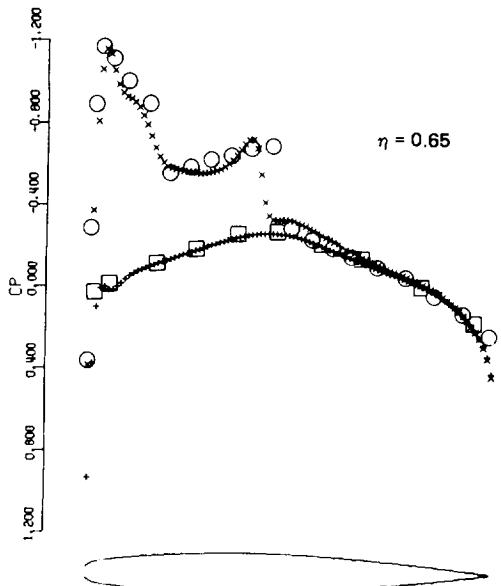
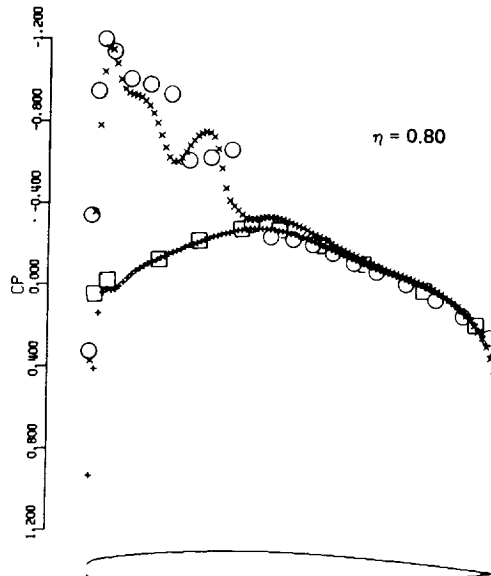


Figure 33. Onera M6 Wing Pressure Distribution Correlation (Sheet 1 of 2)



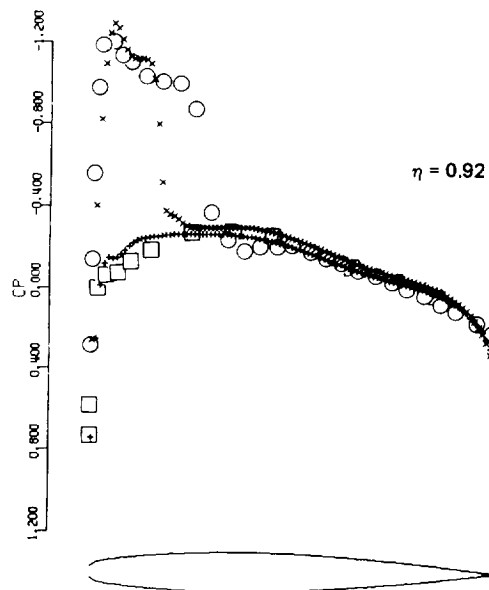
$\eta = 0.65$

ONERA M6 ISOLATED WING
 WING STATION 14 $2\gamma/B = 0.665$
 MACH = 0.841 ALPHA = 3.01
 SECTION CL = 0.270 CM = 0.014 CD = 0.0090



$\eta = 0.80$

ONERA M6 ISOLATED WING
 WING STATION 16 $2\gamma/B = 0.799$
 MACH = 0.841 ALPHA = 3.01
 SECTION CL = 0.250 CM = 0.021 CD = 0.0064



$\eta = 0.92$

ONERA M6 ISOLATED WING
 WING STATION 18 $2\gamma/B = 0.956$
 MACH = 0.841 ALPHA = 3.01
 SECTION CL = 0.179 CM = 0.019 CD = -0.0072

Figure 33. Onera M6 Wing Pressure Distribution Correlation (Sheet 2 of 2)

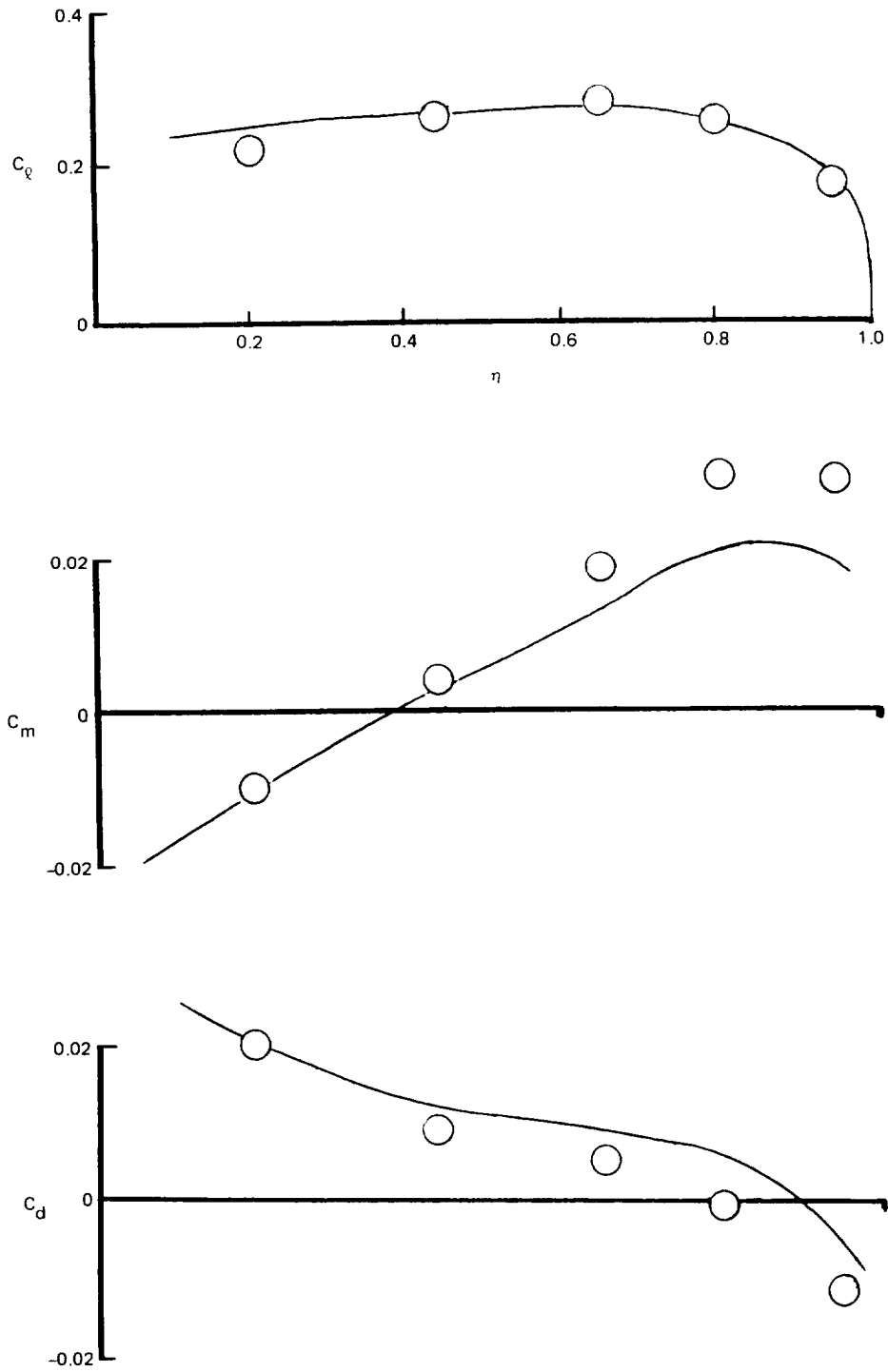
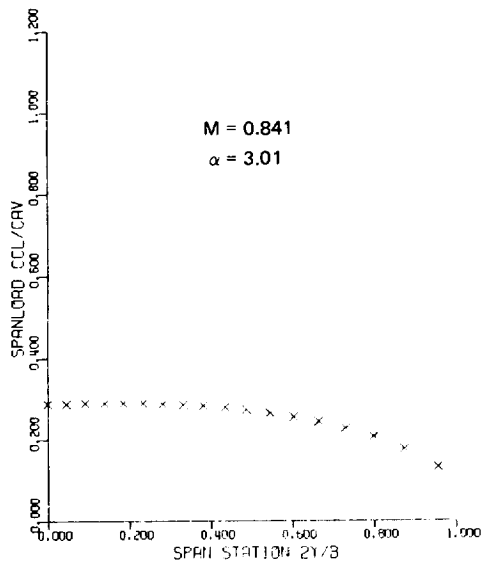


Figure 34. Onera M6 Wing Section Force and Moment Coefficient Correlation, $M = 0.8407, \alpha = 3.01^\circ$



ONERA M6 ISOLATED WING
 SPAN EFFICIENCY $\epsilon = 0.971$
 LIFT INDUCED DRAG = 0.0051
 WAVE DRAG = 0.0087
 FRICTION DRAG = 0.0000

Figure 35. Onera M6 Wing Computed Spanload

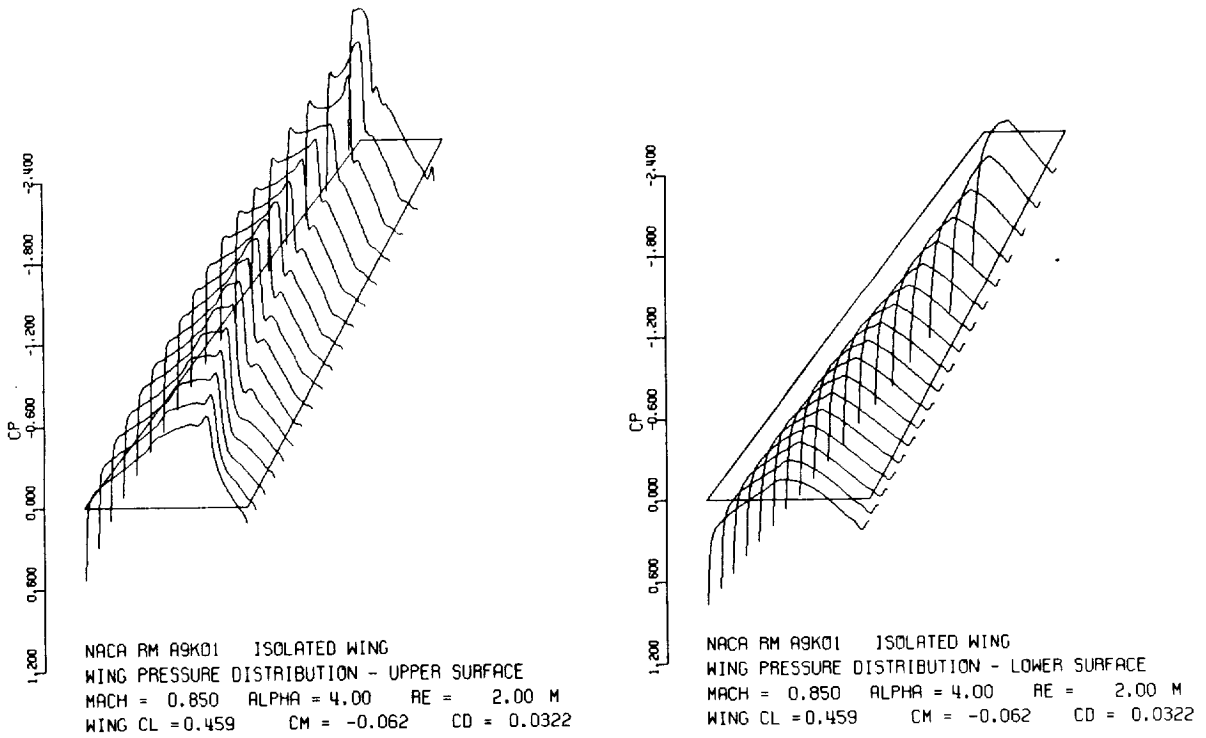
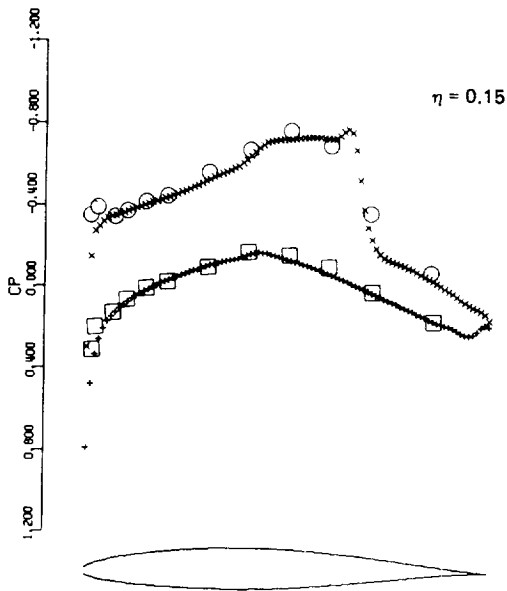
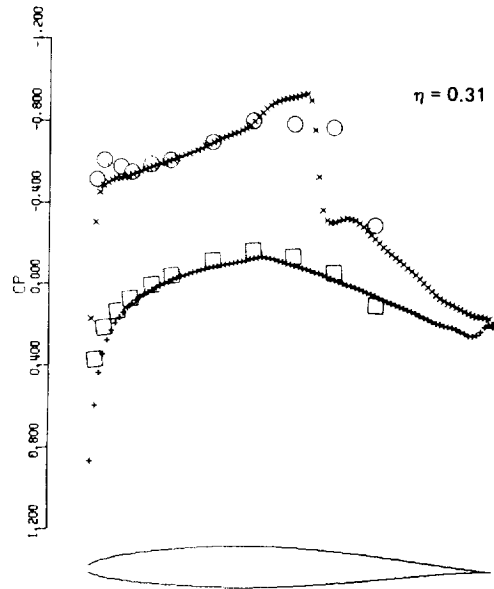


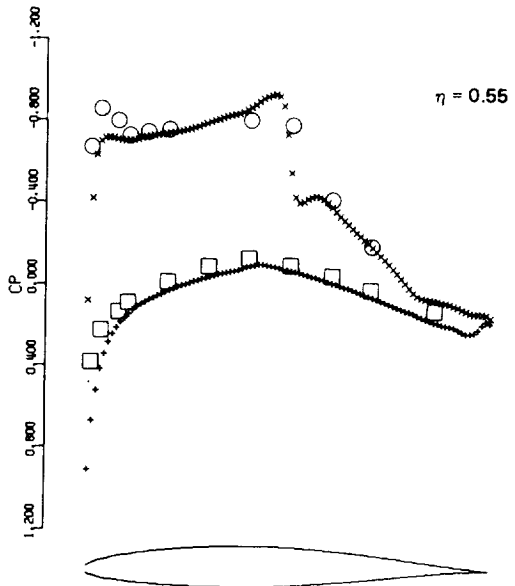
Figure 36. NACA RM A9K01 Isolated Wing Superimposed Computed Pressure Distributions



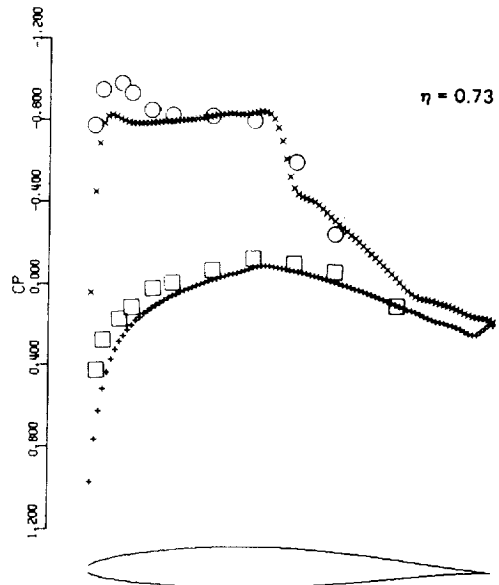
NACA RM A9K01 ISOLATED WING
 WING STATION 4 $2Y/B = 0.139$
 MACH = 0.850 ALPHA = 4.00
 SECTION CL = 0.414 CM = -0.075 CD = 0.0382



NACA RM A9K01 ISOLATED WING
 WING STATION 8 $2Y/B = 0.332$
 MACH = 0.850 ALPHA = 4.00
 SECTION CL = 0.475 CM = -0.057 CD = 0.0283



NACA RM A9K01 ISOLATED WING
 WING STATION 12 $2Y/B = 0.544$
 MACH = 0.850 ALPHA = 4.00
 SECTION CL = 0.517 CM = -0.041 CD = 0.0201



NACA RM A9K01 ISOLATED WING
 WING STATION 15 $2Y/B = 0.730$
 MACH = 0.850 ALPHA = 4.00
 SECTION CL = 0.526 CM = -0.026 CD = 0.0169

Figure 37. NACA RM A9K01 Wing Pressure Distribution Correlation (Sheet 1 of 2)

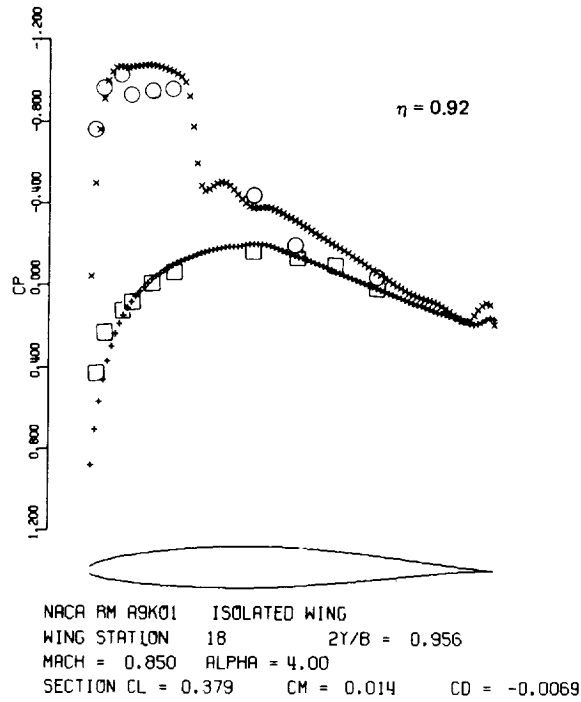


Figure 37. NACA RM A9K01 Wing Pressure Distribution Correlation (Sheet 2 of 2)

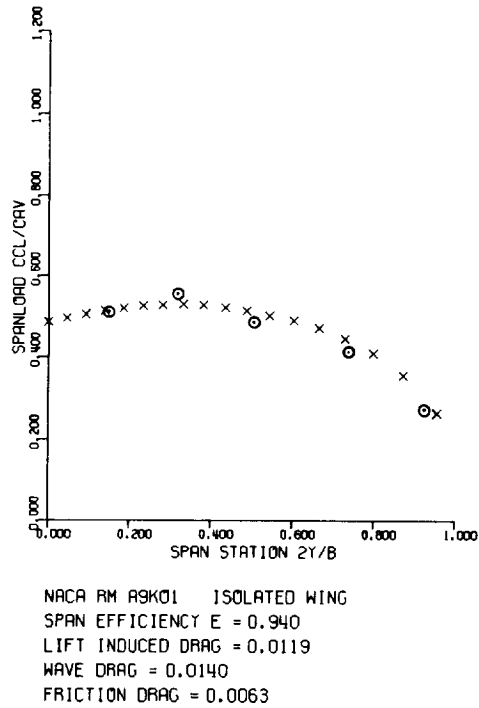


Figure 38 NACA RM A9K01 Isolated Wing Spanload Correlation

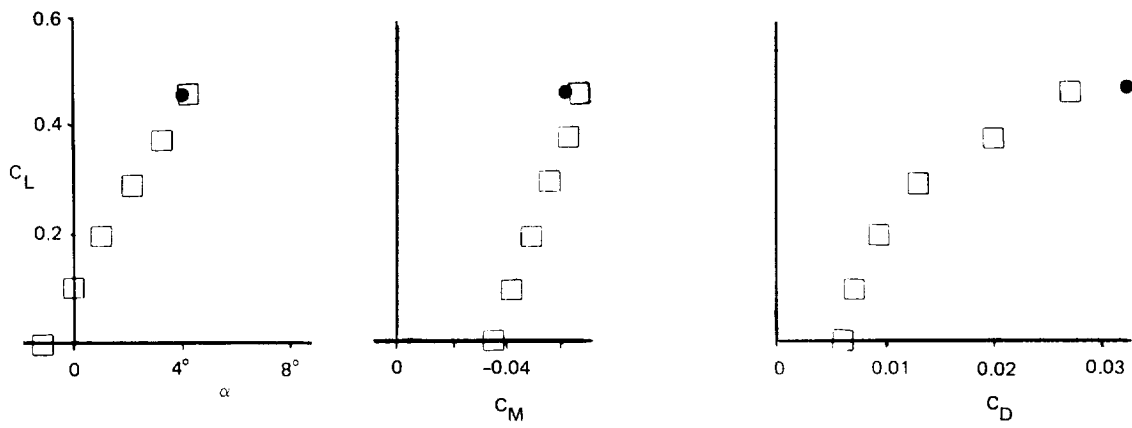


Figure 39. NACA RM A9K01 Isolated Wing Force and Moment Coefficient Correlation, $M = 0.85, \alpha = 4^\circ$

Wing Body Configurations

Three different wing-body configurations have been selected for correlation studies. They are 1) a simple wing-body research model with a planar wing, 2) a conventional wing transport aircraft, and 3) a supercritical wing area-ruled fuselage transport configuration with wing control surface deflection effects. The final configuration with its highly aft-cambered wing section illustrates both the use of the viscous/inviscid interaction mode of operation and the arbitrary body modeling scheme.

A simple wing-body research model ⁽³⁶⁾ is illustrated in Figure 40. The center mounted wing has 45° of sweep with a NACA 65A006 wing section. Superimposed computed pressure distributions for the wing can be seen in Figure 41. Correlations with experimental wing pressures at five spanwise stations can be seen in Figure 42. Body pressure correlations can be found in Figures 43 and 44. Boundary layer displacement thickness effects were not computed for the symmetric wing in this case. Force and moment comparisons are made in Figures 45 through 49. The configuration drag source breakdown can be seen in Figure 48.

The Boeing KC-135 transport ⁽³⁷⁾ has been illustrated in Figure 50. This is a good example of a conventionally winged transport. Comparisons have been made for the configuration without engine pods or pylons. An initial computation indicated that this wind-tunnel model may be experiencing a wing twist caused by wing loading. As a result, the geometry analysed includes 1° of negative section incidence at the wing tip blending to 0° at the wing-body juncture. Superimposed computed wing pressures can be seen in Figure 51 for the cruise design point. Correlations at three wing span stations can be seen in Figure 52.

The final case is a supercritical wing/area ruled fuselage transport configuration ⁽³⁸⁾ (See Figure 53). The solution diverged if the actual glove leading edge sweep of 72° was modeled. For this reason, a reduced sweep of 57° was employed for these comparisons. It is expected that the wing root leading edge pressure peak discrepancy (Figures 55 and 56) is a result of this approximation. In addition, the wing-body computed moment coefficient will have an erroneous nose down component (Figures 58 and 59). The fuselage model for this calculation was shown in Figure 20. This model is interesting because it illustrates the aerodynamic effects that a wing control

surface deflection has on a supercritical wing when the flow is transonic and shock waves are present. For these comparisons, data at a -15° deflection of the second control surface was used. The control surface can be seen in Figure 53 and on the wing section pressure distribution plots. Superimposed computed pressure distributions at the cruise design point can be seen in Figure 54 for the basic wing shape. Wing pressure distribution correlations at five spanwise stations can be seen in Figure 55. A similar set of comparisons for the wing with the control surface deflected upward can be seen in Figures 56 and 57. Force and moment comparisons are made in Figures 58 and 59 while the spanload and drag source breakdown can be seen in Figure 60.

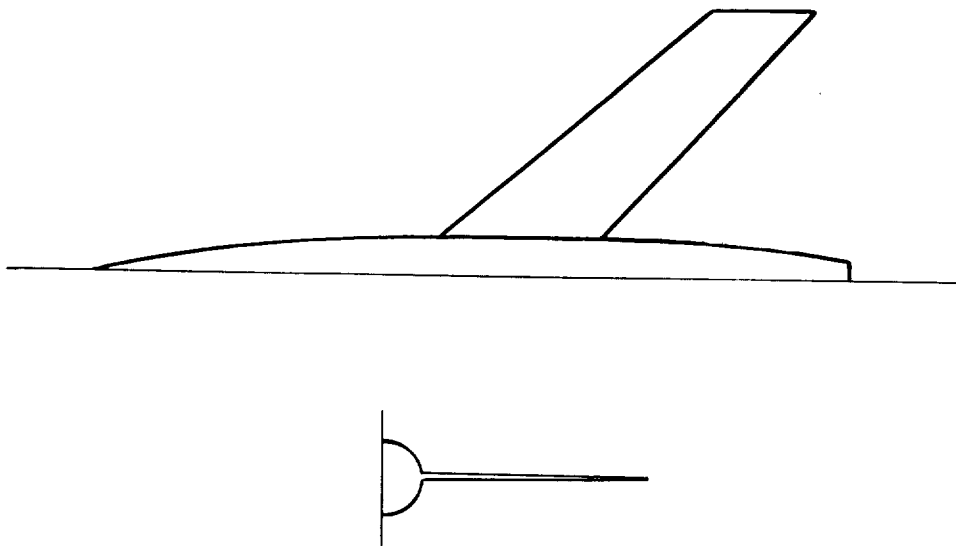


Figure 40. NACA RM L51F07 Simple Wing-Body Configuration

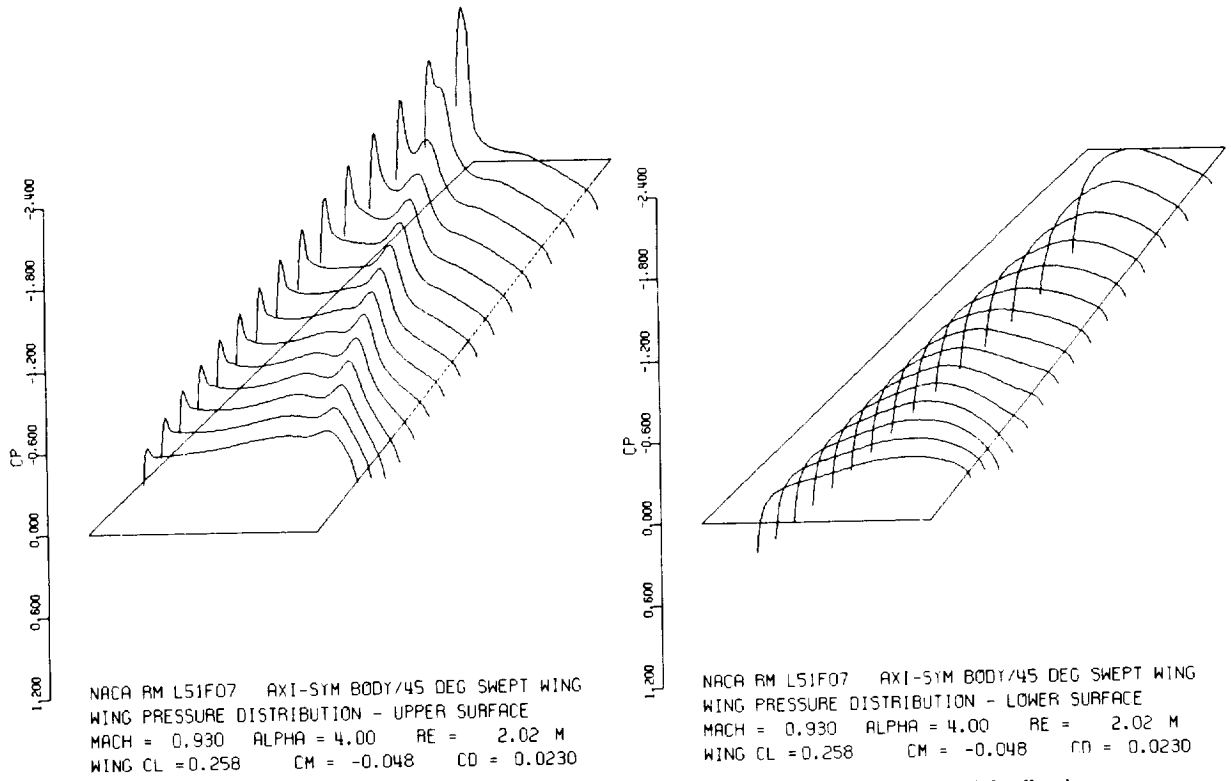


Figure 41. NACA RM L51F07 Wing-Body Superimposed Computed Wing Pressure Distributions

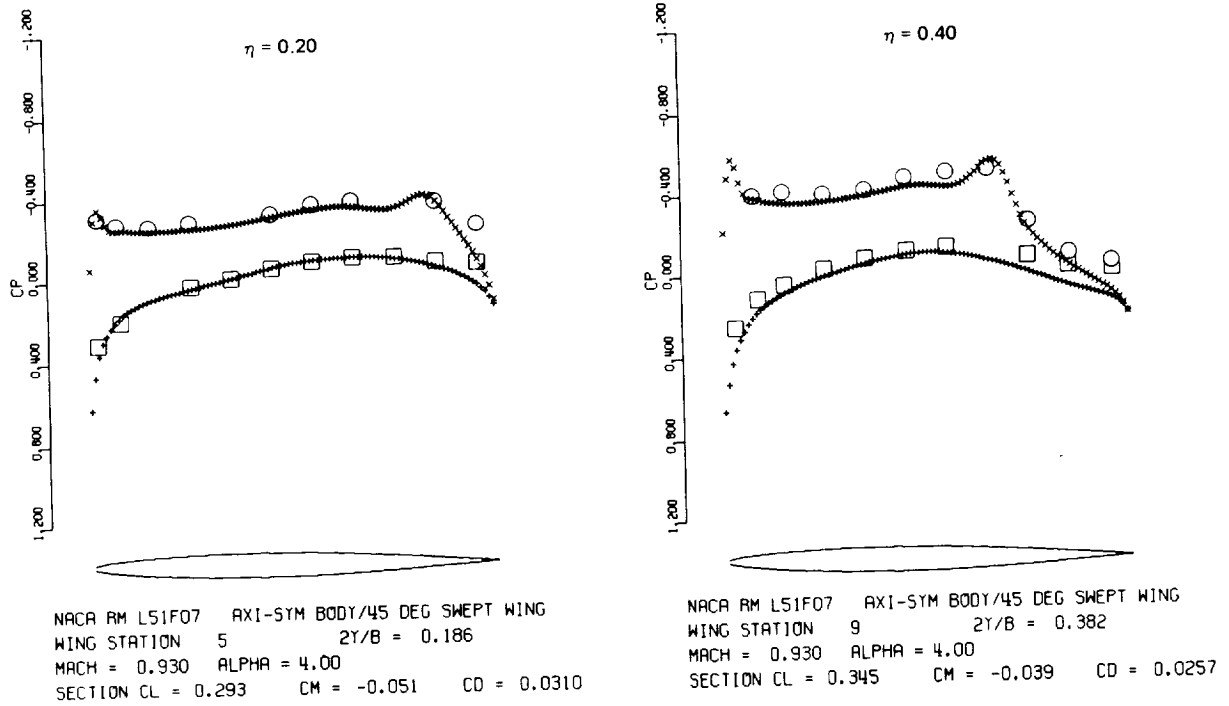
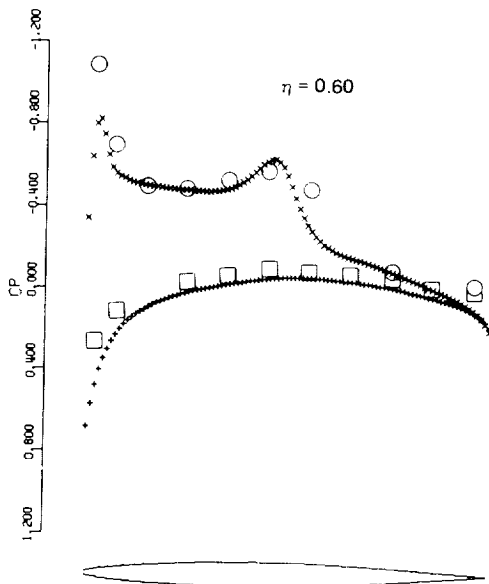
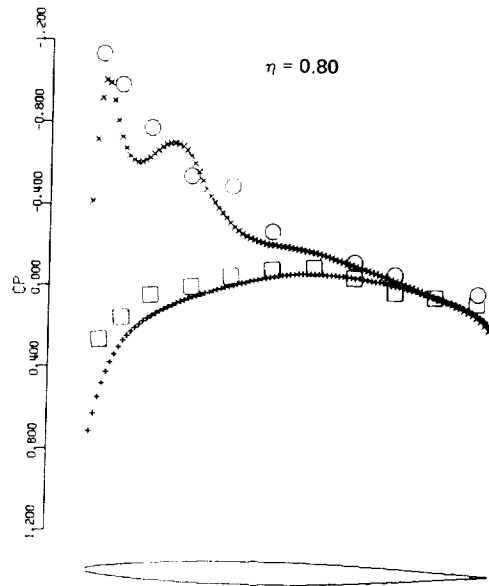


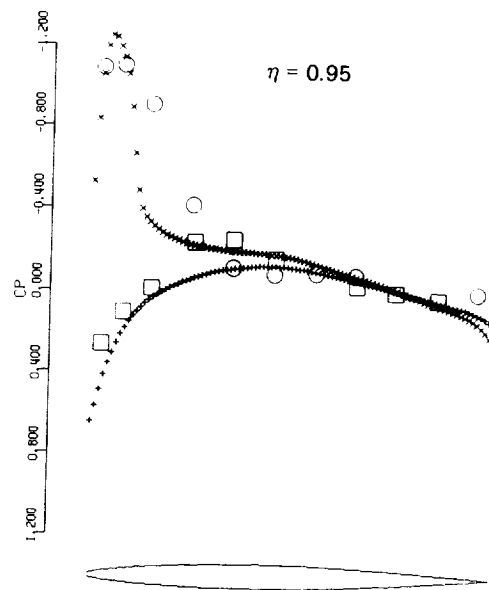
Figure 42. NACA RM L51F07 Wing Pressure Distribution Correlation (Sheet 1 of 2)



NACA RM L51F07 AXI-SYM BODY/45 DEG SWEEP WING
 WING STATION 13 $2l/B = 0.603$
 MACH = 0.930 ALPHA = 4.00
 SECTION CL = 0.364 CM = -0.009 CD = 0.0199



NACA RM L51F07 AXI-SYM BODY/45 DEG SWEEP WING
 WING STATION 16 $2l/B = 0.799$
 MACH = 0.930 ALPHA = 4.00
 SECTION CL = 0.334 CM = 0.021 CD = 0.0146



NACA RM L51F07 AXI-SYM BODY/45 DEG SWEEP WING
 WING STATION 18 $2l/B = 0.956$
 MACH = 0.930 ALPHA = 4.00
 SECTION CL = 0.211 CM = 0.033 CD = 0.0027

Figure 42. NACA RM L51F07 Wing Pressure Distribution Correlation (Sheet 2 of 2)

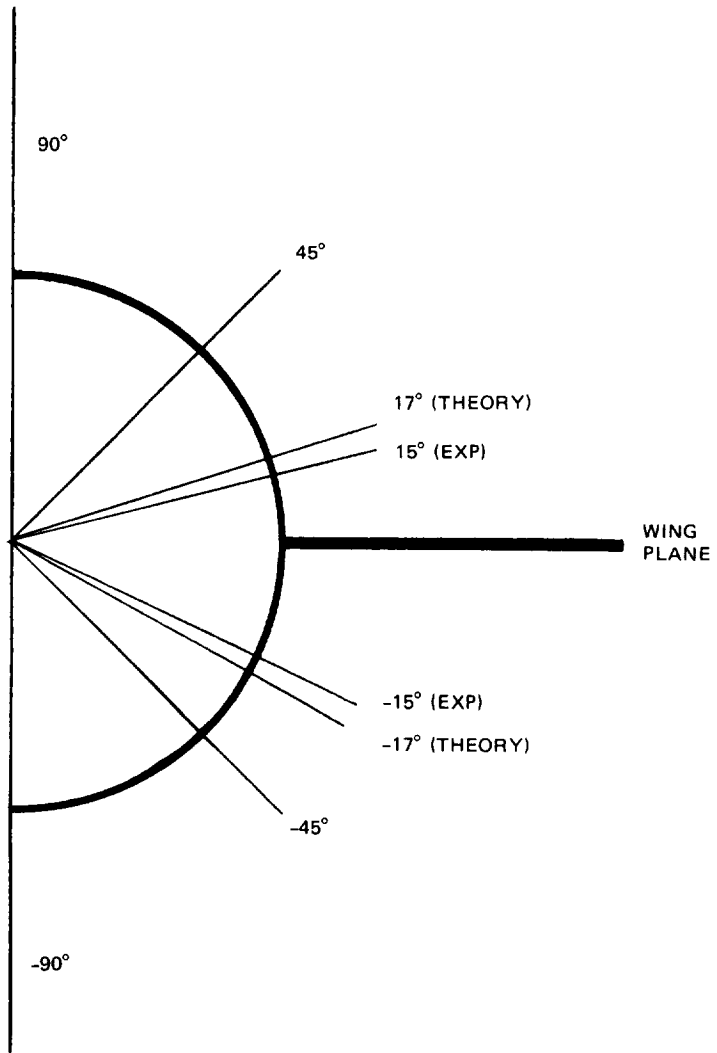
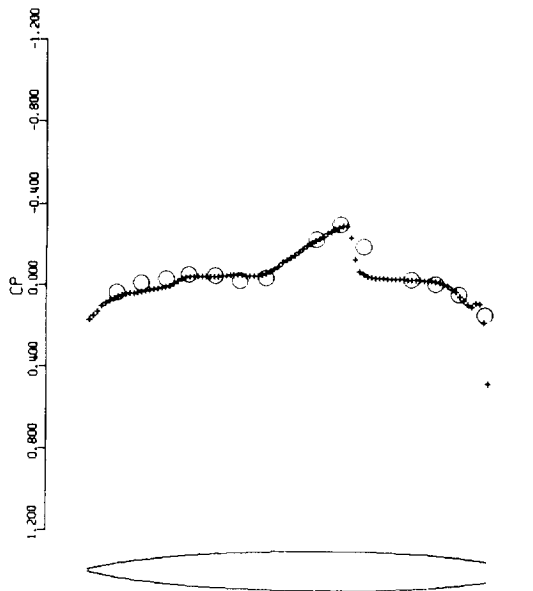
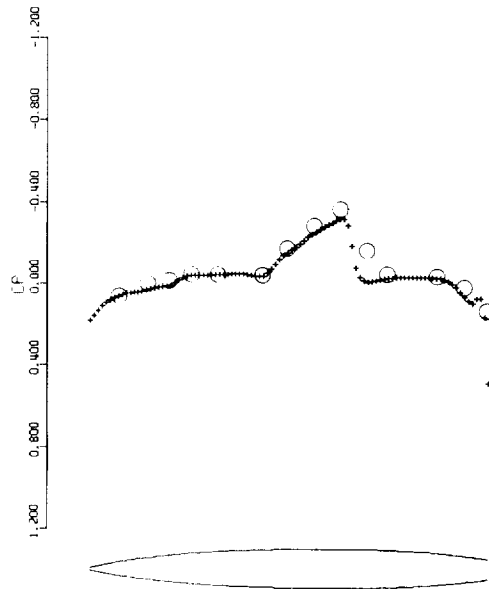


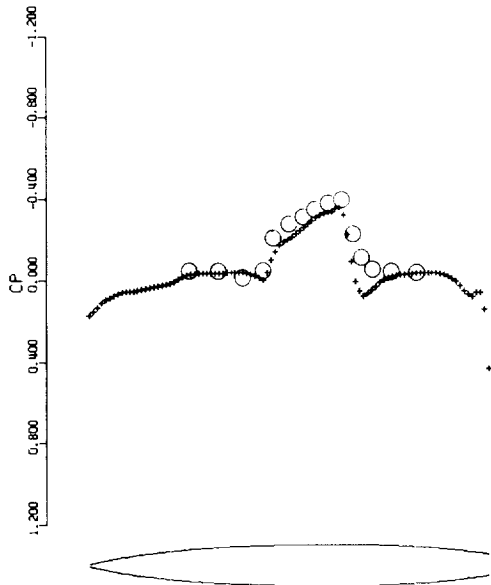
Figure 43. NACA RM L51F07 Stations for Computed and Experimental Body Pressures



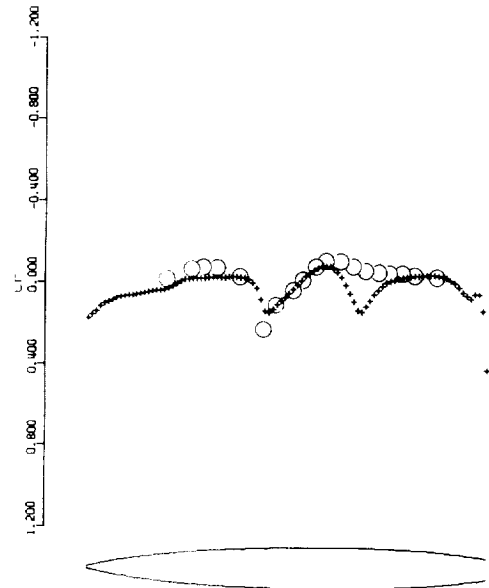
NACA RM L51F07 AXI-SYM BODY/45 DEG SWEPT WING
 BODY PRESSURE DISTRIBUTION
 BODY STATION 1 BODY ANGLE = 90.00 DEGREES
 MACH = 0.930 ALPHA = 4.00



NACA RM L51F07 AXI-SYM BODY/45 DEG SWEPT WING
 BODY PRESSURE DISTRIBUTION
 BODY STATION 6 BODY ANGLE = 45.00 DEGREES
 MACH = 0.930 ALPHA = 4.00

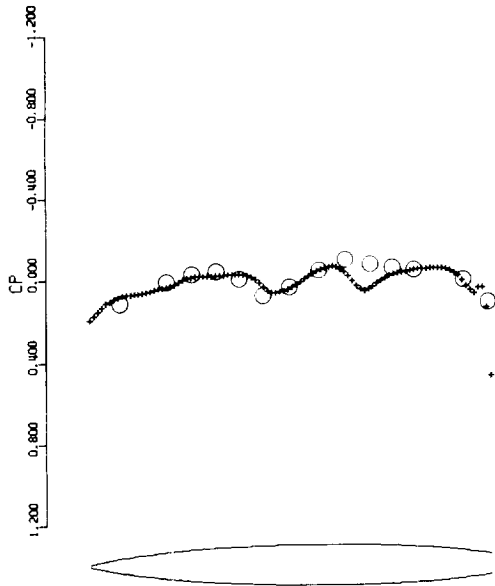


NACA RM L51F07 AXI-SYM BODY/45 DEG SWEPT WING
 BODY PRESSURE DISTRIBUTION
 BODY STATION 9 BODY ANGLE = 17.35 DEGREES
 MACH = 0.930 ALPHA = 4.00

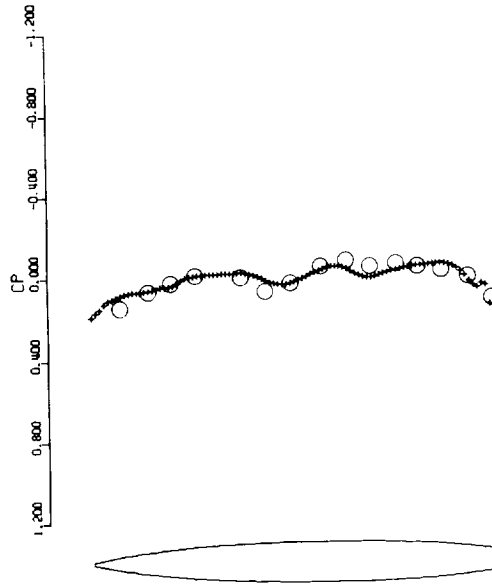


NACA RM L51F07 AXI-SYM BODY/45 DEG SWEPT WING
 BODY PRESSURE DISTRIBUTION
 BODY STATION 20 BODY ANGLE = -17.35 DEGREES
 MACH = 0.930 ALPHA = 4.00

Figure 44. NACA RM L51F07 Body Pressure Distribution Correlation (Sheet 1 of 2)

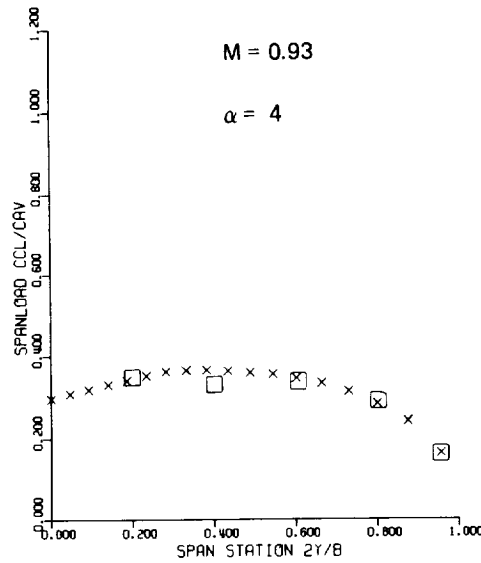


NACA RM L51F07 AXI-SYM BODY/45 DEG SWEPT WING
 BODY PRESSURE DISTRIBUTION
 BODY STATION 17 BODY ANGLE = -45.00 DEGREES
 MACH = 0.930 ALPHA = 4.00



NACA RM L51F07 AXI-SYM BODY/45 DEG SWEPT WING
 BODY PRESSURE DISTRIBUTION
 BODY STATION 12 BODY ANGLE = -90.00 DEGREES
 MACH = 0.930 ALPHA = 4.00

Figure 44. NACA RM L51F07 Body Pressure Distribution Correlation (Sheet 2 of 2)



NACA RM L51F07 AXI-SYM BODY/45 DEG SWEPT WING
 SPAN EFFICIENCY $E = 0.927$
 LIFT INDUCED DRAG = 0.0072
 WAVE DRAG = 0.0094
 FRICTION DRAG = 0.0135

Figure 45. NACA RM L51F07 Wing-Body Spanload Correlation

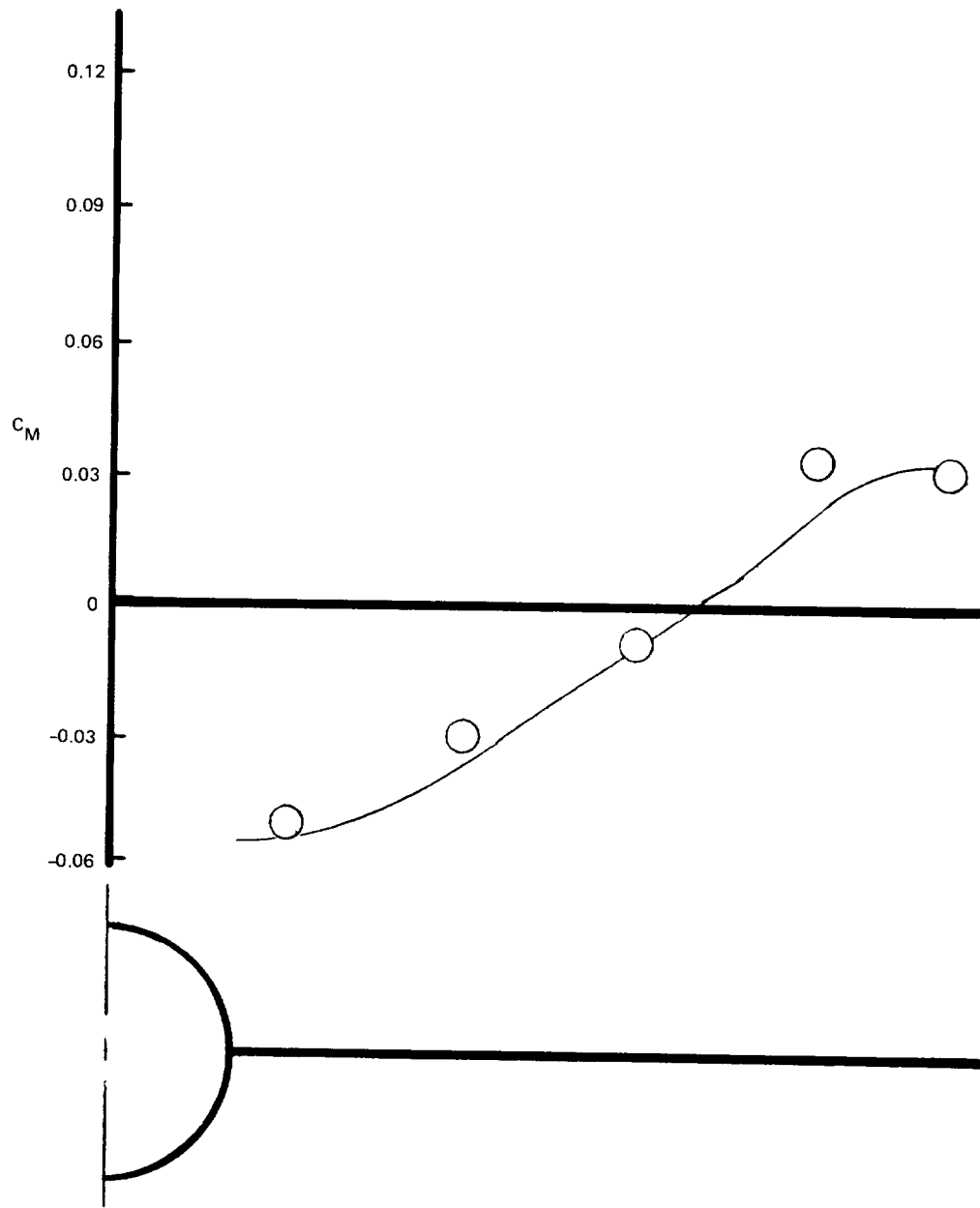


Figure 46. Wing-Body Spanwise Pitching Moment Coefficient Correlation, NACA RM L51F07, $M = 0.93$, $\alpha = 4^\circ$

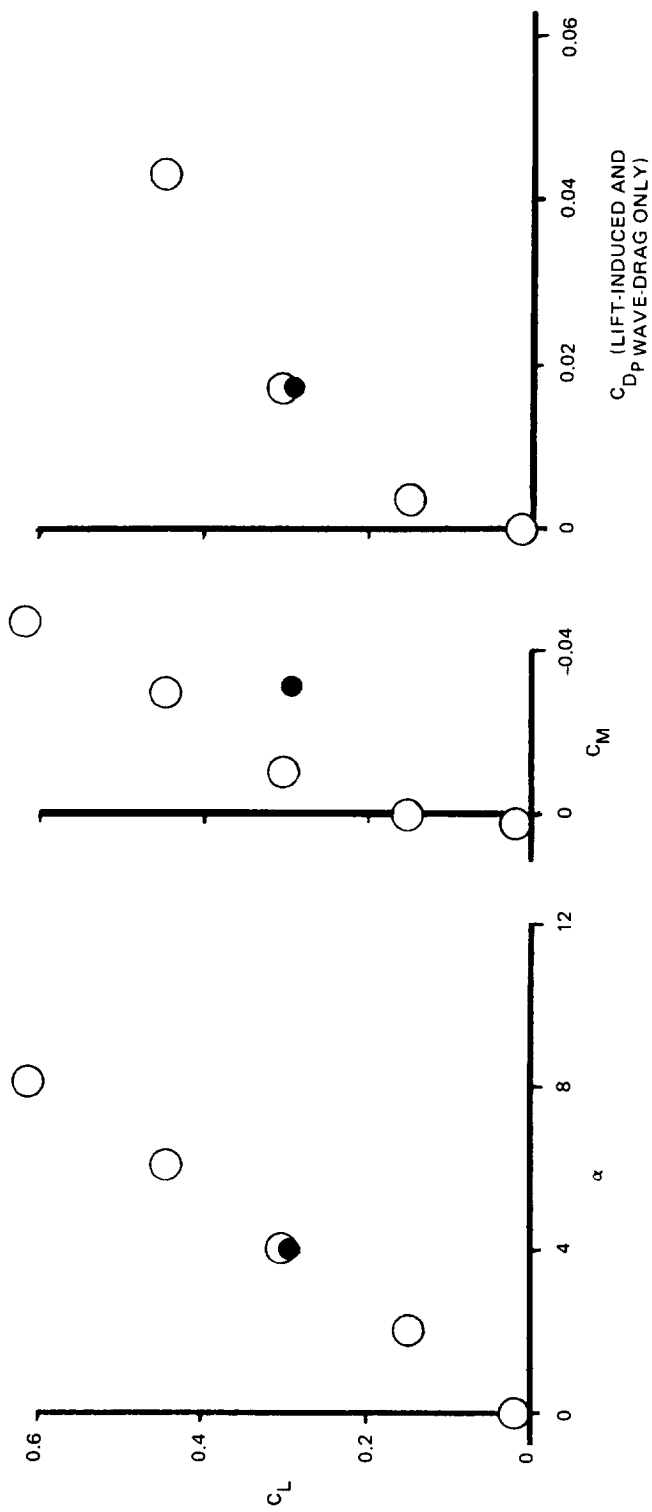


Figure 47. Wing-Body Force and Moment Coefficient Correlation NACA RM L51F07, $M = 0.93, \alpha = 4^\circ$

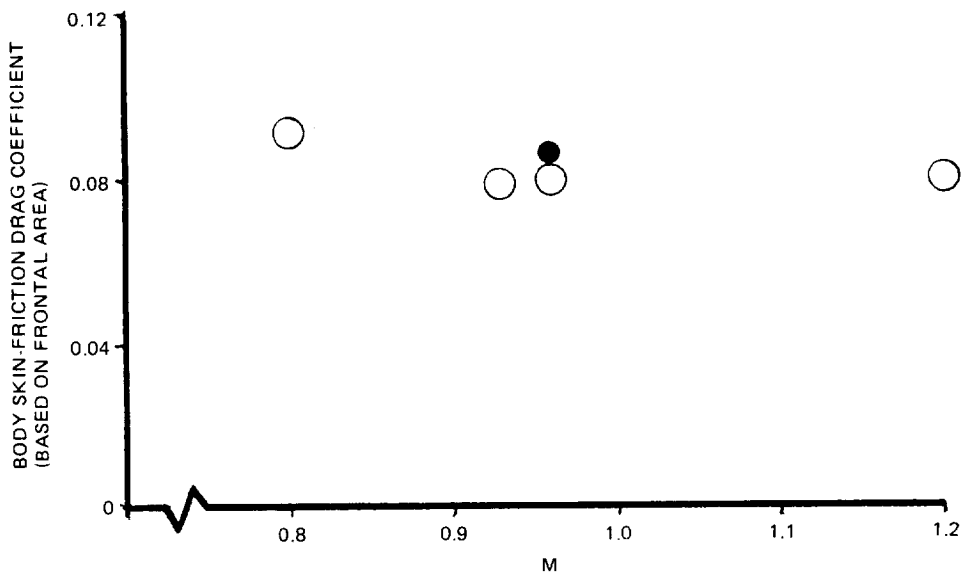
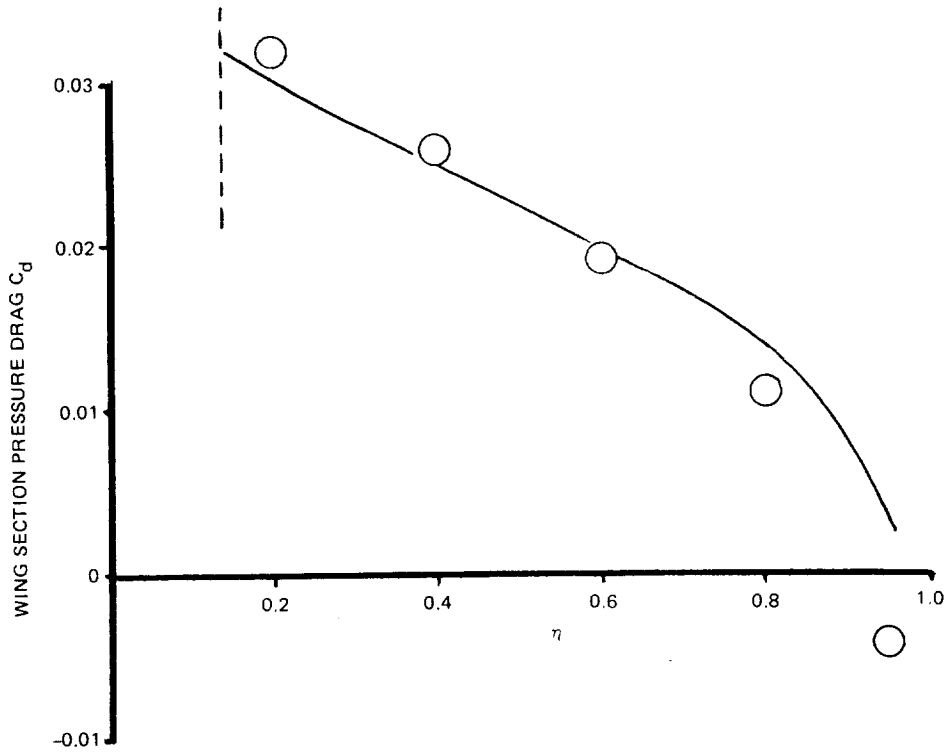


Figure 48. NACA RM L51F07 Wing and Body Drag Coefficient Correlation

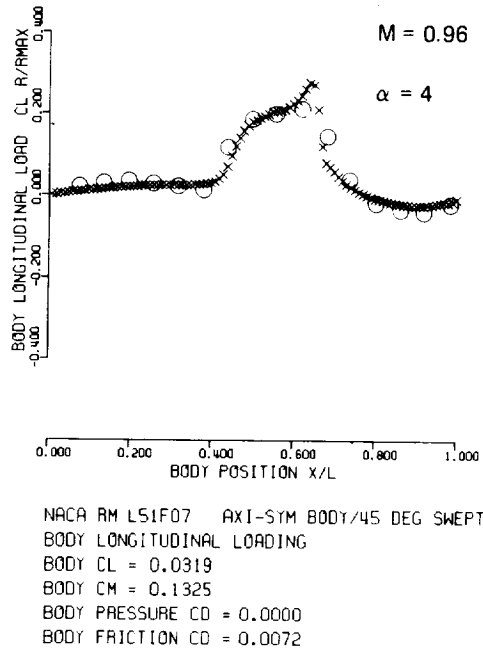


Figure 49. NACA RM L51F07 Body Longitudinal Load Correlation

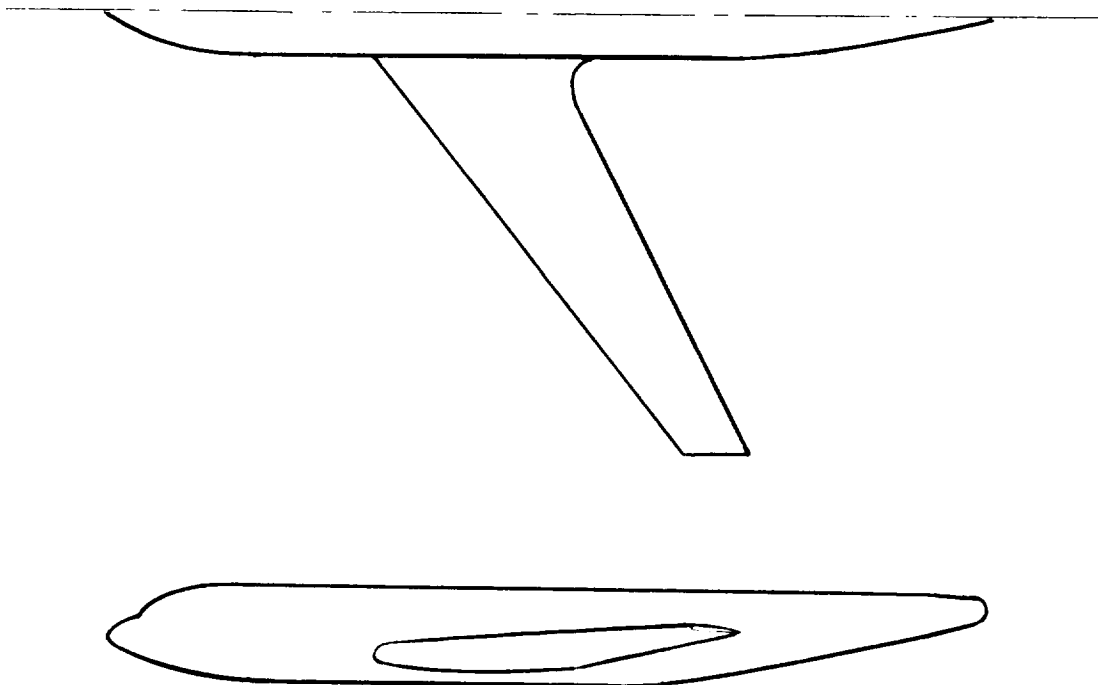


Figure 50. Boeing KC-135 Transport Configuration (Pylons and Engines Off)

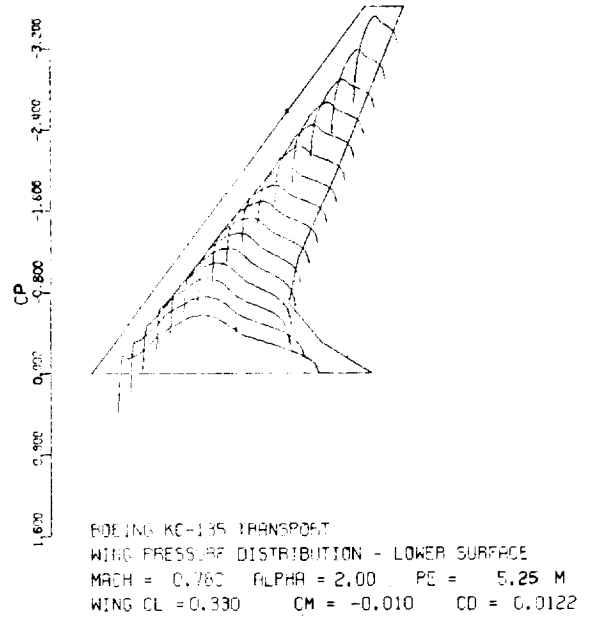
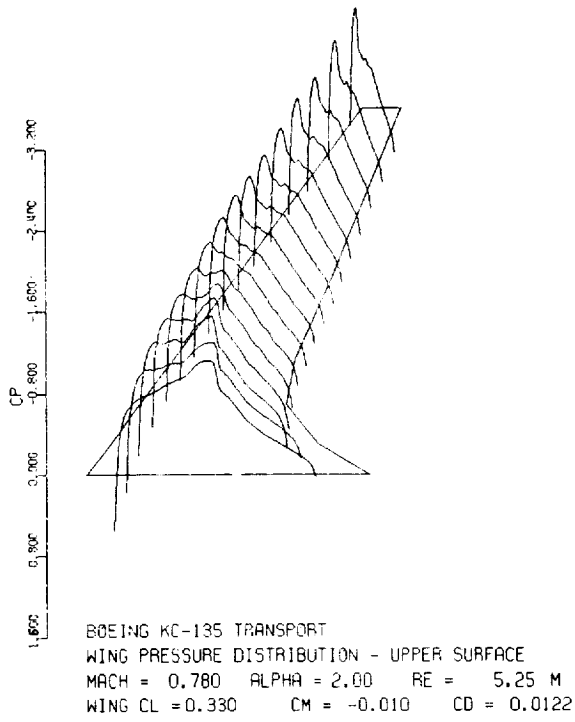
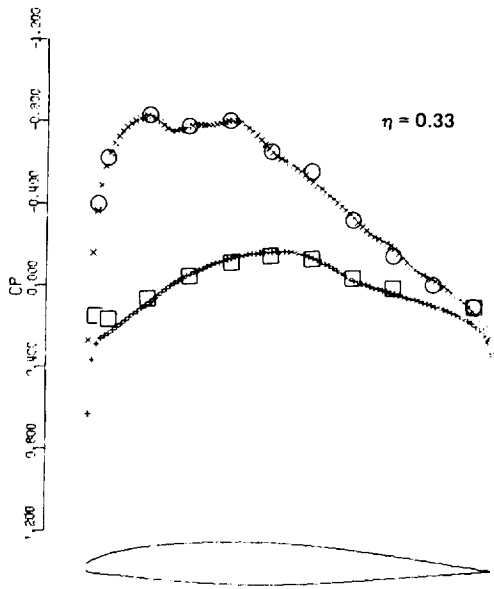
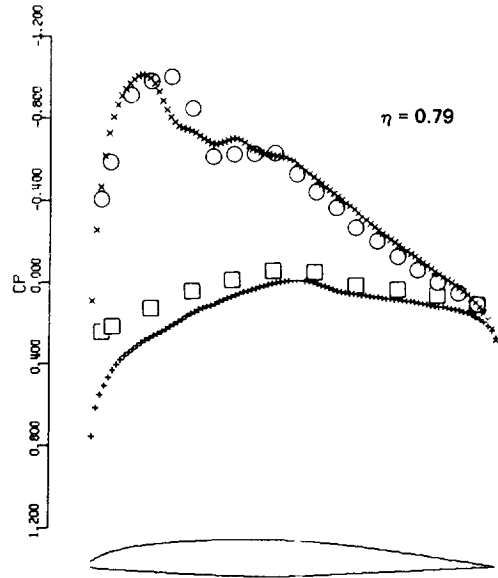


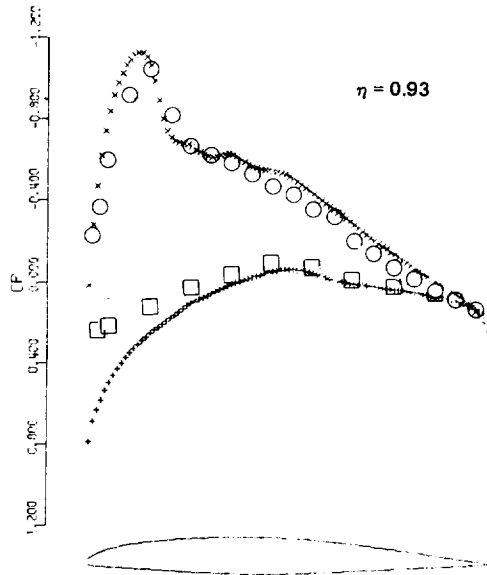
Figure 51. Boeing KC-135 Transport, Superimposed Computed Wing Pressure Distributions



BOEING KC-135 TRANSPORT
 WING STATION 8 $2Y/B = 1.832$
 MACH = 0.760 ALPHA = 2.00
 SECTION CL = 0.462 CM = -0.030 CD = 0.0157



BOEING KC-135 TRANSPORT
 WING STATION 16 $2Y/B = 0.799$
 MACH = 0.780 ALPHA = 2.00
 SECTION CL = 0.601 CM = -0.044 CD = 0.0132



BOEING KC-135 TRANSPORT
 WING STATION 18 $2Y/B = 0.956$
 MACH = 0.780 ALPHA = 2.00
 SECTION CL = 0.534 CM = -0.014 CD = 0.0040

Figure 52. Boeing KC-135 Transport Wing Pressure Distribution Correlation

NOTE: 57° GLOVE LEADING EDGE
SWEEP USED FOR ANALYSIS
(ACTUAL GLOVE SWEEP 72°)

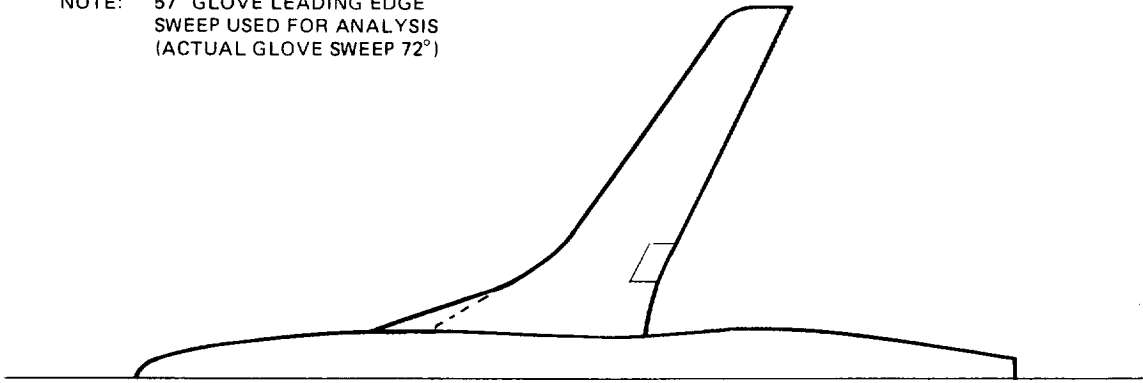


Figure 53. Supercritical Wing/Area-Ruled Fuselage Transport Configuration
(NASA TM X-3431)

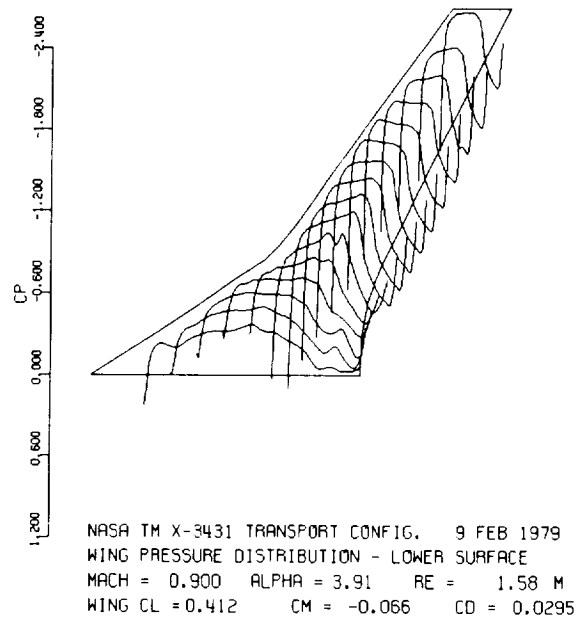
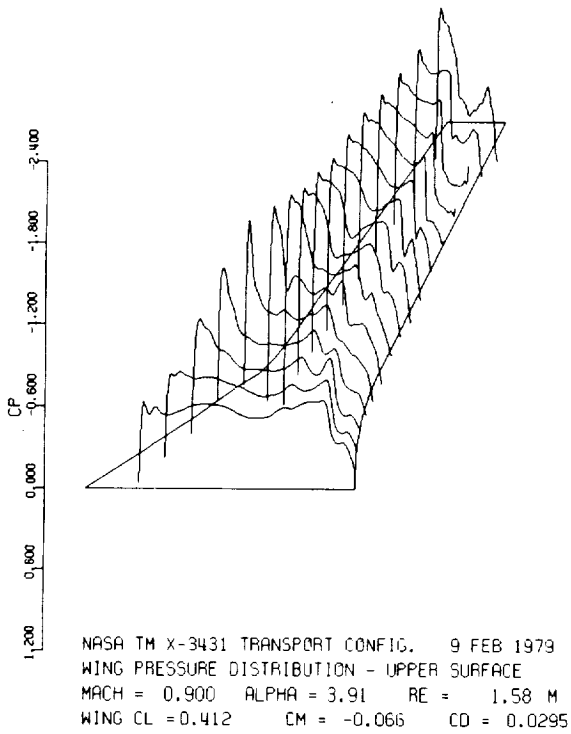


Figure 54. NASA TM X-3431 Transport Configuration Superimposed Computed Pressure Distributions for Basic Wing

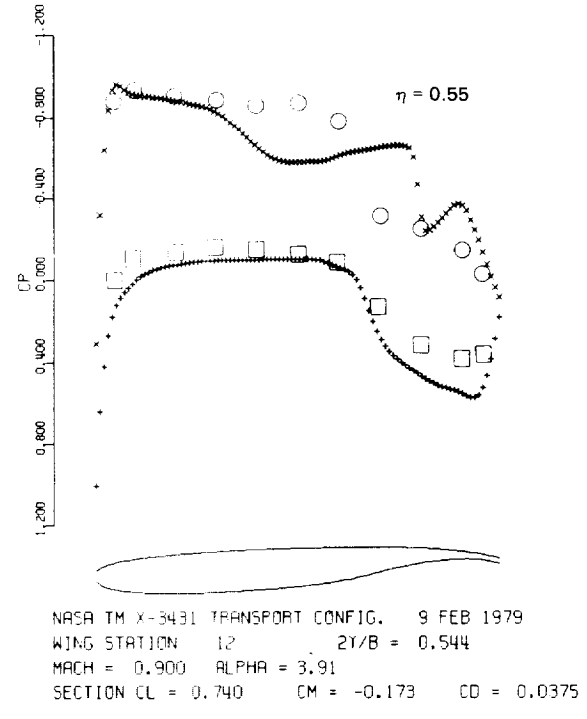
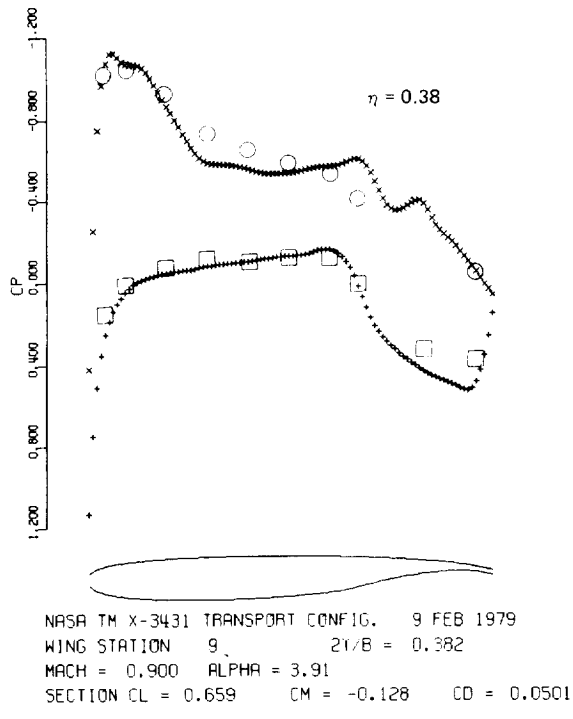
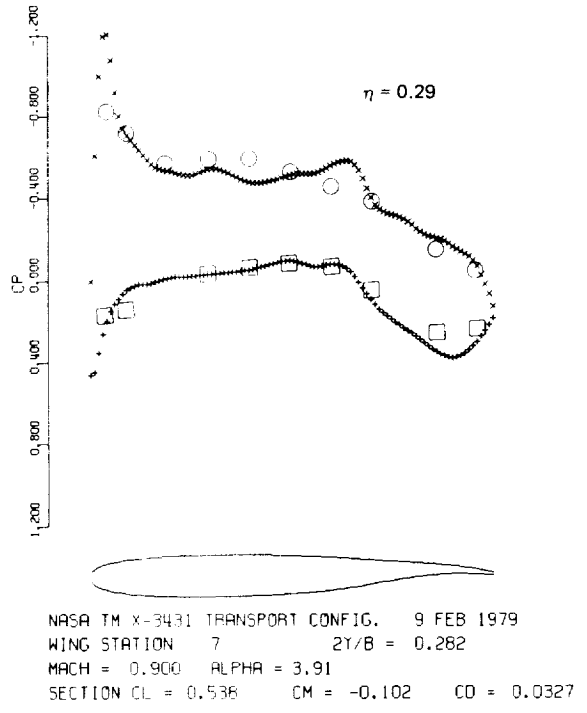
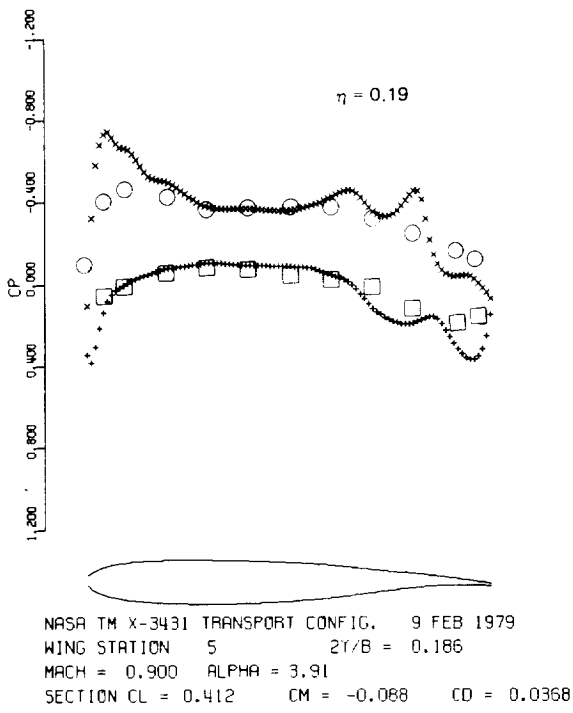
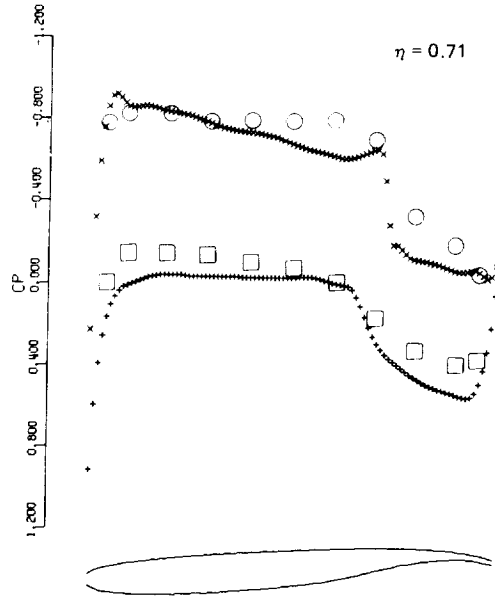
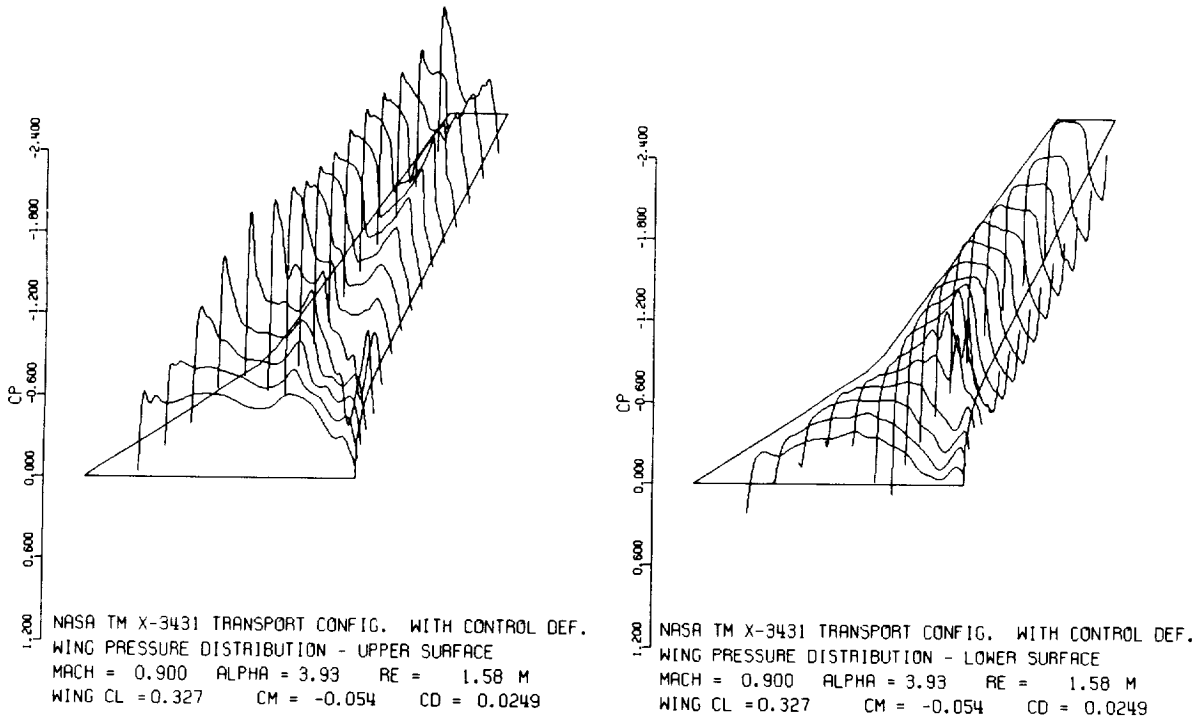


Figure 55. NASA TM X-3431 Transport Configuration Wing Pressure Distribution Correlation for Basic Wing (Sheet 1 of 2)



NASA TM X-3431 TRANSPORT CONFIG. 9 FEB 1979
 WING STATION 15 2T/B = 0.730
 MACH = 0.900 ALPHA = 3.91
 SECTION CL = 0.703 CM = -0.145 CD = 0.0158

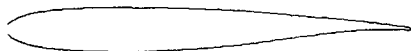
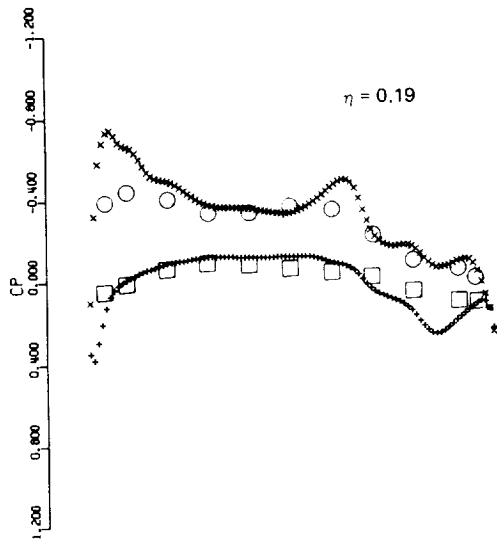
Figure 55. NASA TM X-3431 Transport Configuration Wing Pressure Distribution Correlation for Basic Wing (Sheet 2 of 2)



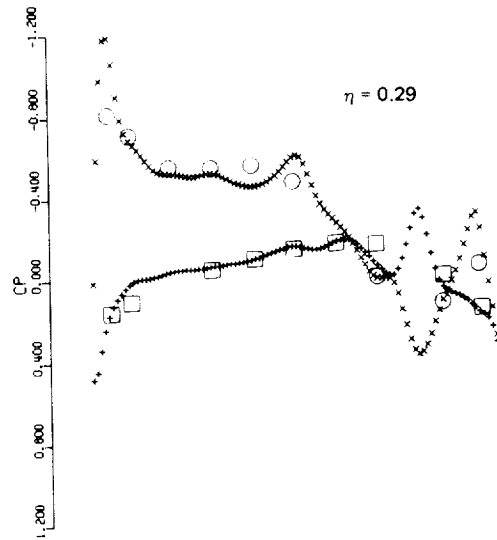
NASA TM X-3431 TRANSPORT CONFIG. WITH CONTROL DEF.
 WING PRESSURE DISTRIBUTION - UPPER SURFACE
 MACH = 0.900 ALPHA = 3.93 RE = 1.58 M
 WING CL = 0.327 CM = -0.054 CD = 0.0249

NASA TM X-3431 TRANSPORT CONFIG. WITH CONTROL DEF.
 WING PRESSURE DISTRIBUTION - LOWER SURFACE
 MACH = 0.900 ALPHA = 3.93 RE = 1.58 M
 WING CL = 0.327 CM = -0.054 CD = 0.0249

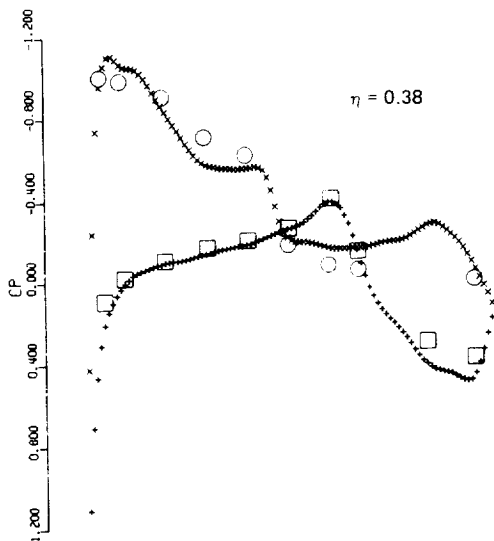
Figure 56. NASA TM X-3431 Transport Configuration Superimposed Computed Wing Pressures for Wing with Control Surface Deflected



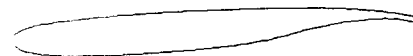
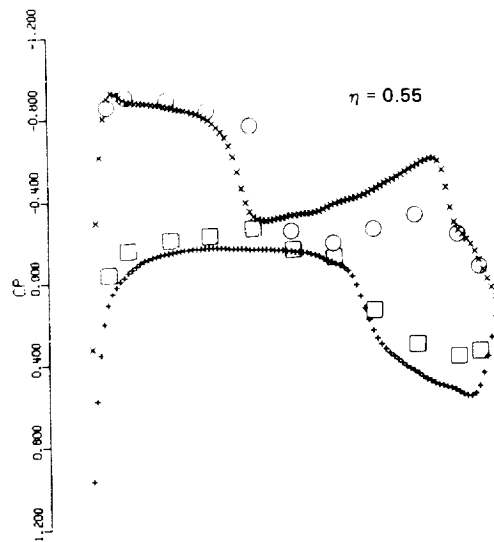
NASA TM X-3431 TRANSPORT CONFIG. WITH CONTROL DEF.
 WING STATION 5 $2Y/B = 0.186$
 MACH = 0.900 ALPHA = 3.93
 SECTION CL = 0.342 CM = -0.054 CD = 0.0291



NASA TM X-3431 TRANSPORT CONFIG. WITH CONTROL DEF.
 WING STATION 7 $2Y/B = 0.282$
 MACH = 0.900 ALPHA = 3.93
 SECTION CL = 0.291 CM = 0.014 CD = 0.0152

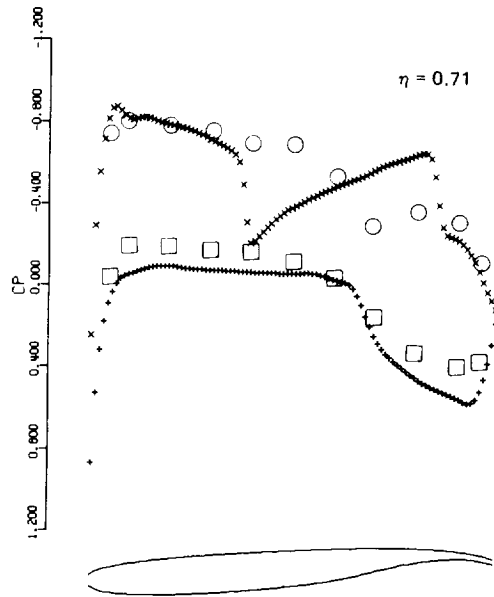


NASA TM X-3431 TRANSPORT CONFIG. WITH CONTROL DEF.
 WING STATION 9 $2Y/B = 0.382$
 MACH = 0.900 ALPHA = 3.93
 SECTION CL = 0.452 CM = -0.063 CD = 0.0401



NASA TM X-3431 TRANSPORT CONFIG. WITH CONTROL DEF.
 WING STATION 12 $2Y/B = 0.544$
 MACH = 0.900 ALPHA = 3.93
 SECTION CL = 0.603 CM = -0.150 CD = 0.0316

Figure 57. NASA TM X-3431 Transport Configuration Wing Pressure Distribution Correlation for Wing with Control Surface Deflection (Sheet 1 of 2)



NASA TM X-3431 TRANSPORT CONFIG. WITH CONTROL DEF.
 WING STATION 15 $2Y/B = 0.730$
 MACH = 0.900 ALPHA = 3.93
 SECTION CL = 0.644 CM = -0.165 CD = 0.0209

Figure 57. NASA TM X-3431 Transport Configuration Wing Pressure Distribution Correlation for Wing with Control Surface Deflection (Sheet 2 of 2)

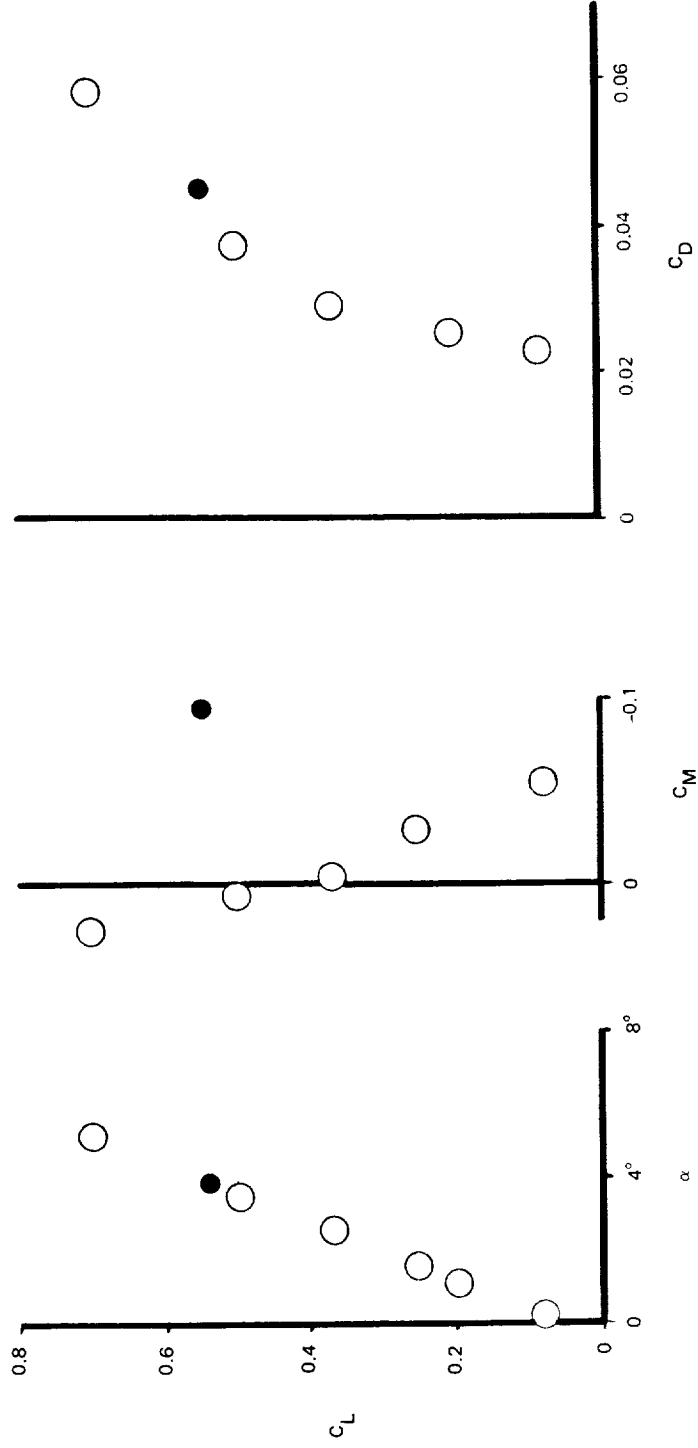


Figure 58. Force and Moment Correlation for Supercritical Wing/Area-Ruled Fuselage Transport Configuration, $M = 0.90, \alpha = 3.91^\circ$

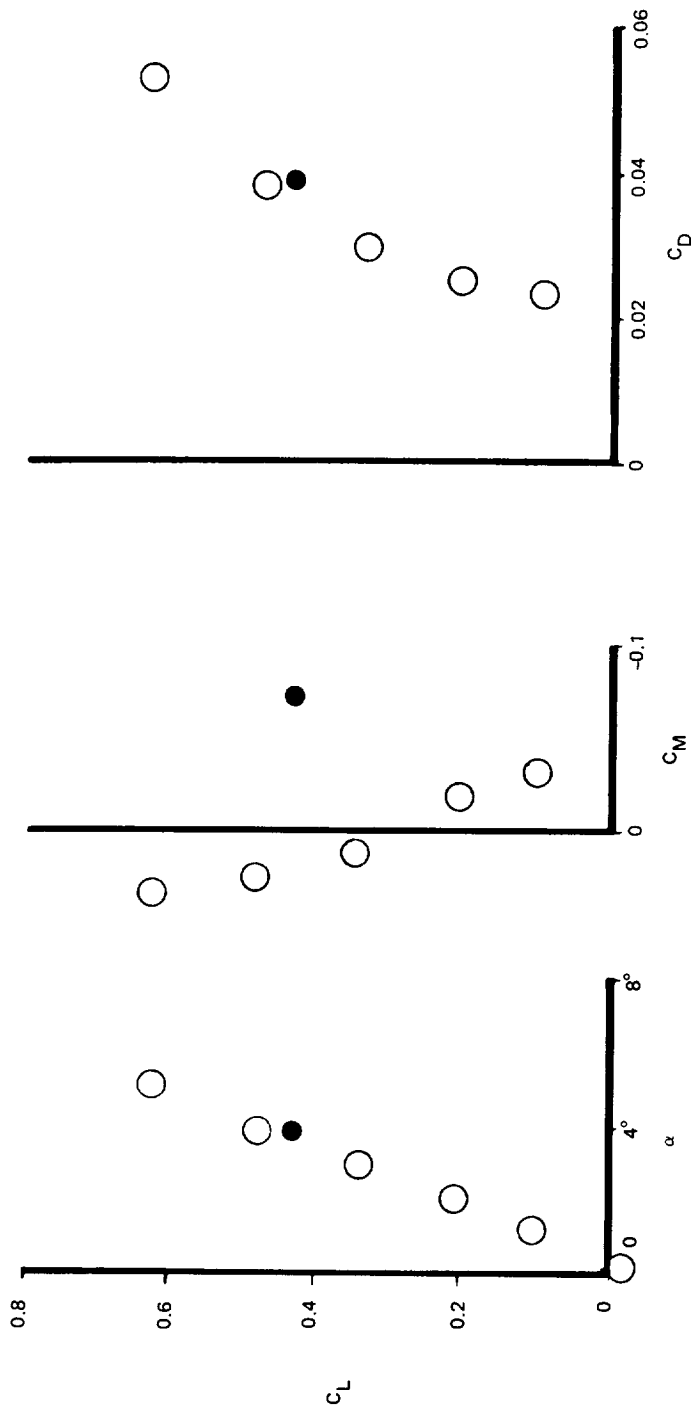
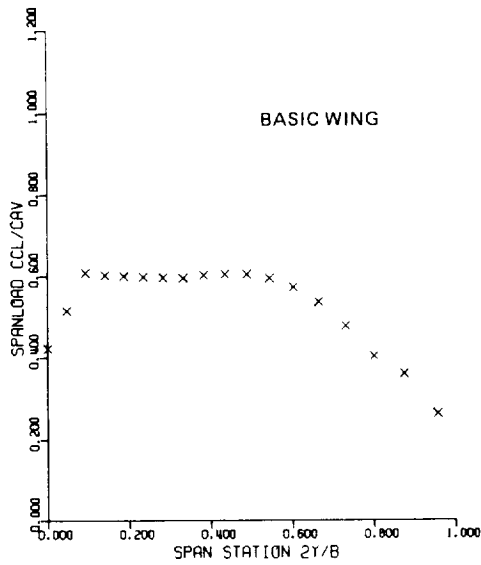
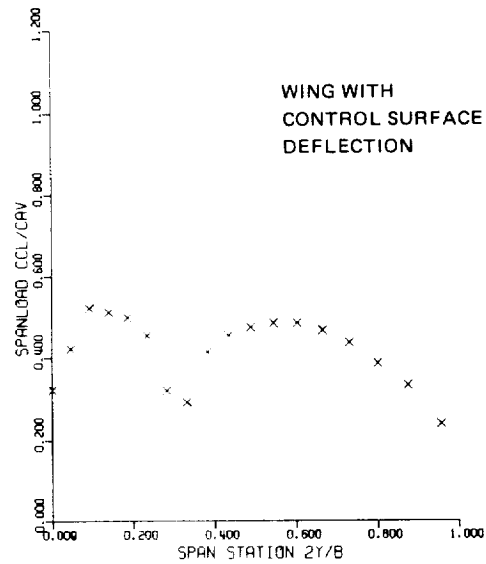


Figure 59. Force and Moment Correlation for Supercritical Wing/Area-Ruled Fuselage Transport Configuration with Wing Control Surface Deflection ($\delta F_2 = -15^\circ$)
 $M = 0.90, \alpha = 3.93^\circ$



NASA TM X-3431 TRANSPORT CONFIG. 9 FEB 1979
 SPAN EFFICIENCY $E = 0.911$
 LIFT INDUCED DRAG = 0.0116
 WAVE DRAG = 0.0106
 FRICTION DRAG = 0.0155



NASA TM X-3431 TRANSPORT CONFIG. WITH CONTROL DEF.
 SPAN EFFICIENCY $E = 0.722$
 LIFT INDUCED DRAG = 0.0092
 WAVE DRAG = 0.0084
 FRICTION DRAG = 0.0155

Figure 60. NASA TM X-3431 Transport Configuration Effect of Wing Control Surface Deflection on Computed Wing Spanload

CONCLUDING REMARKS

The present method provides certain advantages in both the design and analysis of wing-fuselage configurations at transonic speeds. These advantages are related to the high density resolution available and the grid system flexibility needed for treating complex three-dimensional shapes. However, to make these gains, some desirable features had to be sacrificed. In particular, the basic small disturbance-planar boundary condition approach exhibits certain limitations when compared to the more sophisticated full potential equation - exact boundary condition approach. This method can be used effectively if these limitations are understood.

It was pointed out in the grid system section that wing section leading edges are positioned between fine grid points. It is not possible to have a boundary point exactly at the leading edge, a restriction inherent in the small disturbance formulation. As a result, details of the flow in the wing section nose region are somewhat compromised. Unfortunately, the drag computations involve a pressure integration that includes the nose region where for blunt sections, a suction force naturally develops. For this region, it is expected that the present method will be useful in predicting drag increments but caution should be exercised when using the absolute drag levels.

It should be noted that for certain extreme geometric configurations and certain extreme flow conditions, computed small disturbance solutions may not correlate with the physical flow as well as a full potential equation solution. The Douglas wing-body configuration (Ref 39) is a good example (see Figure 61). This wing has 15% thick blunt wing sections. If the flow condition is mild, for example, below the drag divergence condition, comparisons with experimental data are good (see Figure 62 and 63). However, if flow conditions are extreme, beyond what would be considered the design point or drag divergence conditions, comparisons are somewhat compromised* (see Figure 64). However, computations indicate that the present method performs well for the more common geometries and flow conditions occurring in most practical applications. In particular, existing transports analyzed at normal cruise conditions have yielded excellent correlation with experimental data. To date, these transports include the Boeing KC-135, Grumman Gulfstream III, and Lockheed C-5A and C-141.

*See Comments on Convergence Criteria on Page 148.

Wing sweep can become a problem for any finite difference scheme employing a shearing transformation for the wing planform. The sheared coordinate lines were illustrated in Figure 9. As wing sweep increases, the two grid lines collapse on each other degrading resolution in the physical Y-direction. Depending on the application, the methods performance may be downgraded for wing sweep angles greater than 50 or 60 degrees.

Finally, a warning about analyzing complex shapes is in order. Experience has shown that the modeling and input of complex geometric shapes is error prone. It is hoped that users of this method will familiarize themselves first by analyzing simple shapes and slowly progress to more complicated shapes. The array of sample cases included in this report should provide a good starting point. In addition, the modular construction of the present code (isolated bodies and wings as well as wing-bodies) should prove to be useful in diagnosing both code usage and aerodynamic problems.

Future work will include the development of methodology for treating multiple body and multiple wing surfaces (see Figure 65).

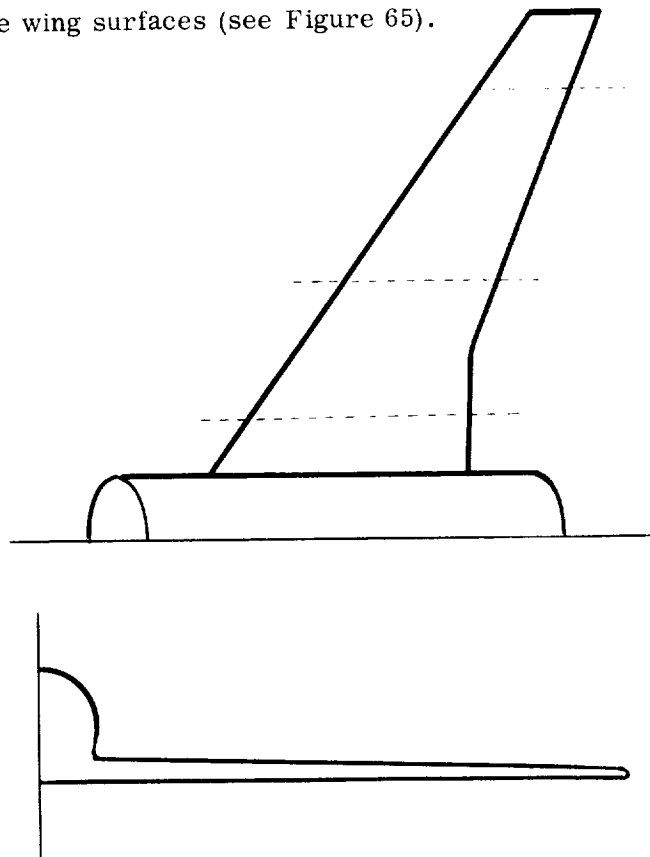


Figure 61. NASA-Douglas Supercritical Wing Transport Configuration

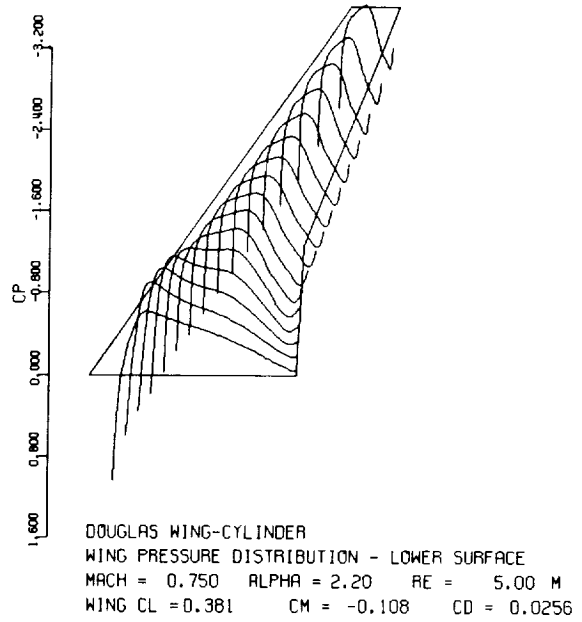
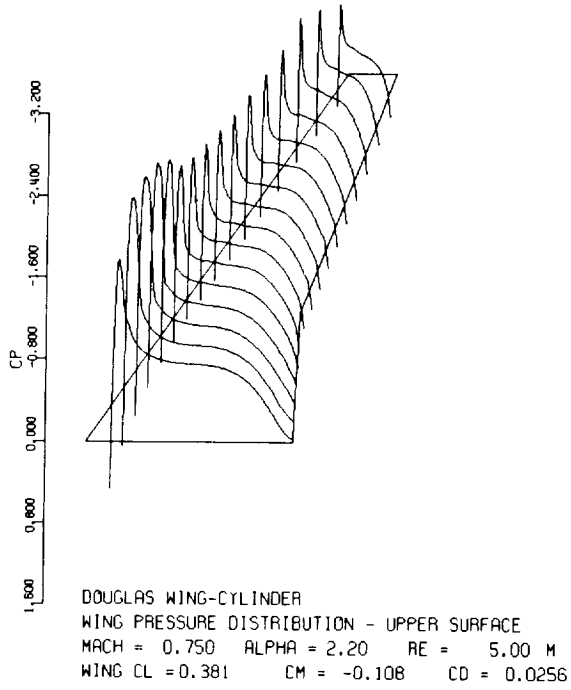


Figure 62. Douglas Transport Configuration Superimposed Computed Pressure Distributions
 $M_\infty = 0.75, \alpha = 2.2^\circ$

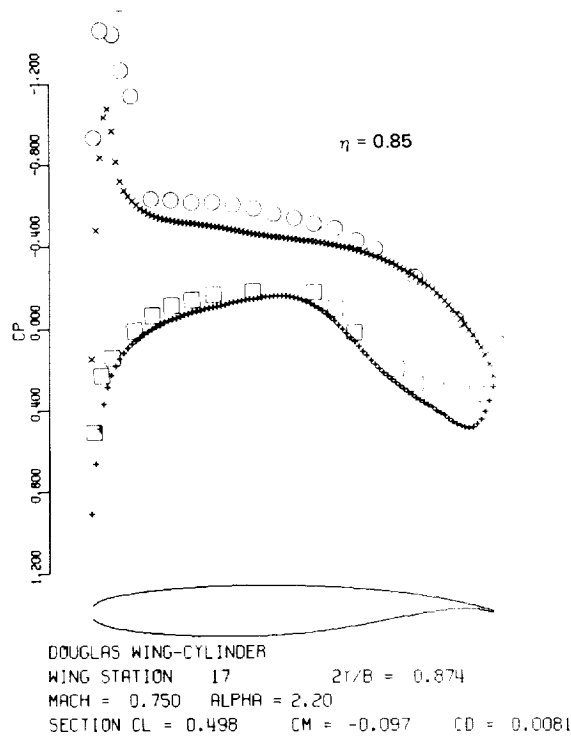
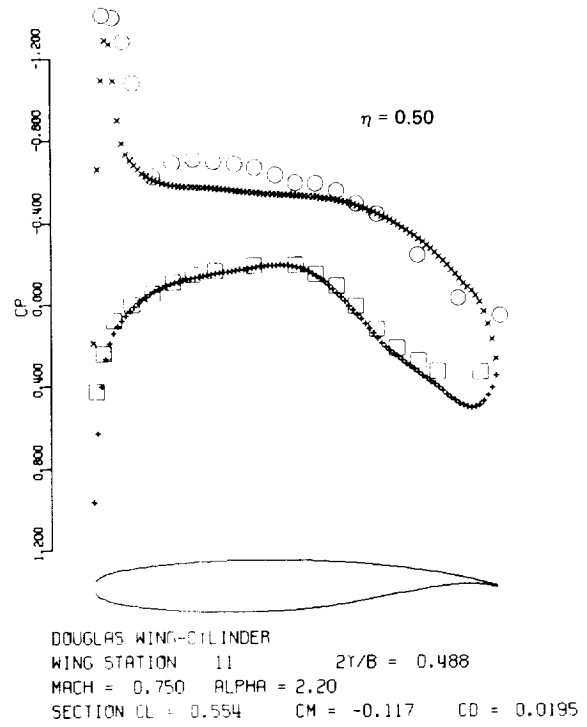
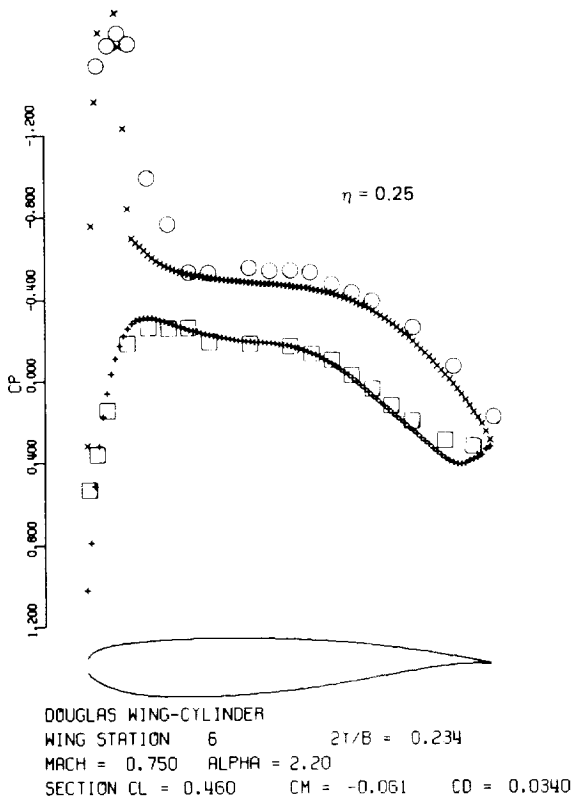
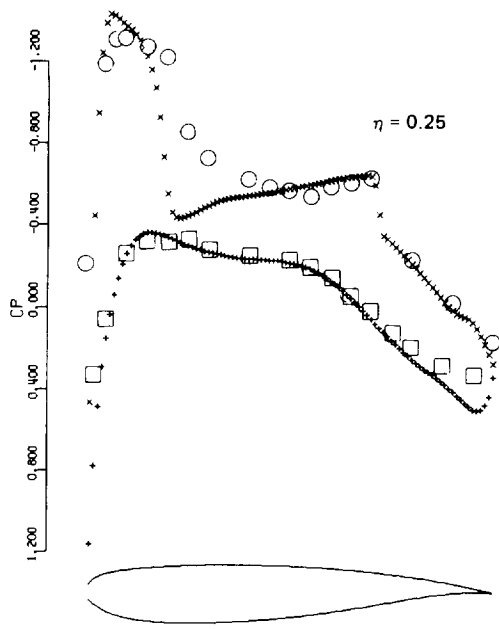
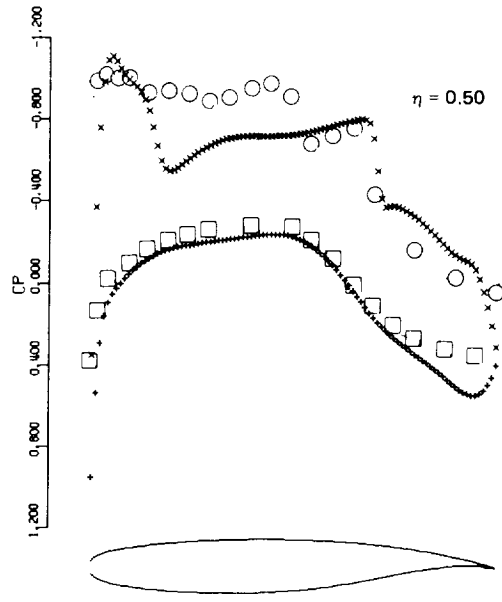


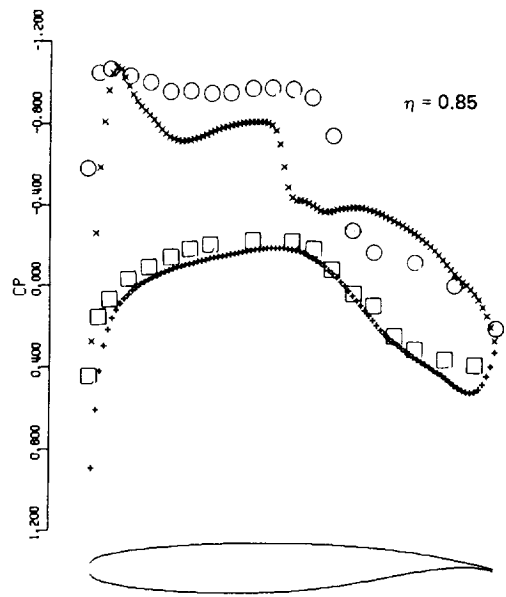
Figure 63. Douglas Transport Configuration Wing Pressure Distribution Correlation, $M_\infty = 0.75, \alpha = 2.2^\circ$



DOUGLAS WING-CYLINDER
 WING STATION 6 $2Y/B = 0.234$
 MACH = 0.840 ALPHA = 1.85
 SECTION CL = 0.510 CM = -0.087 CD = 0.0507



DOUGLAS WING-CYLINDER
 WING STATION 11 $2Y/B = 0.488$
 MACH = 0.840 ALPHA = 1.85
 SECTION CL = 0.629 CM = -0.145 CD = 0.0210



DOUGLAS WING-CYLINDER
 WING STATION 17 $2Y/B = 0.874$
 MACH = 0.840 ALPHA = 1.85
 SECTION CL = 0.590 CM = -0.105 CD = 0.0012

Figure 64. Douglas Transport Configuration Wing Pressure Distribution Correlation, $M_\infty = 0.84, \alpha = 1.85^\circ$

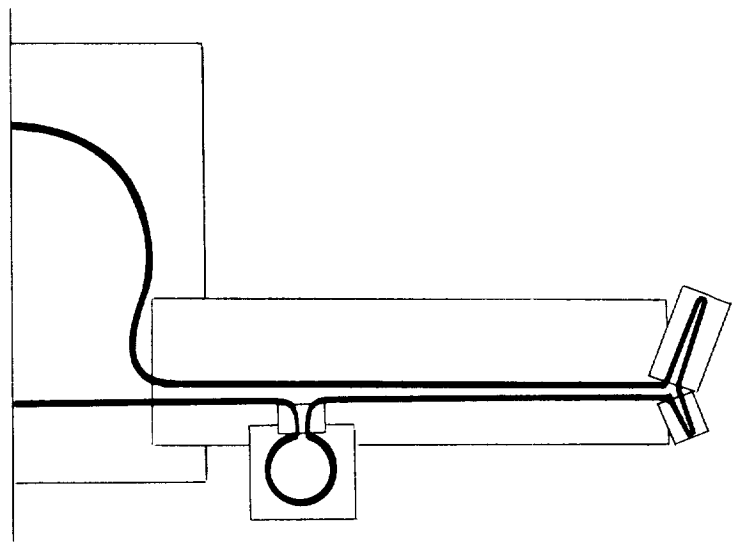


Figure 65. Future Grid Component Build-Up Capability for Complex Aircraft Configurations

APPENDIX
DESCRIPTION OF COMPUTER CODE WIBCO

CONTENTS

	<u>Page</u>
GENERAL COMPUTER CODE DESCRIPTION	99
INPUT DATA FORMAT	103
SAMPLE INPUT DATA SETS	107
OUTPUT DATA (PRINT AND PLOT) FORMAT	117
INPUT GEOMETRY VERIFICATION	121
SUBROUTINE CALL SEQUENCE	125
SUBROUTINE DESCRIPTIONS	131
KEY VARIABLE DESCRIPTIONS	137
RECOMMENDATIONS FOR USAGE	147

GENERAL COMPUTER CODE DESCRIPTION

The computer code is operational on both IBM and CDC type computers. Overlay structures are not used although this approach (for reducing core requirements) may be advantageous depending on facility charging algorithms. The IBM version using the extended H compiler (opt = 2) requires approximately 670K₁₀ for storage and execution. The CDC version with OPT = 1 compiler optimization and segmented loader requires about 236K₈ for storage and execution. There is considerable use of temporary disk storage units. Since interpolation and searching is required, a result of the mesh embedding approach, it is useful to have planar potential (ϕ) arrays separate and addressable. As a result, 72 different units (16 CDC units) are currently employed. The disk unit number and a description of contents are listed below.

<u>DISK NUMBER</u>	<u>DESCRIPTION</u>
1	Input data transferred to Unit 1
7	Flowfield potentials for save/re-start capability
8	Quick-geometry problem diagnosis printed-output
10-35 (1 CDC Unit)	Global crude grid potential array
41-58 (1 CDC Unit)	Fine wing grid potential array
61-76 (1 CDC Unit)	Fine body grid potential array
80	Crude grid wing upper/lower surface boundary conditions
81	Fine wing grid upper/lower surface boundary conditions
82	Fine wing grid x-coordinate array
83	Fine wing grid section surface ordinates
84	Crude grid body surface normal (direction cosines)
85	Fine grid body surface normal (direction cosines)
86	Fine wing grid shearing angles
87	Wing and body pressure coefficient arrays
88	Boundary layer displacement thickness slope

Computer running time will of course vary depending on the facility and the mode of operation or operating system. The absolute levels specified may be out dated shortly after they are specified. IBM 370 running times are specified below, however, since the relative increment for various options will remain essentially steady and these increments will be useful in estimating the time and cost of using different options.

<u>CASE</u>	<u>TIME (CPU Minutes)</u>
Isolated body	17 (50 crude/50 crude-fine iterations)
Isolated wing	37 (100 crude/80 crude-fine iterations)
Isolated wing w/ viscous interaction	43 (100 crude/80 crude-fine iterations)
Wing-body (body modelled in crude grid only)	37 (100 crude/80 crude-fine iterations)
Wing-body (body modelled in fine grid)	50 (100 crude/80 crude-fine iterations)
Geometry/Grid verification	1 (No iterations)

An effort has been made to minimize the amount of data required to define the configuration geometry and flow condition. This should simplify matters for most applications involving configuration analysis and reduce the chances for input errors. For example, the computational grid systems (extent and density) have been set in the FORTRAN coding to provide good results under most conditions. Occasionally, it will be advantageous to manipulate the preset values and limiters. FORTRAN coding changes will be necessary if this is the case. The following values and limiters may be modified in certain special applications.

- 1) Gas constant ($\gamma = 1.4$)
- 2) Fine wing/body embedded grid limits or extent

- 3) Fine wing/body embedded grid density
- 4) Subsonic relaxation factor ($\omega = 1.5$)
- 5) Boundary layer transition ($X/C_{\text{tran}} = 0.05$)
- 6) The number of inviscid cycles between each viscous calculation
(currently set to 20)

All of the sample cases were computed using the basic code without modification. If code modifications of type (2) or (3) are made care must be taken to insure that common and dimensioned arrays are sufficient and consistent.

The input data format description can be found on the following pages. The descriptions are thought to be relatively straight forward except in the case of wing section definition. It is important to extend wing planform/section definition to the symmetry plane even for wing-body configurations (see Figure 25). This serves several purposes. First, the code will compute a wing-body juncture which will be a function of both the configuration geometry and the computational grid system. If the computational juncture is slightly inboard of the geometric juncture, section definition in this region becomes important. Second, the input planform shape provides both the aspect ratio for the lift-induced drag computation and the reference lengths and areas used to reduce the integrated pressures to give force and moment coefficients. Finally, the data input for defining a wing-body configuration can be used directly for the isolated wing case. This feature can be used to study wing-body interference effects.

It is important to note that there is no provision for input of reference lengths and areas. These reference values are computed from the input geometry and printed at the end of the output stream. If reference values other than those computed are used experimentally, the computed force and moment coefficients must be appropriately scaled.

LOCATION OF INPUT DATA READ STATEMENTS

<u>CARD(S)</u>	<u>ROUTINE</u>
1-A THRU 3-B	MAIN
4-B	QWIKDE
5-B THRU 9-B	CSMDEF
10-B THRU 13-B	BLMDEF

INPUT DATA FORMAT

Excluding literal cards, all input data cards are punched in seven field ten digit format (7F10.0).* A decimal point is required in each field.

<u>CARD NUMBER</u>	<u>CARD COLUMN</u>	<u>VARIABLE NAME</u>	<u>DESCRIPTION</u>
Card 1-A	1-80	TITLE	Configuration or run title to identify graphic and printed output.
Card 2-A	1-10	CASE	CASE = 1. Isolated Body (omit cards -W) CASE = 2. Isolated Wing (omit cards -B) CASE = 3. Wing-Body
	11-20	AMACH	Mach Number (AMACH < 1.0)
	21-30	AOA	Angle-of-Attack (degrees)
	31-40	RE	Reynolds Number ($\times 10^6$)
	41-50	AXIT	Number of initial crude grid iterations. (AXIT = 0. for geometry verification only)
	51-60	AXITF	Number of crude/fine grid iteration cycles.
	61-70	VISMOD	VISMOD = 1. No viscous effects. VISMOD = 2. Viscous effects computed at end of inviscid analysis. VISMOD = 3. Inviscid/viscous interaction.
NOTE: Omit card set 1-W through 5-W for CASE = 1.			
Card 1-W	1-10	ASECT	Number of streamwise sections defining wing planform ($2 \leq \text{ASECT} \leq 20$).
	11-20	ANIN	Number of ordinates defining each wing section (ANIN ≤ 60).

*NOTE: Card columns 71-80 on card 2-A have been reserved for the variable START which provides a solution re-start capability.

START = 0. Conventional solution

START = 1. Writes/saves flow field on tape unit 7

START = 2. Restarts with tape 7 as input - does not save resulting solution

START = 3. Same as 2. But final solution is saved on tape unit 7

<u>CARD NUMBER</u>	<u>CARD COLUMN</u>	<u>VARIABLE NAME</u>	<u>DESCRIPTION</u>
Card 1-W (cont'd)	21-30	ANOSW	ANOSW = 0. Sharp nose wing sections. ANOSW = 1. Blunt nose wing sections.
	31-40	XMOM	X-position about which moment is to be computed.
	41-50	ZWING	Z-position of wing (waterline).
	51-60	WPO	WPO = 0. No crude grid output. WPO = 1. Crude grid output for diagnostic purposes.
	61-70	WS	Wing Cp distribution plot scaling per inch (typically 0.4 or 0.8).

NOTE: Card set 2-W through 5-W is repeated ASECT times.

Card 2-W	1-10	XPL	Wing section leading edge (X-value).
	11-20	YP	Wing section span position (Y-value). First Y-value must be 0.0 (symmetry plane), even for wing-body case.
	21-30	XPT	Wing section trailing edge (X-value).
	31-40	TWIST	Wing section local incidence (twist angle in degrees).
	41-50	AKODE	AKODE = 0. Section ordinates identical to preceding section (omit cards 3-W through 5-W). AKODE = 1. New section definition expected on cards 4W and 5W
Card 3-W	1-70	XINW	Wing section X-coordinates (cards 3-W defined only for first wing section, ANIN values expected).
Card 4-W	1-70	YINU	Wing section upper surface Y-coordinates (ANIN values).
Card 5-W	1-70	YINL	Wing section lower surface Y-coordinates (ANIN values).

NOTE: Omit card set 1-B through 13-B for CASE = 2

Card 1-B	1-10	BKOD = 1.	Infinite cylinder (only RADIUS need be input).
		BKOD = -1.	Same as BKOD = 1. No embedded body grid. Crude grid body representation only.
		BKOD = 2.	Simple axisymmetric body definition requested (input BXIN, RIN on card(s) 2-B and 3-B).
		BKOD = -2.	Same as BKOD = 2. No embedded body grid. Crude grid body representation only.

<u>CARD NUMBER</u>	<u>CARD COLUMN</u>	<u>VARIABLE NAME</u>	<u>DESCRIPTION</u>
Card 1-B (cont'd)		BKOD = 3.	Complex body definition requested (input Quick-Geometry model on card(s) 4-B through 13-B).
		BKOD = -3.	Same as BKOD = 3. No embedded body grid. Crude grid body representation only.
	11-20	BNOSE	Body nose (X-value) } For BKOD = ±2. or ±3. Body tail (X-value) }
	21-30	BTAIL	
	31-40	BNIN	Number of axisymmetric body coordinates to be input. BNIN ≤ 60 (for BKOD = ±2 only).
	41-50	RADIUS	Cylinder radius for BKOD = ±1 only.
	51-60	ANOSB	ANOSB = 0. Sharp nose body } BKOD = ±2 only. ANOSB = 1. Blunt nose body }
	61-70	BS	Body Cp plot scaling per inch (typically 0.08).

NOTE: Omit card sets 2-B and 3-B for BKOD = 1 or BKOD = 3.

Card(s) 2-B	1-70	XINB	Axisymmetric body X-coordinates (BNIN values).
-------------	------	------	--

Card(s) 3-B	1-70	RIN	Axisymmetric body radii (BNIN values).
-------------	------	-----	--

NOTE: Omit card sets 4-B through 13-B for BKOD = 1 or BKOD = 2.

Card 4-B	1-70	VTITLE	Quick-Geometry model title.
----------	------	--------	-----------------------------

Card 5-B	1-10	ACSM	Number of distinct cross-section models (ACSM card sets 6-B and 7-B will follow).
----------	------	------	---

Card 6-B	1-10	ADUM	Running count of current cross-section model (1-ACSM).
----------	------	------	--

	11-20	AARC	Number of arcs in current cross-section model (AARC Card(s) 7-B will follow).
--	-------	------	---

	21-60	CTITLE	Title or descriptor of current cross-section model.
--	-------	--------	---

Card 7-B	1-8	ARCNAM	Arc or component name.
----------	-----	--------	------------------------

	11-14	ASHAPE	Arc or component shape.
--	-------	--------	-------------------------

	21-28	PNTNAM(1)	Control point name for beginning of this arc.
--	-------	-----------	---

	31-38	PNTNAM(2)	Control point name for termination of this arc.
--	-------	-----------	---

	41-48	PNTNAM(3)	Slope control point name for this arc, if required.
--	-------	-----------	---

Card 8-B	1-10	ANTCSM	Number of cross-section models to define entire body (ANTCSM card(s) 9-B will follow).
----------	------	--------	--

<u>CARD NUMBER</u>	<u>CARD COLUMN</u>	<u>VARIABLE NAME</u>	<u>DESCRIPTION</u>
Card 9-B	1-10	ADUM	Running count of current cross-section model (1-ANTCSM)
	11-20	AMODEL	Index corresponding to already defined cross-section models (between 1 and ACSM).
	21-30	XCSMS1	Starting X-station for current cross-section model.
	31-40	XCSMS2	Ending X-station for current cross-section model.
Card 10-B	1-10	BLINE	Number of body line models to be defined by segments (BLINE card sets 11-B and 12-B follow).
	11-20	ALIAS	Number of body line models to be aliased (Alias card(s) 13-B follow).
Note: Card set 11-B and 12-B is repeated BLINE times.			
Card 11-B	1-10	BLSEG	Number of segment(s) defining body line model.
	11	BYORZ	The letter Y or Z indicates which data definition is to follow.
	12-19	BNAME	Body line name to be defined.
Card 12-B	1-4	SSHAPE	Segment shape.
	11-20	D(1)	X-station for beginning of segment.
	21-30	D(2)	Y or Z value corresponding to D(1).
	31-40	D(3)	X-station for termination of segment.
	41-50	D(4)	Y or Z value corresponding to D(3).
	51-60	D(5)	X-station for segment slope control point.
	61-70	D(6)	Y or Z value corresponding to D(5)
Note: Card set 13-B is repeated ALIAS times.			
Card 13-B	11	BYORZ	The letter Y or Z indicates which data definition is to follow.
	12-19	BNAME	Body line name to be defined.
	21	AYORZ	The letter Y or Z indicates which definition is to be used for aliasing.
	22-29	ANAME	Body line name to which BNAME is aliased.).

SAMPLE INPUT DATA SETS

(8 CASES)

NOTE: These data sets were used for the correlation studies
(See Comparisons Section, page 55)

Case No. 1
NACA RM L53F07 ISOLATED BODY

1.0	0.99	8.4	1.0	50.	50.	1.0
2.	0.	100.	32.	0.	0.	3.08
0.	0.5	0.75	1.25	2.50	5.00	7.50
10.0	15.0	20.0	25.0	30.0	35.0	40.0
45.0	50.0	55.0	60.0	65.0	70.0	75.0
80.0	85.0	89.0	90.0	91.0	92.0	93.0
94.0	95.0	96.0	100.0			
0.	0.231	0.298	0.428	0.722	1.205	1.613
1.971	2.593	3.090	3.465	3.741	3.933	4.063
4.143	4.167	4.130	4.024	3.842	3.562	3.128
2.526	1.852	1.265	1.120	1.005	0.925	0.872
0.841	0.833	0.833	0.833			

Case No. 2
NACA TND 7331 ISOLATED BODY

1.0	0.991	0.0	1.0	50.	50.	1.0
2.	0.	100.	44.	0.	1.	3.08
0.	0.2	0.4	0.6	0.8	1.0	1.2
1.4	1.6	1.8	2.0	4.0	6.0	8.0
10.0	12.0	14.0	16.0	18.0	20.0	24.0
28.0	32.0	40.0	48.0	50.0	52.0	50.0
68.0	72.0	76.0	80.0	82.0	84.0	86.0
88.0	90.0	92.0	94.0	96.0	97.0	98.0
99.0	100.0					
0.	0.696	0.946	1.134	1.291	1.422	1.539
1.645	1.742	1.832	1.916	2.556	3.005	3.357
3.648	3.894	4.108	4.295	4.460	4.607	4.855
5.052	5.207	5.412	5.497	5.500	5.497	5.412
5.207	5.052	4.855	4.607	4.460	4.295	4.108
3.894	3.648	3.357	3.005	2.556	2.271	1.916
1.422	1.422					

Case No. 3
GULFSTREAM II ISOLATED FUSELAGE NOSE

1.	0.80	3.1	1.0	50.	50.	1.0
3.	8.0	200.0	0.	0.	0.	0.4
GULFSTREAM FUSELAGE QUICK-GEOMETRY MODEL						
3.						
1. NOSE TO WINDSHIELD BASE						
BODYLO	ELLI	BDYBCL	BDYMHB	BDYLSCP		
BODYHI	ELLI	BDYMHB	BDYTCL	BDYUSCP		
2. WINDSHIELD						
CANLO	ELLI	BDYBCL	BDYMHB	BDYLSCP		
CANSI	ELLI	BDYMHB	CANLOW	CANLSCP		
WINDF	LINE	CANLOW	BDYTCL			
3. CANOPY						
CANPLO	ELLI	BDYBCL	BDYMHB	BDYLSCP		
CANPSI	ELLI	BDYMHB	CANLOW	CANLSCP		
WINDSI	LINE	CANLOW	CANHIE			
CANOPUP	ELLI	CANHIE	BDYTCL	CANTSCP		
4.						
1.	1.	8.0	64.0			
2.	2.	64.0	83.5			
3.	3.	83.5	133.0			
4.	1.	133.0	200.0			
10.	11.					
2. ZBDYBCL						
ELLX	8.0	78.5	133.0	53.0	8.0	53.0
LINE	133.0	53.0	200.0	53.0		
4. ZBDYTCL						
ELLX	8.0	78.5	64.0	113.5	8.0	94.5
LINE	64.0	113.5	83.5	132.5		
CUBI	83.5	132.5	133.0	147.0	98.0	147.0
LINE	133.0	147.0	200.0	147.0		
1. YCENTER						
LINE	8.0	0.0	200.0	0.0		
2. ZBDYMHB						
CUBI	8.0	78.5	181.0	100.0	135.5	100.0
LINE	181.0	100.0	200.0	100.0		
1. YBDYMHB						
ELLX	8.0	0.	200.0	47.0	8.0	47.0
1. ZCANLOW						
LINE	64.0	113.5	133.0	113.5		
1. ZCANHIE						
LINE	83.5	132.5	133.0	132.5		
2. YCANLOW						
LINE	64.0	0.	79.5	28.0		
LINE	79.5	28.0	133.0	42.0		
2. YCANHIE						
LINE	83.5	0.	96.0	24.5		
LINE	96.0	24.5	133.0	34.0		
1. YCANTSCP						
LINE	83.5	0.	133.0	22.0		
ZMAPAXIS	ZBDYMHB					
YMAPAXIS	YCENTER					
ZCANTSCP	ZBDYTCL					
ZCANLSCP	ZCANLOW					
YCANLSCP	YBDYMHB					
YBDYTCL	YCENTER					
YBDYBCL	YCENTER					
YBDYLSCP	YBDYMHB					
ZBDYLSCP	ZBDYBCL					
YBDYUSCP	YBDYMHB					
ZBDYUSCP	ZBDYTCL					

Case No. 4
ONERA M6 ISOLATED WING

2.	0.8407	3.01	2.5	100.	80.	1.0
2.	24.	1.0	0.452	0.	1.	0.4
0.	0.	1.0	0.	0.		
0.	0.25441	0.45704	0.98413	1.94609	2.97008	5.41248
9.56354	16.49976	21.87096	27.17978	32.42726	37.61446	42.74223
47.81197	55.30937	60.23757	65.11093	69.93027	77.05998	84.07324
90.61905	96.61860	100.0				
0.	0.97958	1.17419	1.68984	2.24545	2.58245	3.03278
3.57742	4.19089	4.50507	4.71987	4.84902	4.89296	4.84888
4.71661	4.36741	4.05241	3.68990	3.29402	2.65505	1.95838
1.22389	0.48907	0.07052				
0.	-0.97958	-1.17419	-1.68984	-2.24545	-2.58245	-3.03278
-3.57742	-4.19089	-4.50507	-4.71987	-4.84902	-4.89296	-4.84888
-4.71661	-4.36741	-4.05241	-3.68990	-3.29402	-2.65505	-1.95838
-1.22389	-0.48907	-0.07052				
0.85670	1.4838	1.3944	0.	0.		

Case No. 5
NACA RM A9K01 ISOLATED WING

2.	0.8500	4.00	2.0	100.	80.	3.
2.	25.	1.0	25.480	0.	1.0	0.6
0.	0.	26.67	0.	0.		
0.	0.465	0.733	1.275	2.644	5.388	8.129
10.859	16.279	21.647	26.959	32.213	37.413	42.555
47.644	52.674	57.649	62.569	67.433	72.242	76.998
91.701	86.350	90.948	95.497	100.0		
0.	0.908	1.103	1.411	1.961	2.754	3.355
3.846	4.614	5.175	5.580	5.845	5.978	5.983
5.816	5.525	5.135	4.666	4.133	3.551	2.934
2.297	1.662	1.049	0.484	0.		
0.	-0.820	-0.979	-1.221	-1.632	-2.196	-2.608
-2.939	-3.439	-3.794	-4.035	-4.177	-4.220	-4.155
-3.968	-3.673	-3.307	-2.887	-2.432	-1.954	-1.471
-1.003	-0.573	-0.216	0.022	0.		
45.625	60.0	58.955	-0.6	0.		

Case No. 6
 NACA RM L51F07 AXI-SYM BODY/45 DEG SWEPT WING

3.	0.93	4.0	2.02	100.	80.	2.0
2.	26.	1.0	20.	0.0	1.0	0.6
12.625	0.	20.125	0.	1.0		
0.	0.5	0.75	1.25	2.5	5.0	7.5
10.0	15.0	20.0	25.0	30.0	35.0	40.0
45.0	50.0	55.0	60.0	65.0	70.0	75.0
80.0	85.0	90.0	95.0	100.0		
0.	0.464	0.563	0.718	0.981	1.313	1.591
1.824	2.194	2.474	2.687	2.842	2.945	2.996
2.992	2.925	2.793	2.602	2.364	2.087	1.775
1.437	1.083	0.727	0.370	0.013		
0.	-0.464	-0.563	-0.718	-0.981	-1.313	-1.591
-1.824	-2.194	-2.474	-2.687	-2.342	-2.945	-2.996
-2.992	-2.925	-2.793	-2.602	-2.364	-2.087	-1.775
-1.437	-1.083	-0.727	-0.370	-0.013		
25.375	12.0	29.875	0.	0.		
2.	0.	33.333	25.	0.	0.0	0.4
0.	0.2	0.3	0.5	1.0	2.0	3.0
4.0	6.0	8.0	10.0	12.0	14.0	16.0
18.0	20.0	22.0	24.0	26.0	28.0	30.0
32.0	33.0	33.333	33.8			
0.	0.0924	0.1192	0.1712	0.2888	0.4820	0.6452
0.7884	1.0372	1.2360	1.3860	1.4964	1.5732	1.6252
1.6572	1.6668	1.6520	1.6096	1.5368	1.4248	1.2512
1.0104	0.88	0.833	0.833			

Case No. 7
BOEING KC-135 TRANSPORT

3.	.78	2.0	5.25	100.	80.	1.
5.	26.	0.	52.90	-4.25	1.	0.8
28.66	0.0	70.27	1.8	1.0		
0.	0.5	0.75	1.25	2.50	5.0	7.5
10.	15.	20.	25.	30.	35.	40.
45.	50.	55.	60.	65.	70.	75.
80.	85.	90.	95.	100.		
0.740	1.750	2.055	2.539	3.470	4.830	5.813
6.572	7.661	8.380	8.860	9.137	9.218	9.105
8.766	9.258	7.620	6.870	6.029	5.168	4.300
3.445	2.584	1.723	0.861	0.		
0.000	-0.872	-1.076	-1.390	-1.915	-2.613	-3.178
-3.665	-4.510	-5.228	-5.757	-6.104	-6.275	-6.250
-6.044	-5.678	-5.185	-4.618	-4.041	-3.464	-2.886
-2.309	-1.732	-1.155	-0.577	0.		
32.02	4.37	62.89	1.8	0.		
36.38	10.36	57.86	1.76	1.		
0.536	1.399	1.654	2.060	2.840	3.998	4.850
5.511	6.436	7.070	7.500	7.760	7.920	7.910
7.725	7.382	6.895	6.284	5.570	4.782	3.985
3.188	2.391	1.594	0.797	0.		
0.000	-0.733	-0.895	-1.123	-1.475	-1.915	-2.290
-2.646	-3.318	-3.925	-4.401	-4.746	-4.980	-5.070
-5.007	-4.793	-4.448	-3.995	-3.496	-2.996	-2.497
-1.598	-1.498	-0.999	-0.499	0.		
41.41	16.73	59.20	1.70	1.0		
0.374	1.123	1.340	1.687	2.350	3.360	4.114
4.699	5.530	6.047	6.422	6.666	6.805	6.829
6.736	6.509	6.136	5.643	5.049	4.380	3.687
2.929	2.107	1.465	0.732	0.		
0.000	-0.570	-0.684	-0.837	-1.053	-1.307	-1.544
-1.787	-2.265	-2.731	-3.118	-3.425	-3.642	-3.763
-3.782	-3.676	-3.487	-3.174	-2.787	-2.389	-1.991
-1.593	-1.194	-0.796	-0.398	0.		
50.81	29.30	64.90	1.44	1.0		
0.306	0.997	1.198	1.519	2.160	3.130	3.857
4.423	5.210	5.704	6.050	6.280	6.430	6.449
6.370	6.178	5.850	5.412	4.880	4.267	3.605
2.904	2.178	1.452	0.726	0.		
0.000	-0.465	-0.558	-0.657	-0.750	-0.895	-1.041
-1.187	-1.479	-1.770	-2.059	-2.275	-2.445	-2.543
-2.568	-2.501	-2.330	-2.078	-1.818	-1.558	-1.299
-1.039	-0.775	-0.520	-0.260	0.		
69.27	53.96	74.97	0.80	0.		
-2.	0.0	108.30	22.	5.04	1.	.4
0.	2.0	4.0	6.0	8.0	10.0	12.0
14.0	16.0	20.0	30.0	40.0	50.0	60.0
70.0	78.0	80.0	85.0	90.0	95.0	100.0
108.3						
0.	2.50	3.35	3.90	4.30	4.60	4.80
4.95	5.04	5.04	5.04	5.04	5.04	5.04
5.04	5.04	4.92	4.65	4.20	3.55	2.65
2.60						

Case No. 8
NASA TM X-3431 TRANSPORT CONFIG.

3.	0.900	3.91	1.58	100.	80.	3.0
18.	25.	1.0	73.075	-2.5	1.0	0.6
36.3	0.	73.296	0.5	0.		
0.	0.0025	0.0050	0.0100	0.0150	0.0250	0.0500
0.0750	0.100	0.150	0.200	0.250	0.300	0.400
0.500	0.550	0.600	0.650	0.700	0.750	0.800
0.850	0.900	0.950	1.000			
-0.0225	-0.0153	-0.0119	-0.0075	-0.0043	0.0003	0.0078
0.0140	0.0182	0.0242	0.0283	0.0305	0.0307	0.0263
0.0173	0.0124	0.0074	0.0024	-0.0031	-0.0086	-0.0146
-0.0212	-0.0279	-0.0343	-0.0424			
-0.0225	-0.0296	-0.0331	-0.0376	-0.0410	-0.0465	-0.0555
-0.0618	-0.0664	-0.0728	-0.0776	-0.0808	-0.0828	-0.0834
-0.0797	-0.0751	-0.0700	-0.0642	-0.0584	-0.0525	-0.0468
-0.0434	-0.0424	-0.0435	-0.0448			
45.5	5.961	78.407	0.5	0.		
53.2	11.041	79.277	0.5	1.		
-0.0502	-0.0417	-0.0369	-0.0338	-0.0305	-0.0252	-0.0162
-0.0110	-0.0074	-0.0040	-0.0023	-0.0021	-0.0027	-0.0045
-0.0083	-0.0110	-0.0144	-0.0189	-0.0243	-0.0290	-0.0332
-0.0384	-0.0440	-0.0505	-0.0585			
-0.0502	-0.0574	-0.0607	-0.0660	-0.0698	-0.0754	-0.0852
-0.0910	-0.0949	-0.1000	-0.1030	-0.1046	-0.1052	-0.1033
-0.0988	-0.0954	-0.0908	-0.0853	-0.0787	-0.0727	-0.0675
-0.0631	-0.0611	-0.0611	-0.0630			
58.662	14.733	80.428	0.5	1.		
-0.0880	-0.0788	-0.0752	-0.0705	-0.0672	-0.0629	-0.0557
-0.0511	-0.0473	-0.0434	-0.0404	-0.0386	-0.0375	-0.0375
-0.0398	-0.0420	-0.0446	-0.0479	-0.0522	-0.0555	-0.0586
-0.0624	-0.0672	-0.0735	-0.0832			
-0.0880	-0.0959	-0.0995	-0.1046	-0.1082	-0.1133	-0.1213
-0.1263	-0.1297	-0.1332	-0.1354	-0.1363	-0.1364	-0.1342
-0.1296	-0.1261	-0.1214	-0.1153	-0.1074	-0.1000	-0.0935
-0.0882	-0.0857	-0.0862	-0.0885			
63.248	17.779	81.748	0.5	1.		
-0.1135	-0.1056	-0.1021	-0.0978	-0.0947	-0.0896	-0.0821
-0.0772	-0.0734	-0.0695	-0.0651	-0.0632	-0.0617	-0.0612
-0.0625	-0.0638	-0.0652	-0.0678	-0.0709	-0.0735	-0.0758
-0.0791	-0.0836	-0.0900	-0.0997			
-0.1135	-0.1208	-0.1243	-0.1290	-0.1324	-0.1372	-0.1440
-0.1482	-0.1514	-0.1552	-0.1571	-0.1576	-0.1573	-0.1554
-0.1504	-0.1457	-0.1410	-0.1341	-0.1251	-0.1164	-0.1089
-0.1032	-0.1007	-0.1021	-0.1049			
65.614	20.094	82.885	0.5	1.		
-0.1282	-0.1203	-0.1165	-0.1115	-0.1083	-0.1035	-0.0960
-0.0908	-0.0870	-0.0820	-0.0785	-0.0763	-0.0749	-0.0737
-0.0738	-0.0746	-0.0756	-0.0775	-0.0808	-0.0830	-0.0853
-0.0887	-0.0933	-0.0999	-0.1100			
-0.1282	-0.1364	-0.1401	-0.1448	-0.1481	-0.1524	-0.1591
-0.1635	-0.1668	-0.1702	-0.1718	-0.1722	-0.1720	-0.1695
-0.1641	-0.1592	-0.1545	-0.1465	-0.1369	-0.1274	-0.1191
-0.1125	-0.1097	-0.1112	-0.1161			
67.198	22.083	83.864	0.5	1.		
-0.1399	-0.1296	-0.1258	-0.1219	-0.1179	-0.1137	-0.1069

Case No. 8 (Cont'd)

-0.1024	-0.0990	-0.0941	-0.0907	-0.0883	-0.0866	-0.0846
-0.0841	-0.0843	-0.0850	-0.0860	-0.0875	-0.0895	-0.0922
-0.0959	-0.1008	-0.1075	-0.1164			
-0.1399	-0.1494	-0.1532	-0.1579	-0.1612	-0.1658	-0.1729
-0.1773	-0.1804	-0.1841	-0.1858	-0.1863	-0.1860	-0.1832
-0.1777	-0.1736	-0.1678	-0.1593	-0.1476	-0.1370	-0.1284
-0.1221	-0.1188	-0.1201	-0.1285			
68.953	24.557	85.075	0.5	1.		
-0.1490	-0.1386	-0.1349	-0.1301	-0.1271	-0.1228	-0.1158
-0.1111	-0.1074	-0.1020	-0.0980	-0.0949	-0.0926	-0.0892
-0.0874	-0.0870	-0.0869	-0.0872	-0.0880	-0.0894	-0.0916
-0.0947	-0.0993	-0.1058	-0.1148			
-0.1490	-0.1581	-0.1618	-0.1665	-0.1696	-0.1741	-0.1808
-0.1849	-0.1876	-0.1906	-0.1917	-0.1916	-0.1905	-0.1865
-0.1798	-0.1751	-0.1688	-0.1598	-0.1477	-0.1367	-0.1278
-0.1212	-0.1178	-0.1190	-0.1275			
70.711	27.032	86.292	0.5	1.		
-0.1586	-0.1482	-0.1445	-0.1399	-0.1369	-0.1326	-0.1257
-0.1209	-0.1172	-0.1115	-0.1073	-0.1040	-0.1014	-0.0976
-0.0952	-0.0945	-0.0941	-0.0941	-0.0946	-0.0958	-0.0977
-0.1007	-0.1053	-0.1120	-0.1216			
-0.1586	-0.1675	-0.1711	-0.1757	-0.1788	-0.1831	-0.1897
-0.1936	-0.1961	-0.1989	-0.1997	-0.1993	-0.1980	-0.1934
-0.1863	-0.1814	-0.1749	-0.1658	-0.1535	-0.1424	-0.1335
-0.1270	-0.1237	-0.1251	-0.1341			
72.464	29.501	87.505	0.5	1.		
-0.1687	-0.1584	-0.1548	-0.1502	-0.1472	-0.1430	-0.1361
-0.1313	-0.1275	-0.1217	-0.1173	-0.1137	-0.1109	-0.1065
-0.1036	-0.1026	-0.1019	-0.1017	-0.1019	-0.1028	-0.1045
-0.1074	-0.1120	-0.1169	-0.1289			
-0.1687	-0.1774	-0.1810	-0.1855	-0.1885	-0.1927	-0.1991
-0.2028	-0.2052	-0.2077	-0.2082	-0.2075	-0.2060	-0.2010
-0.1934	-0.1883	-0.1816	-0.1725	-0.1601	-0.1489	-0.1399
-0.1334	-0.1302	-0.1319	-0.1412			
74.221	31.975	88.720	0.5	1.		
-0.1795	-0.1692	-0.1657	-0.1612	-0.1583	-0.1541	-0.1472
-0.1423	-0.1385	-0.1325	-0.1279	-0.1242	-0.1211	-0.1162
-0.1127	-0.1115	-0.1105	-0.1100	-0.1100	-0.1106	-0.1121
-0.1149	-0.1194	-0.1265	-0.1369			
-0.1795	-0.1880	-0.1915	-0.1959	-0.1988	-0.2030	-0.2092
-0.2127	-0.2150	-0.2172	-0.2174	-0.2165	-0.2147	-0.2092
-0.2013	-0.1960	-0.1892	-0.1799	-0.1674	-0.1562	-0.1472
-0.1407	-0.1376	-0.1394	-0.1490			
75.974	34.444	89.932	0.5	1.		
-0.1910	-0.1808	-0.1773	-0.1729	-0.1700	-0.1659	-0.1590
-0.1541	-0.1502	-0.1441	-0.1393	-0.1353	-0.1320	-0.1267
-0.1227	-0.1211	-0.1199	-0.1191	-0.1188	-0.1192	-0.1205
-0.1231	-0.1277	-0.1348	-0.1456			
-0.1910	-0.1993	-0.2028	-0.2070	-0.2099	-0.2140	-0.2200
-0.2234	-0.2255	-0.2274	-0.2274	-0.2262	-0.2242	-0.2183
-0.2099	-0.2044	-0.1975	-0.1881	-0.1756	-0.1643	-0.1553
-0.1488	-0.1458	-0.1478	-0.1576			
77.732	36.919	91.149	0.5	1.		
-0.2036	-0.1935	-0.1900	-0.1857	-0.1829	-0.1788	-0.1720
-0.1671	-0.1631	-0.1568	-0.1518	-0.1477	-0.1441	-0.1383

Case No. 8 (Cont'd)

-0.1338	-0.1320	-0.1306	-0.1295	-0.1290	-0.1291	-0.1302
-0.1327	-0.1371	-0.1444	-0.1554			
-0.2036	-0.2118	-0.2152	-0.2193	-0.2222	-0.2261	-0.2319
-0.2352	-0.2371	-0.2388	-0.2386	-0.2371	-0.2349	-0.2285
-0.2198	-0.2141	-0.2071	-0.1976	-0.1851	-0.1738	-0.1647
-0.1583	-0.1553	-0.1573	-0.1672			
81.056	41.599	93.447	0.5	1.		
-0.2297	-0.2196	-0.2163	-0.2121	-0.2094	-0.2055	-0.1986
-0.1937	-0.1896	-0.1831	-0.1778	-0.1733	-0.1694	-0.1627
-0.1574	-0.1551	-0.1532	-0.1517	-0.1506	-0.1503	-0.1510
-0.1532	-0.1575	-0.1648	-0.1762			
-0.2297	-0.2375	-0.2407	-0.2447	-0.2474	-0.2512	-0.2567
-0.2597	-0.2613	-0.2625	-0.2619	-0.2600	-0.2574	-0.2503
-0.2408	-0.2349	-0.2276	-0.2181	-0.2055	-0.1942	-0.1851
-0.1787	-0.1757	-0.1778	-0.1877			
82.996	44.331	94.789	0.5	1.		
-0.2462	-0.2363	-0.2330	-0.2290	-0.2263	-0.2224	-0.2156
-0.2106	-0.2065	-0.1998	-0.1944	-0.1897	-0.1856	-0.1785
-0.1727	-0.1702	-0.1680	-0.1662	-0.1649	-0.1644	-0.1649
-0.1669	-0.1710	-0.1783	-0.1897			
-0.2462	-0.2538	-0.2570	-0.2609	-0.2636	-0.2672	-0.2725
-0.2753	-0.2769	-0.2778	-0.2769	-0.2749	-0.2720	-0.2645
-0.2547	-0.2486	-0.2412	-0.2317	-0.2191	-0.2078	-0.1976
-0.1923	-0.1892	-0.1913	-0.2012			
86.506	49.275	97.217	0.5	1.		
-0.2793	-0.2696	-0.2664	-0.2625	-0.2600	-0.2562	-0.2495
-0.2445	-0.2403	-0.2334	-0.2277	-0.2227	-0.2183	-0.2105
-0.2039	-0.2010	-0.1984	-0.1962	-0.1945	-0.1935	-0.1936
-0.1952	-0.1990	-0.2061	-0.2174			
-0.2793	-0.2866	-0.2896	-0.2934	-0.2959	-0.2994	-0.3044
-0.3069	-0.3082	-0.3087	-0.3075	-0.3051	-0.3019	-0.2937
-0.2833	-0.2770	-0.2694	-0.2598	-0.2474	-0.2360	-0.2270
-0.2204	-0.2173	-0.2191	-0.2286			
88.259	51.744	98.429	0.5	1.		
-0.2981	-0.2885	-0.2854	-0.2816	-0.2791	-0.2754	-0.2687
-0.2637	-0.2596	-0.2526	-0.2468	-0.2417	-0.2371	-0.2290
-0.2220	-0.2190	-0.2162	-0.2138	-0.2118	-0.2107	-0.2105
-0.2119	-0.2156	-0.2224	-0.2336			
-0.2981	-0.3032	-0.3083	-0.3119	-0.3144	-0.3178	-0.3226
-0.3251	-0.3263	-0.3266	-0.3251	-0.3226	-0.3192	-0.3107
-0.3001	-0.2937	-0.2861	-0.2765	-0.2641	-0.2528	-0.2437
-0.2371	-0.2338	-0.2355	-0.2447			
92.099	57.150	101.085	0.5	0.		
-3.	0.	136.2	0.	0.	0.	0.4
NASA TM X-3431 TRANSPORT FUSELAGE				QUICK GEOMETRY MODEL		
1.						
1.	2.	NOSE TO TAIL				
BCDYLO	ELLI	EDYBCL	EDYMHB	BDYLSCP		
BODYHI	ELI.I	EDYMHB	EDYTCL	BDYUSCP		
1.						
1.	1.	0.0	136.2			
6.	6.					
5.	ZEDYBCL					
ELLX	0.0	7.0	30.0	1.8	0.0	2.3
LINE	30.0	1.8	92.0	1.3		

Case No. 8 (Cont'd)

CUBI	92.0	1.3	121.0	3.5	103.0	1.2
CUBI	121.0	3.5	132.0	4.0	125.0	4.0
LINE	132.0	4.0	136.2	4.0		
6.	ZEDYTCL					
ELIX	0.0	7.0	45.0	15.25	0.	15.25
LINE	45.0	15.25	57.0	15.0		
LINE	57.0	15.0	66.0	14.72		
CUBI	66.0	14.72	95.0	13.85	88.5	14.35
CUBI	95.0	13.85	106.0	13.40	101.0	13.40
LINE	106.0	13.40	136.2	13.40		
1.	YEDYTCL					
LINE	0.0	0.0	136.2	0.0		
6.	ZEDYMHB					
CUBI	0.0	7.0	19.0	7.9	8.5	7.9
CUBI	19.0	7.9	32.0	6.8	29.0	7.9
CUBI	32.0	6.8	50.0	4.0	40.0	4.0
LINE	50.0	4.0	78.0	4.0		
CUBI	78.0	4.0	86.0	4.9	83.0	4.0
CUBI	86.0	4.9	136.2	9.4	92.0	6.9
5.	YEDYMHB					
ELIX	0.	0.	49.0	7.55	0.	7.55
CUBI	49.0	7.55	58.0	7.25	55.0	7.55
CUBI	58.0	7.25	80.0	7.10	68.0	5.40
CUBI	80.0	7.10	91.0	7.45	86.0	7.45
CUBI	91.0	7.45	136.2	2.8	113.0	7.45
2.	ZMAPAXIS					
CUBI	0.0	7.0	19.0	7.9	8.5	7.9
LINE	19.0	7.9	136.2	7.9		
	YMAPAXIS	YBCYTCL				
	YEDYBCL	YBDYTCL				
	YEDYLSCP	YBDYMHB				
	YEDYUSCP	YBDYMHB				
	ZEDYLSCP	ZBDYBCL				
	ZEDYUSCP	ZBCYTCL				

OUTPUT DATA (PRINT AND PLOT) FORMAT

Printed and plotted output data is provided. Since a typical print or plot sequence is lengthy, only a brief description of each type of output will be provided here. Note that samples of the plotted output can be found in the results and geometry verification sections of this report.

Printed Output

The printed output can be divided into three distinct sections.

- Section I Input Data Listing/Geometry and Grid System Verification
- Section II Relaxation Solution Convergence History
- Section III Computed Velocities, Pressures, Forces, Moments, Reference Lengths and Areas

Within each section, the output data will be printed in the following sequence.

Section I

- Input Data Listing
- Case Flow Condition
- Nominal Extent of Fine Embedded Grid Systems
- Quick-Geometry Model Error Diagnostic Information (BKOD = ± 3 only)
- Configuration Position in Global Crude Grid System
- Body Crude/Fine Grid Limiters
- Global Crude Grid Coordinates
- Fine Embedded Wing Grid Coordinates
- Fine Embedded Body Grid Coordinates

Section II

Phase 1 (Global Crude Grid Solution)

The following information is printed for each crude grid iteration.

- A {
- Iteration Count
 - Maximum Correction to the Flow Field Potential ($\Delta \varphi_{\text{MAX}}$)
 - Grid Position of $\Delta \varphi_{\text{MAX}}$
 - Wing Spanwise Circulation (Γ) Distribution

The following information is printed at the end of the Global Crude Grid Solution.

- B {
- Section Mach Chart (0 indicates subsonic flow)
(1 indicates supersonic flow)
(8 indicates wing section surface)
(7 indicates wake surface)
 - Span row number/ η -position/local chord length, chord position, pressure coefficient, disturbance velocity, section circulation (Γ).

Phase 2 (Crude/Fine Grid Interactions)

The following information is printed for each crude/fine grid interaction cycle.

- Phase 1 (A) Output for Fine Embedded Wing Grid System
- Phase 1 (A) Output for Fine Embedded Body Grid System (for BKOD > 0 only)
- Phase 1 (A) Output for Global Crude Grid System
- Wing Spanwise Circulation (Γ) Distribution

For viscous interaction cases, the following information is printed every 20th cycle.

- Wing Upper/Lower Surface Boundary Layer Separation Point (x/c)
- Boundary Layer δ^* Slope Added to Wing Boundary Conditions.

Section III

The following information is printed at the end of the solution process.

- Phase 1 (B) Output for Wing Embedded Fine Grid System
- For (VISM0D = 2, 3) Wing Upper/Lower Surface Boundary Layer Separation Point (x/c)
- Wing Section $C_{l_{\omega}}$, $C_{m_{\omega}}$, $C_{d_{\omega}}$, $C_{f_{\omega}}$
Note: $C_{m_{\omega}}$ is section moment about local quarter chord position.
- Spanwise Load, Moment, Drag Distributions
- Wing Exposed Area, Total Area, Aspect Ratio, Taper Ratio, Mean Aerodynamic Chord, Average Chord, X-position about which Moments are computed
- Total Wing $C_{L_{WING}}$, $C_{M_{WING}}$, $C_{D_{WING}}$

- Wing Pressure Drag $C_{D_{P(w)}}$
- Wing Friction Drag $C_{F_{WING}}$
- Body Grid Mach Chart
- Body Angular Cut Pressure/Velocity Distribution
- Body Longitudinal Load and Drag Distribution
- Body Length, Wetted Area, Projected Area, Max. Cross-sectional Area, Reynolds Number based on body length
- Total Body $C_{L_{BODY}}$, $C_{M_{BODY}}$, $C_{D_{P(b)}}$
- Body Pressure Drag $C_{D_{P(b)}}$
- Body Friction Drag C_{F_B}
- Total Configuration C_L , C_M , C_D
- Wing-Body Wave Drag $C_{D_{WAVE}}$
- Wing-Body Friction Drag C_F
- Wing-Body Lift-Induced Drag C_{D_I}
- Wing-Body Spanload Efficiency Factor (E)

Plotted Output

The plot output can be divided into two separate sections.

Section I (Input Geometry Verification)

- Title/Case/Flow Condition Label
- Body Cross-Sections
- Input Wing Sections
- Configuration Planview
- Configuration Head-On View

Section II (Computed Results)

- Superimposed wing pressure distributions (upper/lower surface) with total wing C_L , C_M , C_D label.
- Wing planform with section shapes at computed span stations.

- Detailed wing section pressure distributions with section C_l , C_m , C_d label.
- Detailed body angular cut pressure distributions.
- Body longitudinal load plot with body C_{L_B} , C_{M_B} , C_{D_B} and wing-body C_L , C_M , C_D label.
- Wing-body spanload plot with span efficiency, lift-induced drag, wave drag, friction drag label.

INPUT GEOMETRY VERIFICATION

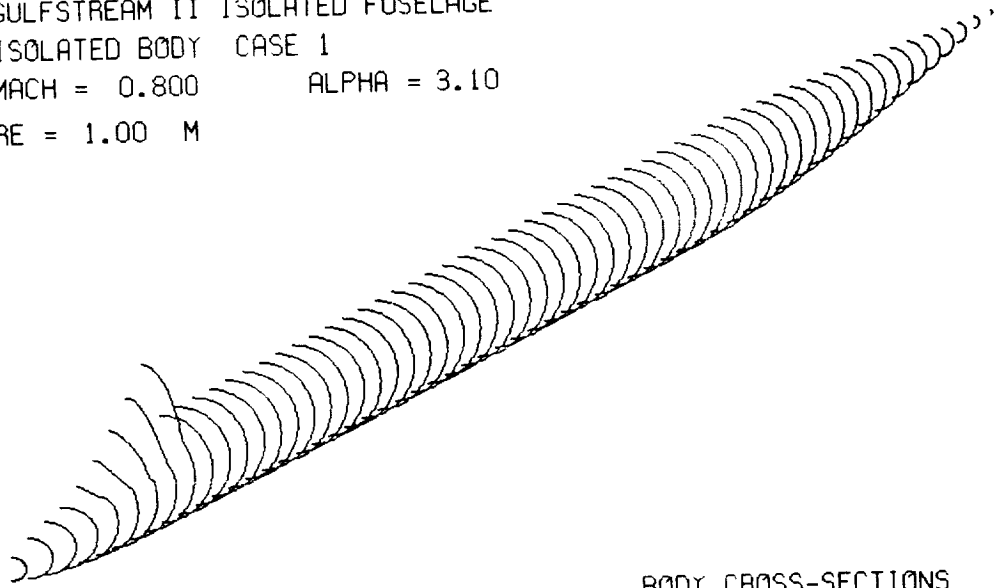
Coding for the graphical inspection of input wing and body geometry has been included. Since the program requires considerable computer time and core storage to operate and some facility budgets may not provide for a number of error-filled submittals, it is recommended that the geometry verification mode of operation be used before submitting for a complete and expensive relaxation solution. The graphic output coupled with printed output for geometry and grid systems should be sufficient to diagnose user input errors. In particular, it has been found advantageous to make the geometry check and perform a single crude and a single fine grid iteration (very cheap) to check code flow before a complete analysis is performed.

The body cross-section array is first to be plotted after the case title and flow conditions are listed (see Figure A-1). In this case, an error in specifying a Z-coordinate of the canopy top centerline is apparent. In Figure A-2, an error in specifying a Y-coordinate of the windshield base is illustrated. Finally, Figure A-3 illustrates the corrected and final shape of the fuselage to be analyzed.

The defining wing chord sections are displayed after the body geometry (see Figure A-4). Each is blown up to a ten inch chord so errors in coordinates will become visible. It is important to note that there is no mapping involved in the present method, thus, no coordinate smoothing or manipulation is employed. As a result, what you input is what you get. Irregularities in input coordinates will cause oscillations in computed pressure distributions.

A configuration plan-view will follow the wing section figures. This should be used to insure that the wing planform is properly defined and its placement on the fuselage is correct (see Figure A-5). Finally, a head-on view is plotted (see Figure A-6). Once again, check to see that the wing and body are indeed attached.

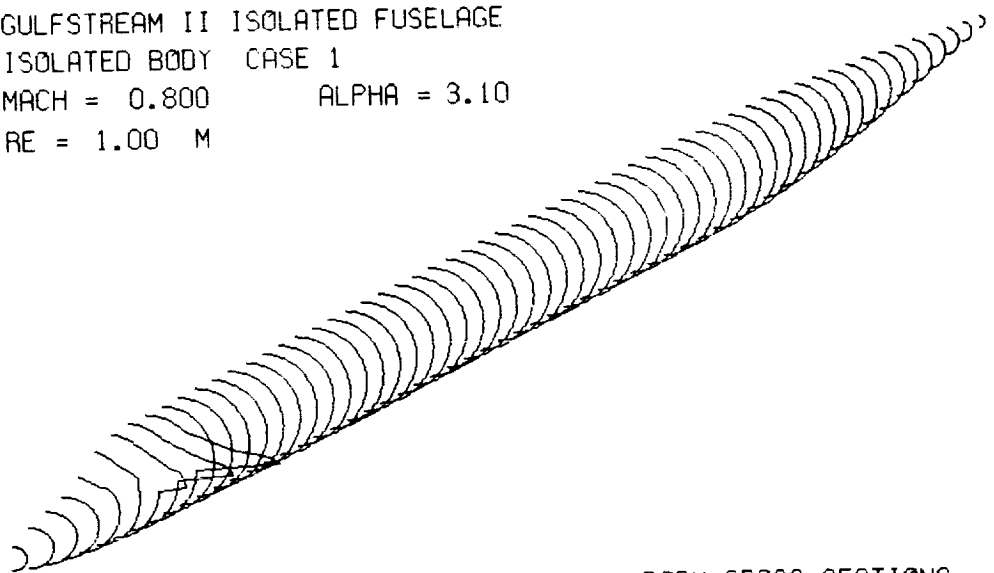
GULFSTREAM II ISOLATED FUSELAGE
ISOLATED BODY CASE 1
MACH = 0.800 ALPHA = 3.10
RE = 1.00 M



BODY CROSS-SECTIONS

Figure A-1. Sample Input Geometry Verification Plot with Error in Z-Coordinate of Canopy Definition

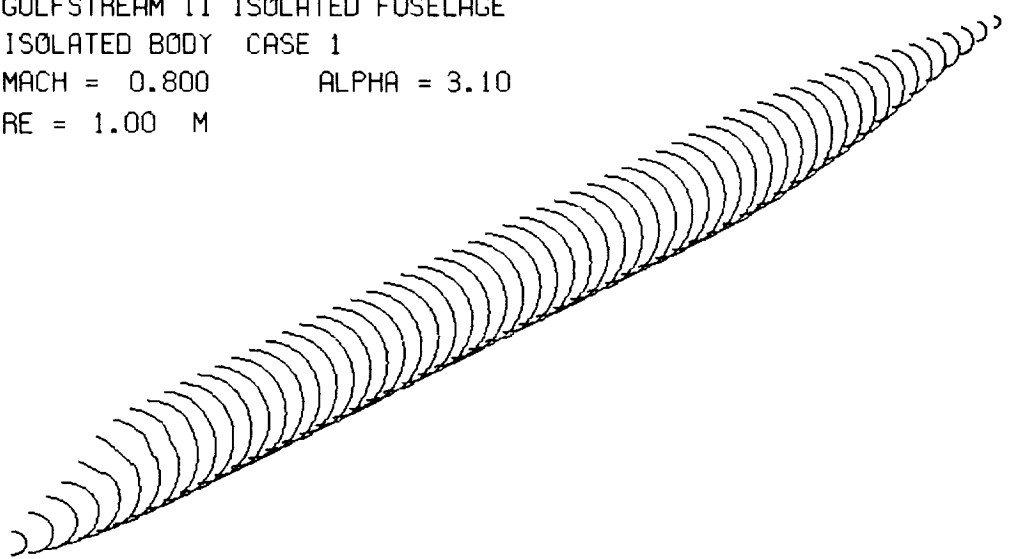
GULFSTREAM II ISOLATED FUSELAGE
ISOLATED BODY CASE 1
MACH = 0.800 ALPHA = 3.10
RE = 1.00 M



BODY CROSS-SECTIONS

Figure A-2. Sample Input Geometry Verification Plot with Error in Y-Coordinate of Canopy Definition

GULFSTREAM II ISOLATED FUSELAGE
ISOLATED BODY CASE 1
MACH = 0.800 ALPHA = 3.10
RE = 1.00 M



BODY CROSS-SECTIONS

Figure A-3. Sample Input Geometry Verification Plot for Fuselage

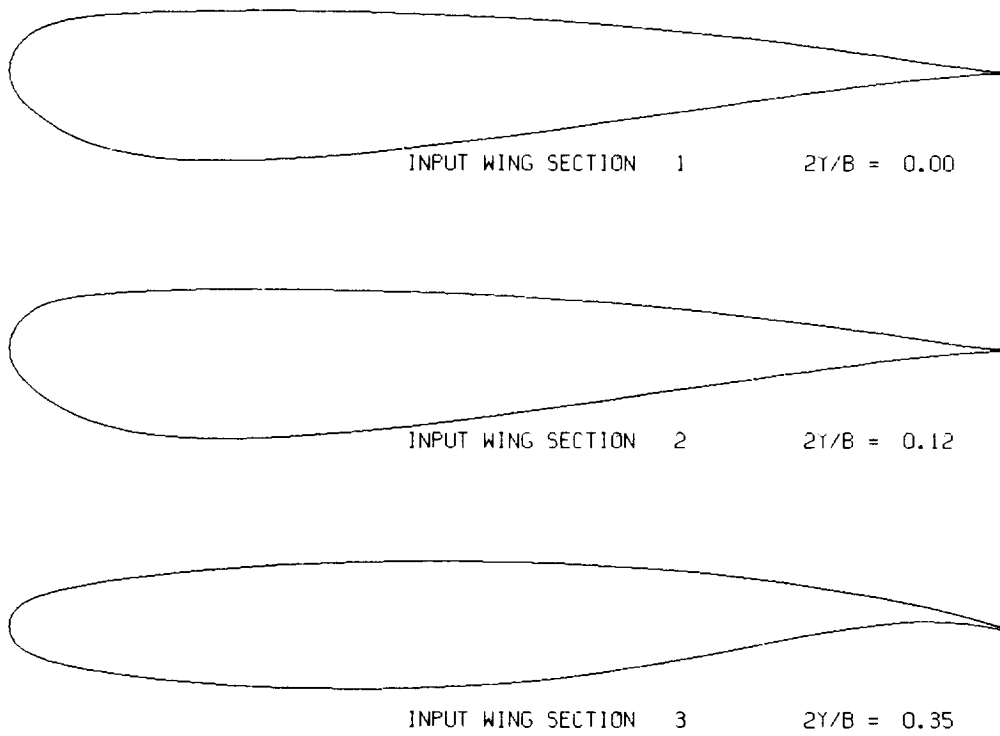


Figure A-4. Sample Input Geometry Verification Plot for Wing Sections

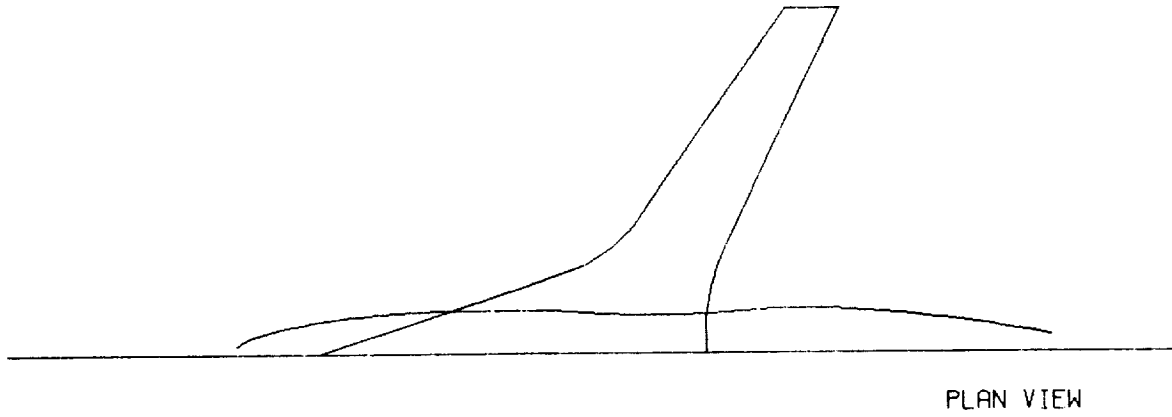


Figure A-5. Sample Input Geometry Verification Plot, Plan View

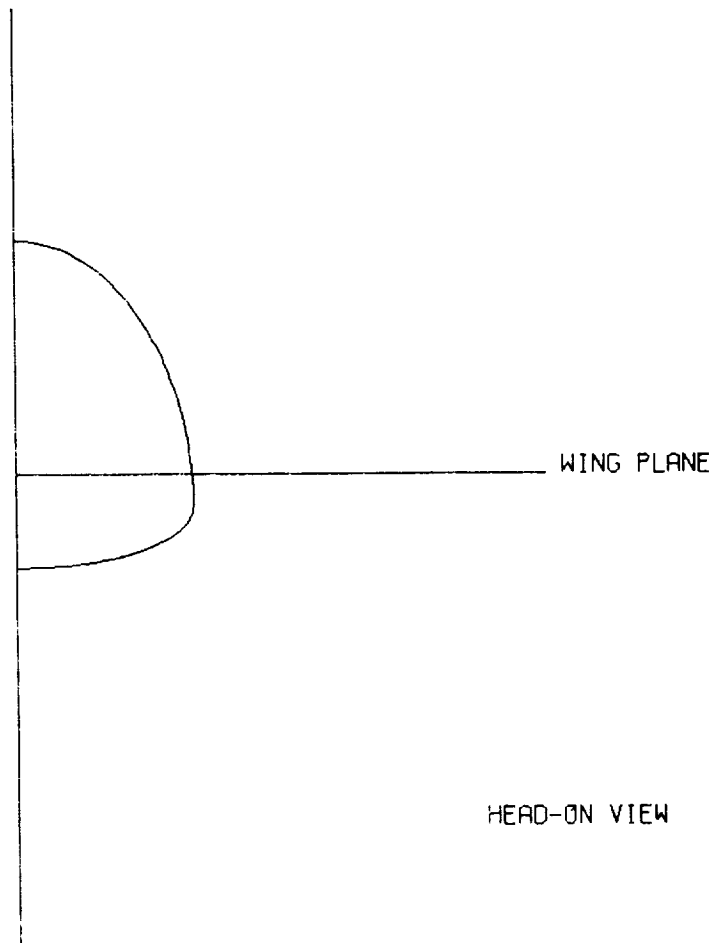
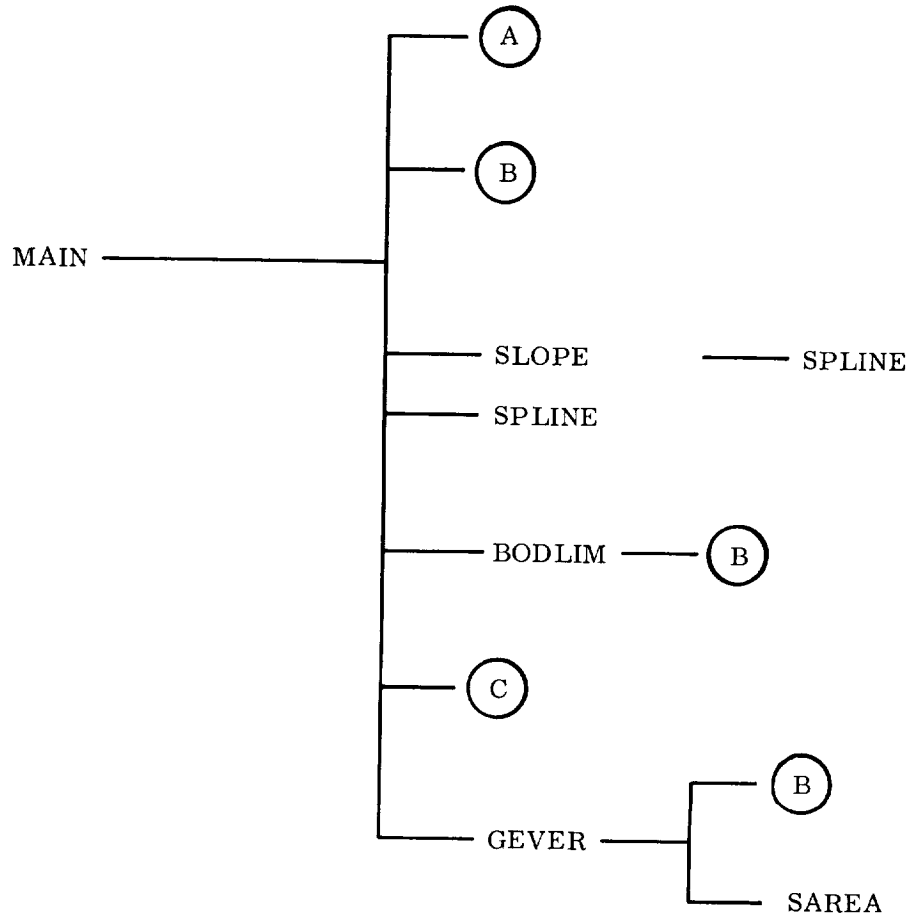


Figure A-6. Sample Input Geometry Verification Plot, Head-On View

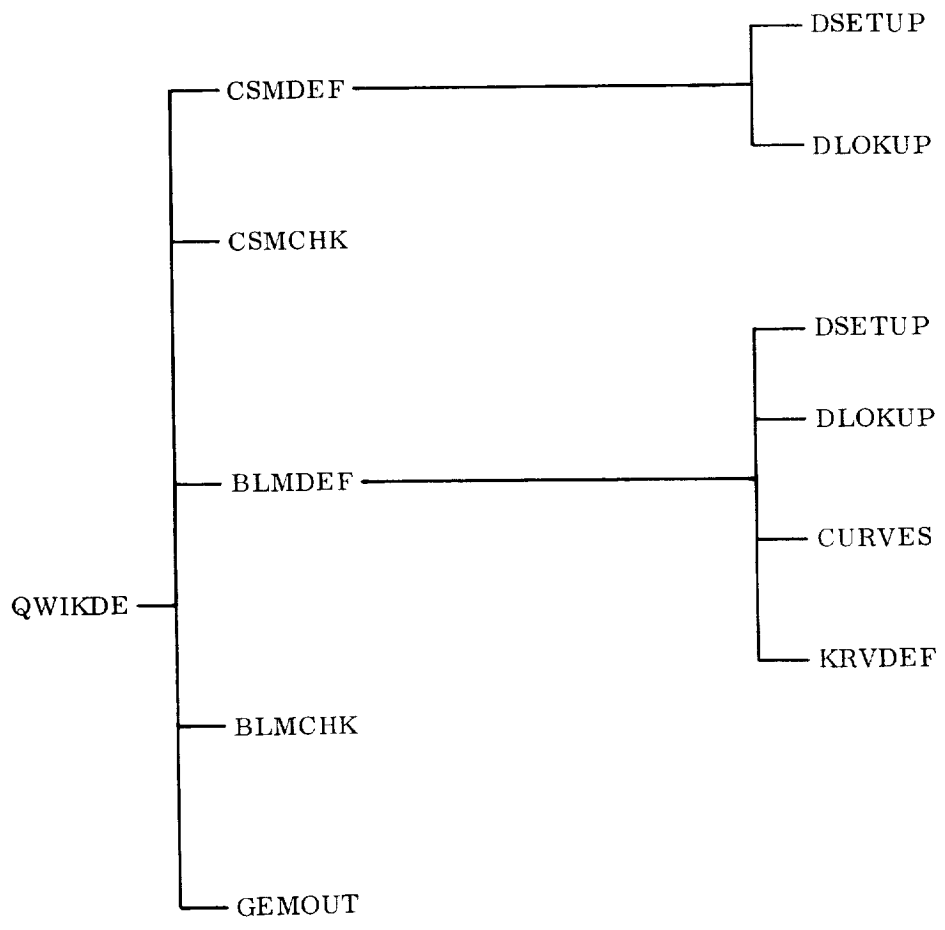
SUBROUTINE CALL SEQUENCE



NOTE:

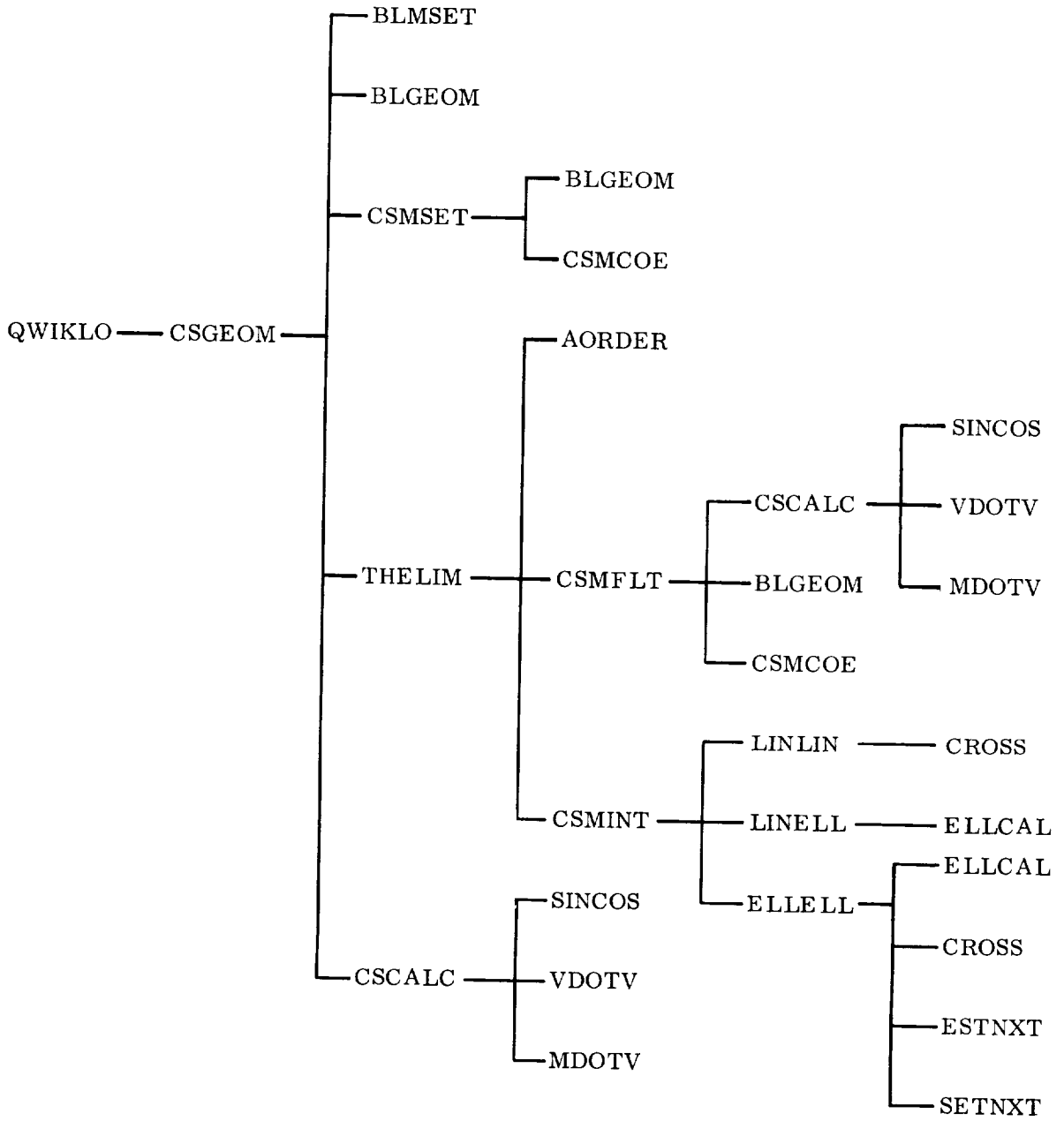
- (A) Fuselage Geometry Definition
- (B) Fuselage Geometry Interrogation
- (C) Relaxation/Boundary Layer Routines

SUBROUTINE CALL SEQUENCE (A)

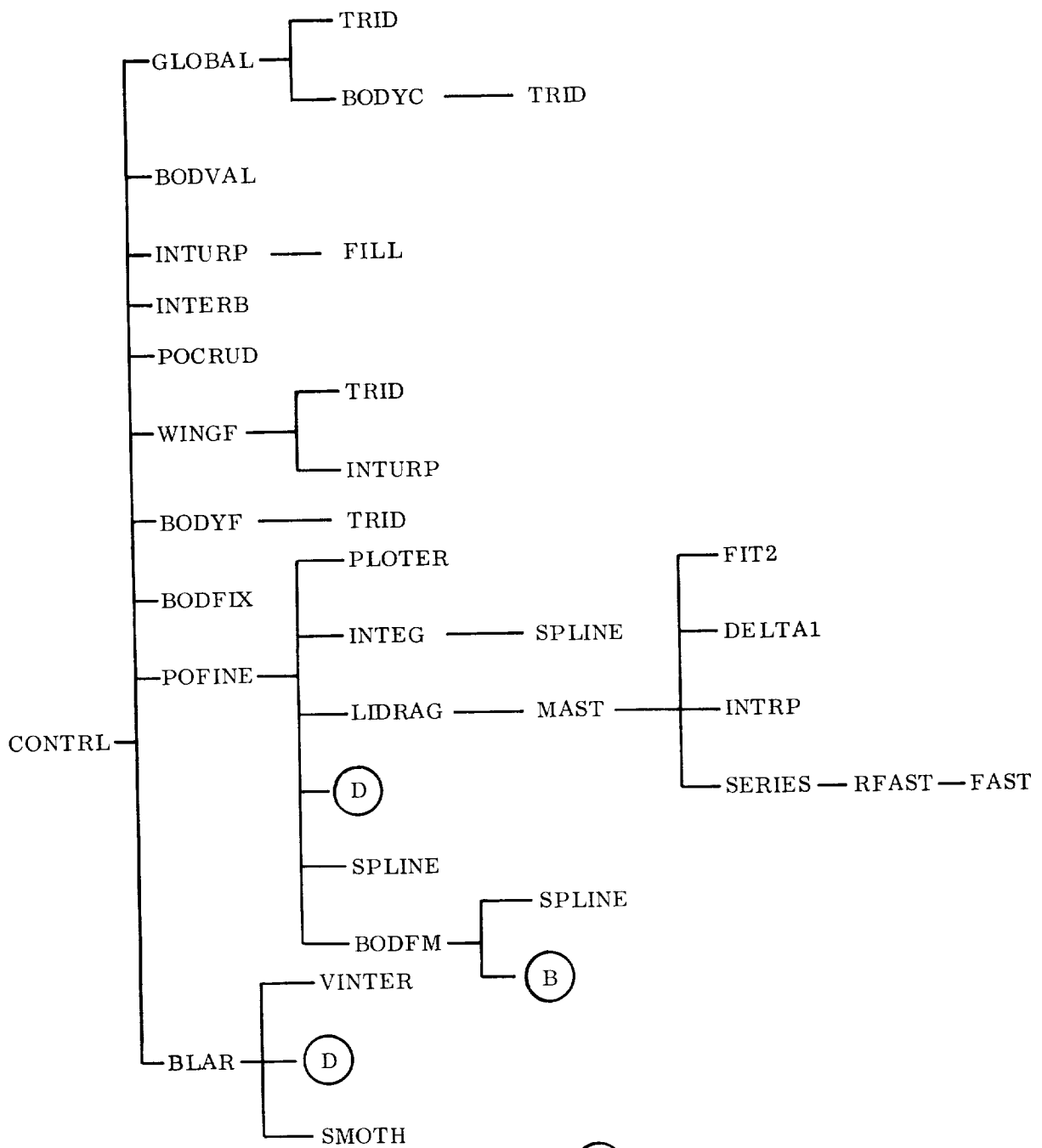


SUBROUTINE CALL SEQUENCE

(B)

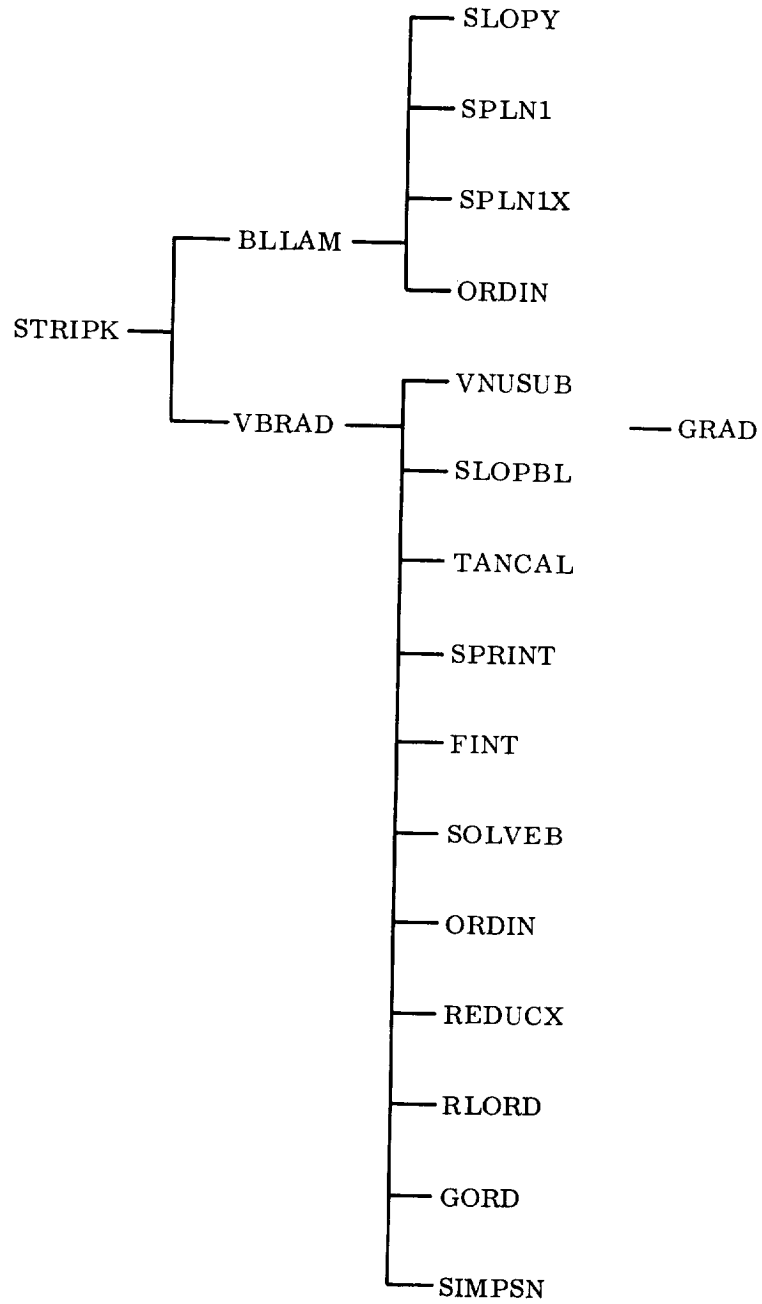


SUBROUTINE CALL SEQUENCE (C)



NOTE: (D) BOUNDARY LAYER ROUTINES

SUBROUTINE CALL SEQUENCE (D)



1

SUBROUTINE DESCRIPTION

AORDER	Orders a set of numbers by permutation index.
BLAR	Main control routine for laminar and turbulent modified chordwise boundary layer calculation. Computes boundary layer displacement thickness (δ^*) slope for viscous/inviscid interaction mode of operation.
BLGEOM	Assigns body line model values and derivatives to control point coordinates.
BLLAM	Computes Thwaites laminar boundary layer with Rott and Crabtree compressibility modification.
BLMCHK	Correlates and checks the input data deck and the indices for the generated body line math models.
BLMDEF	Defines body line models from the input data.
BLMSET	Controls the determination values and first and second derivatives for all body line models at a given x-station.
BODFIX	Computes potentials on fixed wing/wake surface in body fine grid given solution in fine wing grid and global crude grid.
BODFM	Computes integrated body force and moment coefficients.
BODLIM	Computes J and K limiters for body boundary in both crude and fine grid systems.
BODVAL	Computes body boundary point potential values.
BODYC	Finite difference approximations and relaxation solution for body boundary in crude grid.
BODYF	Finite difference approximations and relaxation solution for fine body grid.
CONTRL	Main control routine for relaxation solution of governing equation, interpolation, boundary layer analysis and printed/plotted output.

CROSS Solves for the interaction of two lines in a plane.

CSCALC Computes radial position and derivatives for specified cross-section model, arc, and θ' .

CSGEOM Is the main subroutine in the look-up portion of the QUICK system. It is called to establish $r' = f(\theta', x)$. It calls appropriate subroutines to evaluate body line values and construct cross-section geometry at a given x-station. It is used for all geometry model interrogation.

CSMCHK Correlates and checks the input data deck and the indices for the cross-sectional math model.

CSMCOE Composes the equations which are to define the cross-section geometry at a given station.

CSMDEF Logically defines the cross-section models from the input data.

CSMFLT Creates control point definitions to permit the insertion of a smooth fillet between cross-sectional arcs.

CSMINT Locates user specified intersections between cross-sectional arcs and adjusts their use-theta limits.

CSMSET Sets up the control point coordinate arrays used to define the cross-section geometry at a specified x-station.

CURVES Calculates values and first and second derivatives for individual curve fits.

DELTA1 Interpolation routine for wing spanload.

DLOKUP Is a simple dictionary look-up routine. It assigns an index to match an input name to a codeword list, but is not capable of adding new items to that list.

DSETUP Is an adapting dictionary look-up routine. New items are added to a codeword list, an index (counter) is returned for the codeword, and an indicator (INEW) is set equal to 1 when a new item is encountered.

ELLCAL Set up for ellipse.

ELLELL Calculates intersection of two ellipses.

ESTNXT	Estimates non-linear root by modified inverse quadratic.
FAST	Fast Fourier transform of complex data.
FILL	Performs interpolation controlled by INTURP.
FINT	Simultaneous triple interpolation.
FIT2	Determines cubic spline fit coefficients for input spanload distribution.
GEMOUT	Ensures that all body lines required by a cross-sectional model are defined for the range of that model.
GEVER	Controls geometry verification plotting.
GLOBAL	Finite difference approximations and relaxation solution for global crude grid.
GORD	Bradshaw's G function.
GRAD	Slope of a function at its tabulated points.
INTEG	Integrates wing load distributions for lift, moment and drag coefficients.
INTERB	Interpolation routine for body fine/global crude grid communication.
INTRP	Converts input spanload distribution to a fine over spaced distribution.
INTURP	Controls interpolation for filling fine mesh points using crude grid potential values. Updates crude mesh given fine solution. Updates fine mesh given crude solution.
KRVDEF	Calculates coefficients for the various curve fits associated with body line math models.
LIDRAG	Main control routine for computing lift induced drag efficiency "E" using a Fourier analysis.
LINELL	Solves for the intersection of a line and an ellipse.
LINLIN	Solves for intersection of two lines.
MAIN	Reads all input data except for fuselage math model. Sets up arrays and storage areas. Sets up all crude and fine coordinate systems.
MAST	Controls cubic spline fit for interpolation of input spanload distribution.

MDOTV	Performs matrix multiplication of a vector.
ORDIN	Linear interpolation.
PLOTER	Controls all graphic output (except input geometry verification).
POCRUD	Prints results in global crude grid.
POFINE	Prints results in wing and body fine grid arrays. Integrates wing pressure distributions. Computes body friction drag.
QWIKDE	Main control routine for Quick-Geometry definition and check out.
QWIKLO	Main control routine for interrogation of Quick-Geometry math model.
REDUCX	Performs interpolation to new grid.
RFAST	Fast Fourier transform of real data.
RLORD	Bradshaw's L function.
SAREA	Computes body surface area given an array of cross-sections.
SERIES	Determines Fourier series coefficients.
SETNXT	Reorders points for non-linear root finder.
SIMPSN	Simpson's rule integration.
SINCOS	Adjusts input interrogation angles for top and bottom dead center.
SLOPBL	Slope of a tabulated function at an arbitrary point.
SLOPE	Computes boundary conditions for wing surface and axisymmetric bodies.
SLOPY	Computes wing surface slopes.
SMOTH	Function for smoothing an array of values.
SOLVEB	Solution of two simultaneous linear algebraic equations.
SPLINE	Computes a cubic spline through a set of points.
SPLN1	Computes continuous derivatives interpolation by means of a cubic fit.
SPLN1X	Entry for special cases requiring extrapolation beyond ends of X and Y tables.
SPRINT	Prints output of profile results.

TANCAL	Computes characteristic angles for use in the solution (equation 21 of Bradshaw and Ferriss).
THELIM	Creates and controls use-theta arrays to establish continuity in the cross-sectional model.
TRID	Solves tri-diagonal matrix.
VBRAD	Computes Bradshaw compressible 2-D turbulent boundary layer simulating 3-D boundary layer on infinite yawed wing by Nash-Tseng modified chord technique.
VDTV	Computes a vector dot product.
VINTER	Performs cubic δ^* fit for separated boundary layer in wing section cove regions.
VNUSUB	Computes the Nash effective viscosity.
WINGF	Finite difference approximations and relaxation solution for wing fine grid.

|

KEY VARIABLE DESCRIPTIONS

This description of key program variables and constants which are located in several common blocks will be useful in understanding flow logic.

<u>VARIABLE</u>	<u>DESCRIPTION</u>
AK	The value $1-M^2$.
ALAM	Wing taper ratio (λ).
ALPHA	Angle-of-attack (radians).
AMAC	Wing mean aerodynamic chord (MAC).
AMACH	Mach number.
AM2	The value M^2 .
AOA	Angle-of-attack (degrees).
AR	Wing aspect ratio (R).
BAREA	Body wetted area.
BCF	Body skin friction coefficient.
BCL	Wing crude grid lower boundary slopes.
BCLF	Wing fine grid lower boundary slopes.
BCU	Wing crude grid upper boundary slopes.
BCUF	Wing fine grid upper boundary slopes.
BNOSE	X-coordinate of body nose.
BODCD	Body (integrated) drag coefficient.
BODCL	Body (integrated) lift coefficient.
BODCM	Body (integrated) moment coefficient.
BPAREA	Body projected area.

<u>VARIABLE</u>	<u>DESCRIPTION</u>
BS	Body plot scaling coefficient.
BTAIL	X-coordinate of body tail.
CA	Global crude grid stretching coefficient (ξ_x).
CAV	Wing average chord (C_{AV}).
CB	Global crude grid stretching coefficient (ξ_{xx}).
CC	Global crude grid stretching coefficient (η_y).
CD	Global crude grid stretching coefficient (η_{yy}).
CDI	Lift induced drag coefficient.
CDINT	Wing section integrated drag.
CE	Global crude grid stretching coefficient (ξ_z).
CF	Global crude grid stretching coefficient (ξ_{zz}).
CFINT	Integrated wing section friction coefficient.
CIR	Wing circulation (Γ).
CLINT	Wing section integrated lift.
CMINT	Wing section integrated moment.
CMLOC	Wing section integrated moment about local quarter chord.
CPL	Wing lower surface pressure coefficient.
CPU	Wing upper surface pressure coefficient.
CSCUT	Body x-station for cross-sectional cut.
DELSL	Wing boundary layer slopes for section lower surface.
DELSU	Wing boundary layer slopes for section upper surface.
DETA	Global crude grid mesh spacing in η direction.

<u>VARIABLE</u>	<u>DESCRIPTION</u>
DIM	Configuration length for non-dimensionalizing maximum potential updates.
DRDXC	Axisymmetric body slope distribution in crude grid.
DRDXF	Axisymmetric body slope distribution in fine grid.
DXB	Fine body grid mesh spacing in X direction.
DXI	Global crude grid mesh spacing in ξ direction.
DXW	Fine wing grid mesh spacing in X direction.
DYB	Fine body grid mesh spacing in Y direction.
DYW	Fine wing grid mesh spacing in Y direction.
DZB	Fine body grid mesh spacing in Z direction.
DZETA	Global crude grid mesh spacing in ζ direction.
DZW	Fine wing grid mesh spacing in Z direction.
E	Wing spanload efficiency.
ETA	η coordinates for global crude grid (transformed space).
G	The value $(\gamma + 1) M^2$.
H	The value $(\gamma - 1) M^2$.
IBGI	Crude grid I value of body grid inner overlap region (forward).
IBGL	Crude grid I value of body grid inner overlap region (aft).
IL	Crude grid wing leading edge I values.
ILEF	Wing fine grid leading edge I value.
IMACH	Code for subsonic (0) or supersonic (1) flow at a grid point.
IMAXB	Maximum number of fine body grid points in X direction.
IMAX	Maximum number of crude grid points in X direction.
IMAXW	Maximum number of fine wing grid points in X direction.

<u>VARIABLE</u>	<u>DESCRIPTION</u>
INOSE	Fine body grid I value at body nose .
INOSEC	Crude grid I value at body nose .
IT	Crude grid wing trailing edge I values .
ITAIL	Fine body grid I value at body tail .
ITAILC	Crude grid I value at body tail .
ITEF	Wing fine grid trailing edge I value .
ITER	Iteration count .
JBG	Crude grid J value of body grid inner overlap region (side) .
JMAX	Maximum number of crude grid points in Y direction .
JMAXB	Maximum number of fine body grid points in Y direction .
JROOT	Grid J value at wing root .
JSD	Fine body grid J value at first influence of body boundary points .
JSDC	Crude grid J value first influenced by body boundary point .
JTIP	Grid J value at wing tip .
KBB	Fine body grid K value at wing plane .
KBOD	Code for body in crude grid (0) or fine embedded grid (1) .
KBC	Crude grid K value at wing plane .
KBGL	Crude grid K value of body grid inner overlap region (lower) .
KBGU	Crude grid K value of body grid inner overlap region (upper) .
KBW	Fine wing grid K value at wing plane .
KLOC	Crude grid K limiters for body surface (lower) .
KLOF	Fine grid K limiters for body surface (lower) .
KMAX	Maximum number of crude grid points in Z direction .

<u>VARIABLE</u>	<u>DESCRIPTION</u>
KMAXB	Maximum number of fine body grid points in Z direction.
KMAXW	Maximum number of fine wing grid points in Z direction.
KODB	Body option code . . . cylinder, axisymmetric, arbitrary body (input as BKOD).
KUPC	Crude grid K limiters for body surface (upper).
KUPF	Fine grid K limiters for body surface (upper).
MAXIT	Maximum number of initial crude grid iterations (input as AXIT).
MAXITF	Maximum number of crude/fine grid cycles (input as AXITF).
MODV	Mode of operation for viscous effects (input as VISMOD).
NCASE	Case description . . . wing, body or wing-body case (input as CASE).
NINB	Number of ordinates defining axisymmetric body shape (input as BNIN).
NINW	Number of ordinates defining each wing section (input as ANIN).
NOSEB	Blunt/sharp nose body code (for spline fit).
NOSEW	Blunt/sharp nose wing code (for spline fit).
NPOA	Number of fine grid points between leading and trailing edge of each wing section.
NPOB	Number of fine body grid points between nose and tail of body.
NSECT	Number of defining wing sections (input as ASECT).
NTC	Number of points representing body cross-sections in crude grid.
NTF	Number of points representing body cross-sections in fine body grid.
NTOTB	Total number of fine body grid points in single X-Z plane.

<u>VARIABLE</u>	<u>DESCRIPTION</u>
NTOTAL	Total number of crude grid points in single X-Z plane.
NTOTW	Total number of fine wing grid points in single X-Z plane.
NWPO	Code for print out of crude grid results for diagnostic purposes (input as WPO).
PBL	Fine body grid wing/wake lower surface potentials.
PC1	Global crude grid potential (ψ) arrays (Note: Only three planes are in core at one time.)
PC2	Global crude grid potential (ψ) arrays (Note: Only three planes are in core at one time.)
PC3	Global crude grid potential (ψ) arrays (Note: Only three planes are in core at one time.)
PCL	Crude grid wing/wake lower surface potentials.
PF1	Fine embedded wing and body potential arrays. (Note: Only three planes are in core at one time).
PF2	Fine embedded wing and body potential arrays. (Note: Only three planes are in core at one time).
PF3	Fine embedded wing and body potential arrays. (Note: Only three planes are in core at one time).
PFL	Fine wing grid surface potentials, lower surface
PI	π
RADIUS	Radius for body cylinder option.
RAVC	Crude grid average body radius for boundary condition calculation.
RAVF	Fine grid average body radius for boundary condition calculation.
RC	Axisymmetric body radius distribution in crude grid.
RE	Freestream Reynolds number.
RF	Axisymmetric body radius distribution in fine grid.

<u>VARIABLE</u>	<u>DESCRIPTION</u>
RIN	Input R ordinates defining axisymmetric body.
RMAX	Body maximum radius for computational body surface.
SDD	Wing spanwise drag coefficient $\frac{CC_d}{C_{AV}}$.
SEXP	Wing exposed area.
SFD	Wing spanwise friction coefficient $\frac{CC_f}{C_{AV}}$.
SGRAD	Body side slope at wing-body juncture.
SLD	Wing span load coefficient $\frac{CC_l}{C_{AV}}$.
SMD	Wing spanwise moment coefficient $\frac{CC_m}{C_{AV}}$.
THETC	Body crude grid angular cuts.
THETF	Body fine grid angular cuts.
TITLE	Case title for identifying graphic and printed output.
TSLOC	Wing local sweep angle at wing fine grid boundary points.
TWIST	Wing twist (incidence) distribution.
W	Relaxation factor ω .
WAREA	Wing area S_W .
WCD	Wing drag coefficient.
WCF	Wing friction drag coefficient.
WCL	Wing lift coefficient.
WCM	Wing moment coefficient.

<u>VARIABLE</u>	<u>DESCRIPTION</u>
WCORD	Wing section local chord length.
WS	Wing plot scaling coefficient (input as SCALW).
X	X coordinate for global crude grid (physical space).
XBF	X coordinate for body fine grid.
XI	ξ coordinate for global crude grid (transformed space).
XILE	ξ coordinate of local wing section leading edge.
XINB	Input X ordinates defining axisymmetric body.
XINW	Wing section defining X-ordinates.
XITE	ξ coordinate of local wing section trailing edge.
XLE	X coordinate of local wing section leading edge.
XLET	X coordinate of wing tip leading edge.
XMOM	Position about which configuration moments are computed.
XNC	Body normal vector X direction at crude grid body points.
XNF	Body normal vector X direction at fine grid body points.
XNOSE	X coordinate of body nose repositioned in crude grid.
XOL	Non-dimensional distance along body length and wing chord.
XPL	X coordinate of input wing section leading edge.
XPT	X coordinate of input wing section trailing edge.
XSF	X coordinate defining wing sections at each fine grid boundary points.
XTAIL	X coordinate of body tail repositioned in crude grid.
XTE	X coordinate of local wing section trailing edge.
XTET	X coordinate of wing tip trailing edge.
XWF	Fine embedded wing grid X coordinate.

<u>VARIABLE</u>	<u>DESCRIPTION</u>
Y	Y coordinate for global crude grid (physical space).
YBF	Y coordinate for body fine grid.
YINL	Wing section defining lower Y-ordinates.
YINU	Wing section defining upper Y-ordinates.
YNC	Body normal vector Y direction at crude grid body points.
YNF	Body normal vector Y direction at fine grid body points.
YOB	Wing span station ($2Y/b$).
YP	Y coordinate of input wing section trailing edge.
YSF	Y coordinate defining wing sections at each fine grid boundary points.
YTIP	Y coordinate of wing tip.
Z	Z coordinate for global crude grid (physical space).
ZBF	Z coordinates for body fine grid.
ZETA	ζ coordinate for global crude grid (transformed space).
ZNC	Body normal vector Z direction at crude grid body points.
ZNF	Body normal vector Z direction at fine grid body points.
ZWF	Fine embedded wing grid Z coordinate.
ZWING	Wing height relative to center of body.

|

RECOMMENDATIONS FOR USAGE

The thing that becomes apparent when first using a three-dimensional transonic relaxation scheme is that a considerable amount of computer time and core is required for a solution. Perhaps, an order of magnitude increase over typical resources for a subsonic/supersonic panel method will be noted. And, all of this effort will result in a solution for a single angle-of-attack, Mach number, and Reynolds number combination. It becomes very important to conserve time and resources when using this type of methodology. The geometry verification section of the method has been developed for this reason. It has been found advantageous to use this code in the following manner. When first setting up for analysis of a new configuration, plan on submitting a secondary job along with the primary job (which will provide the complete solution). The secondary job should be set (AXIT = 0, AXITF = 0) for the geometry verification mode or set the solution for a single crude and single fine grid iteration. This will provide a complete set up and cycle through the entire code. Since time requirements will be low, the secondary job should be returned quickly. If errors are found, the primary job can be cancelled to save costs and the error can be quickly corrected.

Analyses performed on highly swept/highly tapered wing planforms at extreme flow conditions indicate that occasionally an erroneous diverging condition at the wing tip is possible. This situation can be identified by increasing values of $\Delta\phi_{MAX}$ at the last span station on the wing. For severe cases, propagation of the discrepancy in-board will be noted. This problem is caused by the large differences in resolution between the embedded wing grid system and the surrounding crude grid system. It occurs only when strong shock waves exist at the wing tip. A code modification has been developed to relieve this problem so solutions at extreme conditions can be obtained. In the main program, a parameter "KTIP" has been set to 0. This will provide a normal solution process. If wing tip problems are encountered, "KTIP" should be set to 1 (KTIP = 1). This will have the effect of reducing wing fine grid density in general (80 evenly spaced points along the chord) and severely stepping down resolution at the wing tip. This will make the crude and fine grid systems more compatible from a numerical standpoint. This option should not be used for the

majority of cases for which it will not be required. Note that the included sample cases provide examples of geometries and flow conditions for which this option was not necessary.

In most cases, modeling wing-body combinations using the crude grid body only option (BKOD < 0) should be quite sufficient. As might be expected, computing resources are conserved. There is normally high grid density in the wing-body juncture region because of the crude grid stretching with its origin near the juncture. If details of the fuselage are important (canopies, blisters, and fairings), the fine body grid option is recommended (BKOD > 0). Isolated bodies, because of the reduced computing requirements, should always be analyzed using the embedded body grid system.

It is recommended that the wing crude grid system output option (WPO = 1) be used. While crude grid wing C_p distributions are of little value beyond diagnosing errors, the Mach charts will provide a measure of the extent of the supersonic flow region into the flow field.

The wing and wing-body sample cases were all computed by using 100 crude iteration cycles followed by 80 crude-fine iteration cycles. Comparisons made with experimental data for the sample cases and additional wing-body configurations indicated that this level of computational convergence would be satisfactory for engineering applications. Any discrepancies between the experiment and analysis were attributed to the methods small-disturbance character and the high flow gradients encountered in certain applications. Waggoner⁽⁴⁰⁾, however, was shown that the basic 100/80 iteration cycle count may be insufficient for high aspect ratio supercritical wing cases. This may, in part, explain correlation discrepancies noted for the NASA supercritical wing-fuselage configuration (page 82) and the Douglas wing cylinder configuration (page 92). For this class of geometry, the total number of iterations may have to be increased by a factor of 3 or 4. The user should be aware of this lack of convergence if applications to high aspect ratio wings or supercritical type sections are of interest.

REFERENCES

1. Murman, E. M. and Cole, J. D.: "Calculation of Plane Steady Transonic Flows," AIAA Journal, 9, 1971.
2. Steger, J. L. and Lomax, H.: "Transonic Flow About Two-Dimensional Airfoils By Relaxation Procedures," AIAA Journal, Vol 10, No. 1, January 1972.
3. Garabedian, P. R. and Korn, D. G.: "Analysis of Transonic Airfoils," Comm on Pure and Applied Math, Vol 24, 1971, pp 841-851.
4. Jameson, A.: "Iterative Solution of Transonic Flows Over Airfoils and Wings, Including Flows at Mach 1," Comm on Pure and Applied Math, Vol 27, 1974.
5. Bailey, F. R. and Steger, J. L.: "Relaxation Techniques for Three-Dimensional Transonic Flow About Wings," AIAA J., Vol 11, No. 3, March 1973, pp 318-325.
6. Klunker, E. B. and Newman, P. A.: "Computation of Transonic Flow About Lifting Wing Cylinder Combinations," Journal of Aircraft, Vol 2, No. 4, April 1974.
7. Hall, M. G. and Firmin, M. C. P.: "Recent Developments In Methods For Calculating Transonic Flows Over Wings," ICAS Paper No. 74-18, August 1974.
8. Van Der Vooren, J., Slooff, J. W., Huizing, G. H. and Van Essen, A.: "Remarks On The Suitability of Various Transonic Small Perturbation Equations To Describe Three-Dimensional Transonic Flow; Examples Of Computations Using A Fully Conservative Rotated Difference Scheme," Symposium Transonicum II, Gottingen, Germany, September 8, 1975.
9. Schmidt, W.: "Progress in Transonic Flow Computations - Analysis and Design Methods For Three-Dimensional Flows," Von Karman Inst For Fluid Mechanics, Lecture Series 87, March 1976.
10. Bailey, F. R. and Ballhaus, W. F.: "Comparisons of Computed and Experimental Pressures For Transonic Flows About Isolated Wings and Wing-Fuselage Configurations," NASA SP-347, pp 1213-1231, 1975.

11. Albone, C. M. , Hall, M. G. and Joyce, G.: "Numerical Solutions For Transonic Flows Past Wing-Body Combinations," Symposium Transonicum II, Gottingen, Germany, September 1975.
12. Ballhaus, W. F.: "Some Recent Progress In Transonic Flow Computations," VKI Lecture Series On Computational Fluid Dynamics, March 15, 1976, Belgium.
13. Jameson, A. and Caughey, D. A.: "Numerical Calculation of the Transonic Flow Past a Swept Wing," NASA CR-153297, 1977.
14. Jameson, A. and Caughey, D. A.: "Finite Volume Method For Transonic Potential Flow Calculations," AIAA Paper 77-635, June 1977.
15. Caughey, D. A. and Jameson, A.: "Numerical Calculation of Transonic Potential Flow About Wing-Cylinder Combinations," AIAA Paper 77-677, June 1977.
16. Boppe, C. W.: "Calculation of Transonic Wing Flows By Grid Embedding," AIAA Paper 77-207, January 1977.
17. Lomax, H. , Bailey, F. R. and Ballhaus, W. F.: "On The Numerical Simulation Of Three-Dimensional Transonic Flow With Application To the C-141 Wing," NASA TN D-6933, August 1973.
18. Liepmann, H. W. and Roshko, A.: "Elements of Gas Dynamics," John Wiley and Sons, Inc. , New York, 1967.
19. Krupp, J. A.: "The Numerical Calculation Of Plane Steady Transonic Flows Past Thin Lifting Airfoils," Boeing Scientific Research Laboratory Report, D180-12958-1, June 1971.
20. Carlson, L. E.: "Transonic Airfoil Flowfield Analysis Using Cartesian Coordinates," NASA CR-2577, August 1975.
21. Jameson, A.: "Transonic Flow Calculations," VKI Lecture Series On Computational Fluid Dynamics, March 1976, Belgium.
22. South, J. C.: "Comments On Difference Schemes For the Three-Dimensional Transonic Small-Disturbance Equation For Swept Wings," NASA TM X-71980, July 1976.
23. South, J. C. and Keller, J. D.: "Axisymmetric Transonic Flow Including Wind Tunnel Wall Effects," NASA SP-347, 1975, pp1233-1268.

24. Werner, J. : "Slender Body Boundary Condition Corrections for Body Shapes Modeled By an Approximate Computational Surface," Grumman Aerodynamics Report 390-77-04, June 1977.
25. Vachris, A. F. and Yaeger, L. S. : "Quick-Geometry - A Rapid Response Method For Mathematically Modeling Configuration Geometry," NASA SP-390, October 1975, pp 49-73.
26. Marconi, F. and Yaeger, L. : "Development of A Computer Code for Calculating the Steady Super/Hypersonic Inviscid Flow Around Real Configurations," NASA CR-2626 (Vol II), May 1976.
27. Nash, J. F. and Tseng, R. R. : "The Three-Dimensional Turbulent Boundary Layer On an Infinite Yawed Wing," The Aeronautical Quarterly, November 1971, pp 346-362.
28. Mason, W. H. , et al. : "An Automated Procedure For Computing the Three-Dimensional Transonic Flow Over Wing-Body Combinations, Including Viscous Effects," Air Force Flight Dynamics Laboratory Report AFFDL-TR-77-122, Vol I, October 1977.
29. Bradshaw, P. and Ferriss, D. H. : "Calculation of Boundary Layer Development Using the Turbulent Energy Equation. Compressible Flow on Adiabatic Walls," J. Fluid Mech, Vol 46, 1971.
30. Bavitz, P. C. : "An Analysis Method For Two-Dimensional Transonic Viscous Flow," NASA TN D-7718, January 1975.
31. Swihart, J. M. and Whitcomb, C. F. , "Pressure Distributions on Three Bodies of Revolution to Determine the Effect of Reynolds Number Up to and Including the Transonic Speed Range," NACA RM L53H04, October 1953.
32. Couch, L. M. and Brooks, C. W. Jr. : "Effect of Blockage Ratio on Drag and Pressure Distributions for Bodies of Revolution at Transonic Speeds," NASA TN D-7331, November 1973.
33. Shepherd, F. : "Report of Wind Tunnel Pressure Measurements and Flowfield Studies on the Gulfstream II and IIA Canopies," GFTT 058, January 1976.
34. Monnerie, B. and Charpin, F. : "Essais de Buffeting d'une Aile en Fleche Transsonique," Colloque d'Aerodynamique Applique Lille, November 1973.

35. Edwards, G. G. and Boltz, F. W.: "An Analysis of the Forces and Pressure Distribution on a Wing with the Leading Edge Swept Back 37.25° ," NACA RM A9K01, 1950.
36. Loving, D. L. and Estabrooks, B. B.: "Transonic Wing Investigation in the Langley 8-Foot High Speed Tunnel at High Subsonic Mach Numbers and At a Mach Number of 1.2," NACA RM L51F07, September 1951.
37. Montoya, L. C.: "Effect of Winglets on a First-Generation Jet Transport Wing," NASA TN D-8474, July 1977.
38. Mann, M. J. and Langhans, R. A.: "Transonic Aerodynamic Characteristics of a Supercritical-Wing Transport Model with Trailing-Edge Controls," NASA TM X-3431, October 1977.
39. Henne, P. A., and Hicks, R. M.: "Transonic Wing Design Using Advanced Computational Methods," AIAA Paper 78-105, January 1978.
40. Waggoner, E. G.: "Computational Transonic Analysis For a Supercritical Transport Wing-Body Configuration," AIAA Paper 80-129, January 1980.

1. Report No. NASA CR-3243	2. Government Accession No.	3. Recipient's Catalog No.	
4. Title and Subtitle TRANSONIC FLOW FIELD ANALYSIS FOR WING-FUSELAGE CONFIGURATIONS		5. Report Date May 1980	
		6. Performing Organization Code	
7. Author(s) Charles W. Boppe		8. Performing Organization Report No.	
		10. Work Unit No.	
9. Performing Organization Name and Address GRUMMAN AEROSPACE CORPORATION BETHPAGE, NEW YORK 11714		11. Contract or Grant No. NAS1-14732	
		13. Type of Report and Period Covered Contractor Report	
12. Sponsoring Agency Name and Address National Aeronautics and Space Administration Washington, DC 20546		14. Sponsoring Agency Code	
15. Supplementary Notes Langley Technical Monitor: Perry A. Newman Topical Report			
16. Abstract A computational method for simulating the aerodynamics of wing-fuselage configurations at transonic speeds has been developed. The finite difference scheme is characterized by a multiple embedded mesh system coupled with a modified or extended small-disturbance flow equation. This approach permits a high degree of computational resolution in addition to coordinate system flexibility for treating complex realistic aircraft shapes. To augment the analysis method and permit applications to a wide range of practical engineering design problems, an arbitrary fuselage geometry modeling system has been incorporated as well as methodology for computing wing viscous effects. Configuration drag is broken down into its friction, wave, and lift-induced components. Typical computed results for isolated bodies, isolated wings, and wing-body combinations are presented. The results are correlated with experimental data. A computer code which employs this methodology is described in the Appendix of this report.			
17. Key Words (Suggested by Author(s)) Transonic Flow Computational Aerodynamics Flow Simulations Wing-Fuselage Finite Difference Relaxation Scheme		18. Distribution Statement Unclassified-Unlimited Subject Category 02	
19. Security Classif. (of this report) Unclassified	20. Security Classif. (of this page) Unclassified	21. No. of Pages 158	22. Price* \$8.00